# Transportable ultra-stable laser system with an instability down to $10^{-16}$

Von der QUEST-Leibniz-Forschungsschule
der Gottfried Wilhelm Leibniz Universität Hannover
zur Erlangung des Grades

Doktorin der Naturwissenschaften
Dr. rer. nat.

genehmigte Dissertation von

M.Sc. Sofia Herbers

2021

| | |
|---|---|
| Referent | PD Dr. Christian Lisdat |
| Korreferent | Prof. Dr. Piet O. Schmidt |
| Korreferent | Dr. Rodolphe Le Targat |
| Tag der Promotion | 14.12.2021 |

## Abstract

In this work, a transportable ultra-stable laser system based on a Fabry-Pérot cavity with crystalline aluminium gallium arsenide ($Al_{0.92}Ga_{0.08}As$) / gallium arsenide (GaAs) mirror coatings, fused silica glass mirror substrates and a 20 cm-long ultra low expansion glass spacer was designed and built to serve as a clock laser for a $^{87}$Strontium (Sr) lattice clock. The laser system uses an external-cavity diode laser, which is stabilized to a resonance frequency of the Fabry-Pérot cavity using the Pound-Drever-Hall method. This reduces the laser's fractional frequency instability down to the cavity's fractional length instability. Due to the high absorbance of $Al_{0.92}Ga_{0.08}As$/GaAs mirror coatings for visible light, the laser is operated at a wavelength of 1397 nm, which is twice the transition wavelength of a $^{87}$Sr lattice clock. The laser system therefore includes frequency doubling and light distribution for operation of a $^{87}$Sr lattice clock.

The fundamental limit of the cavity's fractional length instability and thus the laser's fractional frequency instability is determined by the thermal noise floor resulting from Brownian, thermoelastic and thermorefractive noise of the cavity components. The calculated thermal noise floor limit given as modified Allan deviation of the fractional frequency instability $\mathrm{mod}\,\sigma_\mathrm{y}$ is below $1 \cdot 10^{-16}$. Besides the thermal noise, technical noise caused by seismic noise, residual amplitude modulation, laser power, pressure, optical path length and temperature fluctuations affects the laser's fractional frequency instability. The single contributions of the technical noise were investigated and their impact on the laser's fractional frequency instability were suppressed below the thermal noise floor for averaging times around one second using passive or active stabilization.

The laser system achieves an instability as low as $\mathrm{mod}\,\sigma_\mathrm{y} = 1.6 \cdot 10^{-16}$, which is already a factor 1.3 lower than the theoretically possible instability of $\mathrm{mod}\,\sigma_\mathrm{y} = 2 \cdot 10^{-16}$ for the same resonator with tantalum pentoxide ($Ta_2O_5$) / fused silica ($SiO_2$) mirrors. This is the lowest fractional frequency instability among published transportable laser systems. Depending on the averaging time of interest, the fractional frequency instability has been reduced by a factor of up to seven compared to Physikalisch-Technische Bundesanstalt (PTB)'s current transportable laser system, which had the lowest fractional frequency instability until now. This reduced instability allows a reduction of the Dick effect limit by roughly a factor of four for interrogation times below 0.5 s, which would reduce the clock's instability limit significantly.

Keywords:

- ultra-stable optical cavitiy, ultra-stable optical resonator
- transportable clock laser system, transportable interrogation laser system
- crystalline $Al_{0.92}Ga_{0.08}As$/GaAs mirror coatings

# Contents

# Abbreviations

| | |
|---|---|
| ADEV | Allan deviation |
| ADP | ammonium dihydrogen phosphate |
| Al | Aluminium |
| $Al_{0.92}Ga_{0.08}As$ | aluminium gallium arsenide |
| AlAs | aluminium arsenide |
| AOM | acousto-optic modulator |
| cAOM | control acousto-optic modulator |
| CTE | cofficient of thermal expansion |
| DC | direct current |
| DFB | distributed feedback |
| ECDL | external-cavity diode laser |
| EOM | electro-optic modulator |
| FEM | finite element method |
| FFT | fast Fourier transform |
| FPGA | field-programmable gate array |
| FS | fused silica |
| FSR | free spectral range |
| GaAs | gallium arsenide |
| HC | Hänsch-Couillaud |
| $LiNbO_3$ | lithium niobate |
| LO | local oscillator |
| mADEV | modified Allan deviation |
| mAOM | marker acousto-optic modulator |
| NTC | negative temperature coefficient |
| PBS | polarizing beam splitter |
| PD | photodiode |
| PDH | Pound-Drever-Hall |
| PI | proportional-integral |
| PID | proportional-integral-derivative |
| PLL | phase-locked loop |
| PPLN | periodically-poled lithium niobate |
| PSD | power spectral density |
| PT | photothermal |
| PTB | Physikalisch-Technische Bundesanstalt |
| PTE | photothermoelastic |

| | |
|---|---|
| PTR | photothermorefractive |
| QPN | quantum projection noise |
| QWL | quarter-wavelength |
| RAM | residual amplitude modulation |
| RF | radio frequency |
| rms | root mean square |
| ROC | radius of curvature |
| SHG | second-harmonic generation |
| SI | international system of units |
| $SiO_2$ | fused silica |
| Sr | Strontium |
| $Ta_2O_5$ | tantalum pentoxide |
| TE | thermoelastic |
| TEC | thermoelectric cooler |
| TEM | transverse electromagnetic |
| TO | thermo-optic |
| TR | thermorefractive |
| ULE | ultra low expansion |
| XPS | extruded polystyrene foam |

# 1. Introduction

Of all quantities in the international system of units (SI), the realization of the second has the smallest uncertainty in relative value. Currently, caesium atomic clocks realize our second. However, optical clocks[1] are deemed strong candidates for the redefinition of the second as they outperform the caesium clocks[1] as shown first by Campbell et al. [1], Chou et al. [2], Falke et al. [3] and Le Targat et al. [4].

Because optical clocks are such accurate measurement tools of time, they have other applications beyond time keeping, such as tests of fundamental physics like setting constrain to the time variation of fundamental constants, search for dark matter, and detection of violations of Lorentz invariance [for latest publications see amongst others 5–10]. Accordingly, Godun et al. [5], Huntemann et al. [8], McGrew et al. [9] and Schwarz et al. [11] were able to show an upper boundary of about $1 \times 10^{-16}\,\mathrm{yr}^{-1}$ for the time variation of the proton-to-electron mass ratio and an upper boundary of low $10^{-17}\,\mathrm{yr}^{-1}$ for the time variation of the fine structure constant. Furthermore, Roberts et al. [7] presented an optical clock network in Europe, which is used to search for dark matter, to mention just a few. Clocks with high accuracy can also be used for geodetic measurements [12–15], which is the application considered in this work.

From general relativity, it is known that the frequency of a clock is affected by the gravitational potential. Hence, a gravitational potential difference $\Delta V$ of about $0.1\,\mathrm{m}^2\,\mathrm{s}^{-2}$, which corresponds to approximately 1 cm in height difference on Earth's surface, results in a fractional relativistic redshift $\Delta\nu_{rel}/\nu_0$ of $10^{-18}$ between two clocks [15].

Today's knowledge of geodetic heights with respect to the geoid, as an equipotential surface, on Earth is based on terrestrial and satellite-based measurements. For Europe, discrepancies of 1 cm to 5 cm for areas with good data quality and coverage where found, but for certain areas like high mountain regions or islands in the high seas the differences often exceed 10 cm [16], which can be seen as benchmark for optical clocks. Today's laboratory clocks already meet the requirements to resolve approximately 1 cm of height [e.g. 17–19]. Over short distance, conventional methods like geometric leveling offer low uncertainties on the sub-millimeter level, but it is time-consuming and accumulates large errors over long distances. In contrast, the measurement uncertainty using clocks connected by optical links is almost independent of the distance between two measurement points. A demonstration of such a laboratory clock network is given in Lisdat et al. [20]. As laboratory systems are limited to one certain location, stand-alone transportable clocks that can be transported to the point of interest

[1] Strictly speaking, most systems described in literature as optical or atomic clocks are not a clock, but a frequency standard, since there is no clockwork. This differentiation is also handled generously in this work.

are needed for geodetic measurements. Proof-of-concept geodetic measurements with transportable clocks have been demonstrated by Grotti et al. [21], Takamoto et al. [22], Takano et al. [23] and Huang et al. [24] over distances up to 1200 km so far with inaccuracies down to approximately 5 cm. Besides geodetic applications, a compact and robust, stand-alone optical clock can serve as a transportable frequency standard and replace the hydrogen maser at better performance. Also, space experiments on fundamental physics are conceivable with transportable optical clocks [25, 26].

An optical clock has two main parameters that are important for all its applications: its instability and its systematic uncertainty. The transition frequency of a clock is shifted by various parameters such as temperature, electric and magnetic fields. Thus, the measured transition frequency of a clock needs to be corrected to obtain the undisturbed transition frequency of the clock. The required corrections are not perfectly known, leading to the clock's systematic uncertainty. To reach low systematic uncertainties, a well controlled and characterized system is needed. Current stationary optical clocks reach fractional uncertainties of low $10^{-18}$ and transportable ones fractional uncertainties down to mid $10^{-18}$. For full uncertainty budgets of these clocks see among others Bothwell et al. [17], Cao et al. [27], Koller et al. [28], McGrew et al. [18], Nicholson et al. [19] and Takamoto et al. [22].

The instability of an optical clock describes the statistical scattering of the clock frequency and therefore a low instability corresponds to a high measurement precision. Hence, lower instabilities result in shorter averaging times until a certain statistical uncertainty is reached, which is the key to fast time-resolved measurements such as measurements of tides.

The clock instabilities of today's best optical clocks are usually limited by the Dick effect or the quantum projection noise (QPN). The Dick effect describes a limitation of the clock instability due to an aliasing effect caused by alternating periods of atom interrogation, during which the atoms are probed by the clock laser, and dead time, during which the atoms are read out and prepared [29, 30]. The QPN results from the projective measurement of the atom's[2] quantum state, which causes the atom to collapse into the ground or excited state [31]. Both are described in more detail in chapter 2.

To reduce the clock instability, one or both limits have to be reduced. As the QPN limit confines the instability of an optical clock for uncorrelated states, it can be overcome by generating correlated states, for example spin squeezed states [32, 33] as demonstrated among others by Braverman et al. [34] and Kruse et al. [35]. The instability of such clocks is ultimately restricted by the Heisenberg limit, which results from the Heisenberg uncertainty.

However, Schulte et al. [36] point out that for optical clocks spin squeezing does only offer a relevant advantage in clock instability for optical clocks with small atom number, where QPN is by far the largest contribution. In contrast, the QPN limit of clocks with large atom number, like lattice clocks, is usually below the Dick effect limit, and therefore spin squeezing does not decrease the clock instability substantially

[2] Atom is used as an umbrella term for both neutral atom and ion.

for these clocks.

Dead-time-free or synchronous interrogation of at least two atom ensembles such as described in Schioppo et al. [37] and Hume and Leibrandt [38][3] allows clocks to overcome the Dick effect limit and reduces the QPN noise by extending the interrogation time beyond the laser's coherence time. However, these methods require two Dick-effect-limited clocks of comparable stability in relative proximity to offer any relevant advantage. Finally, the contributions from both QPN and the Dick effect to the instability limit of a clock depend, either directly or indirectly, on the frequency instability of the clock laser[4] $\sigma_{\mathrm{y,L}}$[5] that is used to interrogate the atoms. Therefore, the past continuous improvement of clock instability was only possible due to the continuous improvement of laser instability, and still clocks generally benefit from lower laser instability. While improvements to the atomic package to perform dead-time-free interrogation and spin squeezing require extensive changes to the atomics package of a clock and substantially increase its complexity, an improved clock laser can be developed independently and integrated into the clock as a plug-in component. It is thus an excellent means of improving the performance of an already operating transportable optical clock.

Currently, the best clock laser systems are based on lasers that are pre-stabilized to ultra-stable external optical reference cavities using the Pound-Drever-Hall locking technique [41] to transfer the length stability $\delta l/l_0$ of the cavity to the frequency stability $\delta\nu/\nu_0$ of the clock laser light, described in more detail in section 3.1. The fundamental limit of the cavity length instability is the thermal noise, also known as thermo-dynamic noise, in the cavity components, which depends on the cavity temperature, the cavity geometry and material properties of the cavity components, described in more detail in section 3.2. As the thermal noise limit of a cavity decreases with increasing separation $l_0$ of the cavity mirrors and with lower cavity temperature, longer cavities [e.g. 42, 43] or cavities operated at low temperature [e.g. 44, 45] have been build to reduce the laser instability in the past years. However, for transportable systems this is only useful to a limited extent as long cavities are in conflict with a compact and light-weight design, which is beneficial for a transportable system. Cryogenic cooling in a transportable system requires a low-vibration closed-cycle system to not degrade the laser's frequency stability by seismic noise affecting the length stability of the ultra-stable cavity. Low-vibration cryocoolers, such as pulse tube cooler or coolers using evaporation of a liquid, might be a suitable choice for a transportable system. However, cooling to cryogenic temperature adds additional weight, increases the power consumption of a clock and requires permanent cooling also during transport to ensure a prompt availability of the laser system after transport. Thus, cryogenic cooling is a disproportionate effort for robust and self-contained transportable system compared to the use of crystalline gallium arsenide (GaAs)/aluminium gal-

[3] In this paper, a single-ion clock and a lattice clock are used to demonstrate synchronous interrogation rather than two clocks with atom ensembles.

[4] The clock laser is also referred to in the literature as interrogation laser.

[5] Frequency instability is commonly described using the Allan deviation $\sigma_{\mathrm{y}}(\tau)$, which was first introduced by Allan [39, 40]. Here, $\tau$ is the averaging time.

lium arsenide ($Al_{0.92}Ga_{0.08}As$) mirror coatings [46] to reduce the thermal noise floor. Crystalline $GaAs/Al_{0.92}Ga_{0.08}As$ mirror coatings provide a third option addressing the material properties, which can be used at same cavity geometry and temperature in contrast to longer or cryogenic cooled cavities. It relies on the higher quality factor of these coatings compared to the traditional tantalum pentoxide ($Ta_2O_5$)/fused silica ($SiO_2$) coatings. However, these crystalline mirror coatings are highly absorbing for visible light. The laser system must be operated at a sub-harmonic wavelength and up-converted to the clock transition, for example, by frequency-doubling.

Besides the thermal noise, several influences like fluctuation of temperature, pressure and laser power or seismic noise degrade the cavity length stability as described in section 5.5 to 5.9. Their impact on the cavity instability has to be reduced, for example, by active or passive stabilization below the thermal noise limit to allow an operation of the cavity at its fundamental limit. Here, the vibration sensitivity of the cavity length, which is a parameter for the mechanical deformation of the cavity caused by seismic noise, typically increases with spacer length $l_0$ in contrast to the thermal noise limit. Taking the contributions of seismic noise and thermal noise into account, we find a practical optimal in cavity length, at which the cavity instability is minimal. To increase the optimal spacer length, the vibration sensitivity is reduced by decoupling the cavity from seismic noise using particular mounting concepts of the reference cavity. In this respect, a rugged, transportable mounting design is more challenging than laboratory systems, which benefit from loose and soft mounting not applicable to transportable systems. Different mounting designs for transportable reference cavities allowing a rugged mounting and providing low vibration sensitivity were established in the past years. Examples for such mountings are small spherical [47, 48], cubical [49, 50], cylindrical [51–55] and double tetrahedral [56] cavities. The different designs come along with different advantages and disadvantages such as scalability of cavity length $l_0$ and complexity of the mounting structure as further discussed in section 5.7.

Today's best laser systems are based on cryogenic silicon cavities with an instability down to $\mathrm{mod}\,\sigma_{y,L}$[6] $= 4 \cdot 10^{-17}$ [44, 45] or a 48 cm long glass cavity with an instability of $\sigma_{y,L} = 8 \cdot 10^{-17}$ [43]. Clock instabilities of below $1 \cdot 10^{-16}/\sqrt{\tau}$ [11, 37, 57] have been realized in a laboratory environment. Transportable stand-alone clocks show instabilities of down to $\sigma_y = 1 \cdot 10^{-15}/\sqrt{\tau}$ [28, 27], with clock laser instabilities of down to $\mathrm{mod}\,\sigma_{y,L} = 3 \cdot 10^{-16}$ [51].

In this work, a new clock laser system to reduce the instability of PTB's transportable Sr lattice clock [28] to below $\sigma_y = 1 \cdot 10^{-15}/\sqrt{\tau}$ is presented. It is based on crystalline mirror coatings [46] and operated at the sub-harmonic wavelength of the clock transition near 1397 nm. The mirror substrates are made out of fused silica glass and the 20-cm-long spacer is made out of ultra low expansion glass. The choice of the mirror substrates and spacer is discussed in section 3.3. The measured instability curve of the laser system as well as the remaining contributions to the laser instability caused by seismic noise, and variations of residual amplitude modulation,

[6] $\mathrm{mod}\,\sigma_y$ indicates that the modified Allan deviation [39, 40] of a fractional frequency fluctuation is used.

temperature, laser power, and pressure are discussed in chapter 5. Frequency-doubling to the transition frequency of $^{87}$Sr and its influence on the effective laser instability are discussed in chapter 6.

# 2. Clock instability

Several contributions affect the instability of a clock, including electronic noise, photon shot noise, detection laser noise, quantum projection noise (QPN) and the Dick effect. A detailed discussion for a Sr lattice clock is found in Al-Masoudi et al. [58]. As mentioned in the introduction, today's best clocks' instabilities are in general determined by the QPN limit or the Dick effect. The equations below give the correlation between clock instabilities for QPN-limited or Dick-effect-limited clocks and the laser instability. Here, we consider Rabi's and Ramsey's methods, which are most common. Rabi interrogation consists of a single $\pi$-pulse of duration $t_\mathrm{i} = t_\pi$, whereas Ramsey interrogation consists of two $\pi/2$-pules of duration $t_{\pi/2}$ separated by a variable dark time $t_\mathrm{dark}$, leading to $t_\mathrm{i} = 2\, t_{\pi/2} + t_\mathrm{dark}$.

## 2.1. Coherence time

The coherence time $t_\mathrm{coh}$, which governs the maximum possible interrogation time $t_\mathrm{i}$, depends on the laser instability $\sigma_\mathrm{y,L}$ and the interrogation scheme. Following Schulte et al. [36], Matei et al. [44] and Leroux et al. [59], the coherence time is defined as the time at which the root mean square (rms) phase deviations is below 1 rad, which corresponds to the case that after the coherence time $t_\mathrm{coh}$ in more than 99 % of all cases the rms phase excursion is below $\pm\pi$. Equation 2.1 gives a simple approach to determine the approximate coherence time $t_\mathrm{coh}$ from the Allan deviation (ADEV) of a laser's fractional frequency instability $\sigma_\mathrm{y,L}$.

$$\frac{1\,\mathrm{rad}}{2\pi\,\nu_0\,t_\mathrm{coh}} \stackrel{!}{=} \sigma_\mathrm{y,L}(t_\mathrm{coh}) \tag{2.1}$$

Here, $\nu_0$ is the absolute clock frequency. For Rabi and Ramsey interrogation, the observed excitation after an interrogation yields the average frequency during the interrogation. Thus, the coherence time $t_\mathrm{coh}$ is a good estimation for a maximum reasonable interrogation time $t_\mathrm{i}$. However, in practice the optimal interrogation time to achieve best clock performance depends on several parameters like clock type, interrogation scheme and frequency spectrum of the laser noise. An example how the optimal interrogation time can be found is given in Leroux et al. [59] for Ramsey interrogation.

The coherence time and thus maximum interrogation time increase with reducing laser instability. As one may expect, this usually results in better frequency instability of the clock as discussed in sections 2.2 and 2.3 below.

## 2.2. Quantum projection noise

The QPN limit $\sigma_{\mathrm{y,QPN}}$ of the clock instability, which results form the measurement of the atomic state, is given by equation 2.2 and is discussed in detail amongst others in Hobson [60].

$$\sigma_{\mathrm{y,QPN}} = \frac{1}{D\,\nu_0}\sqrt{\frac{Q_\mathrm{e}(1-Q_\mathrm{e})}{N_\mathrm{at}}}\sqrt{\frac{t_\mathrm{cy}}{\tau}} \tag{2.2}$$

Here, $Q_\mathrm{e}$ is the excitation probability (usually $Q_\mathrm{e} \approx 0.5$), $N_\mathrm{at}$ the number of atoms interrogated, $\tau$ the averaging time, $D$ the error-signal discriminant and $t_\mathrm{cy}$ the single cycle duration, $t_\mathrm{cy} = t_\mathrm{i} + t_\mathrm{dead}$, with the dead time $t_\mathrm{dead}$, while the atoms are prepared and are read out. Obviously, the QPN limit $\sigma_{\mathrm{y,QPN}}$ decreases with $\sqrt{N_\mathrm{at}}$, and therefore clocks with high atom number $N_\mathrm{at}$ are beneficial compared to single atom clocks. Dick [29] and Dick et al. [61] give the formulas for the error-signal discriminant $D$ for Rabi and Ramsey interrogation:

$$D = \pi\, 0.60386\, t_\pi = \pi\, 0.60386\, t_\mathrm{i} \qquad \text{Rabi interrogation} \tag{2.3}$$

$$D = \pi\left[t_\mathrm{dark} + \left[2 - \frac{4}{\pi}\right] t_{\pi/2}\right] \qquad \text{Ramsey interrogation} \tag{2.4}$$

$$\approx \pi\, t_\mathrm{i} \qquad \text{for } t_\mathrm{dark} \gg t_{\pi/2} \tag{2.5}$$

Ramsey interrogation results in a lower QPN limit compared to Rabi interrogation at same interrogation durations $t_\mathrm{i}$ due to its steeper error-signal discriminant. Furthermore, the QPN limit reduces with higher interrogation time $t_\mathrm{i}$. Clocks using clock lasers with high instability and therefore short coherence times often operate near the limit $t_\mathrm{i} \ll t_\mathrm{cy}$. Here, the QPN limit reduces with $t_\mathrm{i}^{-1}$. For clock lasers with low instability and therefore long coherence time leading to $t_\mathrm{cy} \approx t_\mathrm{i}$, the QPN limit reduces with $t_\mathrm{i}^{-1/2}$. In both cases, lower clock laser instability will reduce the QPN limit.

## 2.3. Dick effect

The Dick effect as introduced by Dick [29] describes an aliasing caused by the dead time during the operation of the clock. It gives rise to a contribution $\sigma_{\mathrm{y,Dick}}$ to the clock's instability $\sigma_\mathrm{y}$, which depends directly on the power spectral density (PSD) of the clock laser's one-sided fractional frequency fluctuations $S_{\mathrm{y,L}}$[1]. Lower $S_{\mathrm{y,L}}$ results in lower clock laser instability $\sigma_{\mathrm{y,L}}$. Following Dick [29], Dick et al. [61], Santarelli et al. [63], Audoin et al. [64] and Greenhall [65], the Dick effect contribution to the

[1] $S_\mathrm{y}$ indicates that the one-sided fractional frequency fluctuation PSD is used, which is a frequency domain statistical dispersion and can be transferred to time domain statistical dispersion like the Allan deviation, see among others Benkler et al. [62]

clock instability is given by:

$$\sigma^2_{\mathrm{y,Dick}} = \frac{1}{b_0^2\,\tau}\sum_{k=1}^{\infty}|b_\mathrm{k}|^2\,S_{\mathrm{y,L}}(k/t_\mathrm{cy}) \tag{2.6}$$

$$b_0 = \frac{1}{t_\mathrm{cy}}\int_0^{t_\mathrm{cy}} b(t)\,\mathrm{d}t \tag{2.7}$$

$$b_\mathrm{k} = \frac{1}{t_\mathrm{cy}}\int_0^{t_\mathrm{cy}} b(t)\exp\!\left(-\frac{2\pi i k t}{t_\mathrm{cy}}\right)\mathrm{d}t \tag{2.8}$$

Here, $b_0$ and $b_\mathrm{k}$ are the Fourier coefficients for amplitude conversion near the $k$th harmonic of the single cycle frequency $f_\mathrm{cy} = 1/t_\mathrm{cy}$ of the frequency sensitivity function $b(t)$. It describes the response of the excitation probability to small frequency fluctuations. At the operating points ($Q_\mathrm{e} = 0.5$) of a clock using Rabi or Ramsey interrogation, respectively, it is given by equation 2.9 and 2.14.

Rabi:

$$\begin{aligned} b(t) &= \sin^2(\theta)\cos(\theta) \\ &\cdot\left[\sin(\Omega_1(t))\left\{1-\cos(\Omega_2(t))+\sin(\Omega_2(t))\right\}\left\{1-\cos(\Omega_1(t))\right\}\right] \quad 0<t<t_\mathrm{i} \\ &= 0 \qquad\qquad t_\mathrm{i}<t<t_\mathrm{cy} \end{aligned} \tag{2.9}$$

with

$$\theta = \frac{\pi}{2} + \arctan(0.798685) \tag{2.10}$$

$$\Omega_1(t) = \Omega\frac{t}{t_\mathrm{i}} \tag{2.11}$$

$$\Omega_2(t) = \Omega\left[1-\frac{t}{t_\mathrm{i}}\right] \tag{2.12}$$

$$\Omega = \pi\sqrt{1+0.798685^2} \tag{2.13}$$

Ramsey:

$$\begin{aligned} b(t) &= \sin\!\left(\frac{\pi\,t}{2\,t_{\pi/2}}\right) && 0<t<t_{\pi/2} \\ &= 1 && t_{\pi/2}<t<t_\mathrm{i}-t_{\pi/2} \\ &= \sin\!\left(\pi\frac{t_\mathrm{i}-t}{2\,t_{\pi/2}}\right) && t_\mathrm{i}-t_{\pi/2}<t<t_\mathrm{i} \\ &= 0 && t_\mathrm{i}<t<t_\mathrm{cy} \end{aligned} \tag{2.14}$$

For the simple case of Ramsey interrogation with negligibly short $\pi/2$-pules, equation 2.6 can be solved analytically [see appendix of 29]:

$$\sigma_{\mathrm{y,Dick}}^2 = \frac{1}{\tau}\frac{t_{\mathrm{cy}}^2}{t_{\mathrm{i}}^2}\sum_{k=1}^{\infty}\frac{1}{\pi^2 k^3}\,\sin^2\!\left(\frac{\pi k t_{\mathrm{i}}}{t_{\mathrm{cy}}}\right) S_{\mathrm{y,L}}(k/t_{\mathrm{cy}}) \tag{2.15}$$

According to equation 2.15, the Dick contribution $\sigma_{\mathrm{y,Dick}}$ reduces with decreasing laser noise $S_{\mathrm{y,L}}$ and higher duty factor $t_{\mathrm{i}}/t_{\mathrm{cy}}$ and therefore, higher interrogation time $t_{\mathrm{i}}$ at the same dead time $t_{\mathrm{dead}}$. The former is true in general (see equation 2.6), whereas the latter holds in most but not all cases. Generally, as long as $t_{\mathrm{i}}$ is significantly smaller than $t_{\mathrm{cy}}$, the Dick effect limit decreases with longer interrogation times $t_{\mathrm{i}}$. In the case of $t_{\mathrm{dead}} \ll t_{\mathrm{i}}$, $t_{\mathrm{i}} \approx t_{\mathrm{cy}}$, the Dick contribution eventually starts to become larger with increasing interrogation time in case of Rabi interrogation due to flicker frequency noise of ultra-stable lasers, which decreases with $1/f$ for $S_{\mathrm{y,L}}$. Longer interrogation times $t_{\mathrm{i}}$ and thus longer cycle times $t_{\mathrm{cy}}$, result in larger contribution from the laser's instability $S_{\mathrm{y,L}}$ due to its $1/f$ behavior, while $|b_{\mathrm{k}}|^2$ approaches a constant value. This results effectively in an increase of the Dick effect limit $\sigma_{\mathrm{y,Dick}}$ for very long interrogation times when using Rabi interrogation. In contrast, when using Ramsey interrogation, $|b_{\mathrm{k}}|^2$ trends quadratically towards zero, while $S_{\mathrm{y,L}}$ only increases approximately linearly for very long $t_{\mathrm{i}}$ at $t_{\mathrm{dead}} \ll t_{\mathrm{i}}$ and $t_{\pi/2} \ll t_{\mathrm{dark}}$, resulting in a continuous decrease of $\sigma_{\mathrm{y,Dick}}$. This operation mode piratically results in a continuous interrogation with constant sensitivity. Thus, the Dick effects limit must reduce to zero due the absence of any aliasing effect. If $t_{\pi/2}$ is not much smaller than $t_{\mathrm{dark}}$, $\sigma_{\mathrm{y,Dick}}$ trends not to zero also for Ramsey interrogation as the sensitivity function $b(t)$ is not constant equivalent to the case of Rabi interrogation. However, this occurs at time scales that are of little practical relevance for transportable clocks, at least so far. Hence, the impact of the Dick effect on clock instability is reduced by stabler clock lasers, both directly and by allowing longer interrogation times due to the laser coherence time limit.

# 3. Laser instability

In order to reduce a laser's frequency instability, the laser frequency can be stabilized to an ultra-stable external reference cavity, transferring the cavity's length stability $\delta l/l_0$ to the laser frequency stability with $\delta\nu/\nu_0 = -\delta l/l_0$ as described in section 3.1. Consequently, the laser frequency stability is now limited by the cavity length noise, which in the best case approaches the thermal noise of the cavity components as shown in section 3.2. The cavity noise, resulting from thermal noise, is affected by various parameters including material properties such as the Young's modulus or the quality factor. In section 3.3, the choice of cavity materials is discussed to minimize the thermal noise when designing a transportable reference cavity.

## 3.1. Pound-Drever-Hall locking technique

An external reference Fabry-Pérot cavity can be used to measure the laser frequency and feed back an error signal to the laser to suppress frequency fluctuations [66]. To generate an error signal for the stabilization, either the transmitted light can be used for a side-of-fringe [67] or a fringe-center technique [68] or the reflected light can be used for the Hänsch-Couillaud (HC) [69] or the Pound-Drever-Hall (PDH) [66] technique. In general, techniques using transmitted light are limited in bandwidth by the linewidth[1] $lw$ of the cavity and suffer from a lower signal-to-noise ratio [70]. As fast techniques and high signal-to-noise ratios are beneficial to transfer the stability of the cavity to the laser frequency, HC and PDH technique are preferable. The HC technique uses an external reference cavity with an internal linear polariser, birefringent crystal or Brewster plate and derives the error signal from the polarization of the back reflected light [69]. In the case of the PDH technique, which is the optical equivalent of the RF microwave Pound stabilizer [71], the phase of the laser light is modulated to generate an error signal from the reflected light [66], making it comparable complex. However, in contrast to the HC technique, the PDH technique can be made insensitive to technical noise of the laser by using high modulation frequencies [72], making it the most suitable choice for an ultra-stable laser.

[1] The ratio of the free spectral range (FSR) $FSR$ and the finesse $\mathcal{F}$ is defined as the linewidth $lw$ of a Fabry-Pérot cavity, $lw = FSR/\mathcal{F}$. For cavity in vacuum, the finesse is defined by the intensity reflection coefficient $R$ of the mirrors with $\mathcal{F} = \pi\sqrt{R}/[1-R]$ and the FSR is reciprocal to the cavity length $l_0$ with $FSR = c/[2l_0]$.

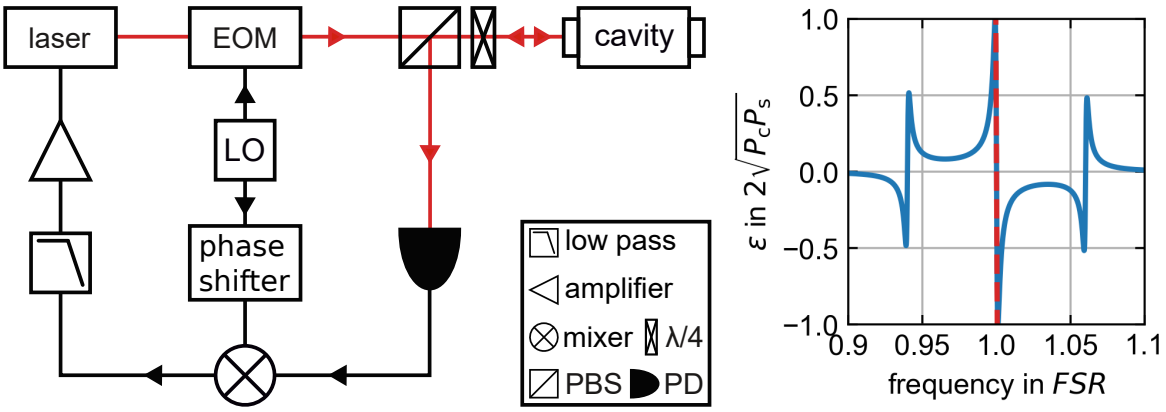


Figure 3.1.: Schematic sketch of the PDH locking technique (left). A detailed description is given in the text. The resulting error signal $\varepsilon_{\mathrm{PDH}}$ (blue solid) and its approximation by equation 3.1 (red dashed) normalized to $2\sqrt{P_{\mathrm{c}}P_{\mathrm{s}}}$ with $\mathcal{F} \approx 1000$, $f_{\mathrm{m}} \approx 60 \cdot lw$ (right).

### 3.1.1. Basic principle

Figure 3.1 left shows the schematic setup of the PDH technique. For a detailed description, see among others the introductory paper by Black [41]. The laser light passes through an electro-optic modulator (EOM) with a modulation frequency $f_{\mathrm{m}}$ larger than the cavity linewidth $lw$ to ensure that the side bands are reflected when the carrier, meaning the laser light, is in resonance. A local oscillator (LO) generates the modulation frequency $f_{\mathrm{m}}$. The back reflected light from the cavity, which passed the quarter waveplate twice, is picked up by the polarizing beam splitter (PBS) and sent to a photodiode (PD). The PD detects the optical power of the incident light, which is proportional to the square of the incident field strength, resulting in the detection of mixing products of carrier and sideband signals. This signal contains the phase information of the laser frequency with respect to the cavity's resonance frequency, which needs to be mixed down to direct current (DC) to generate a control signal. Therefore the PD signal is mixed with a reference signal of the frequency $f_{\mathrm{m}}$ as well generated by a LO. A phase shifter is needed to match the phase $\phi_{\mathrm{mod}}$ between reference signal and PD signal. The mixing product at twice the modulation frequency $f_{\mathrm{m}}$ is filtered out by a low-pass filter. The error signal, which is at roughly DC, goes through a servo amplifier and is forwarded to the laser tuning port to adjust the laser frequency.

Figure 3.1 shows the error signal[2] $\varepsilon_{\mathrm{PDH}}$ (blue curve) for a small modulation depth $M$, a fast modulation frequency $f_{\mathrm{m}} \gg lw$ and a phase[3] $\phi_{\mathrm{mod}} = \pi/2$ at the mixer, the so called dispersion signal[4]. The error signal is normalized to $2\sqrt{P_{\mathrm{c}}P_{\mathrm{s}}}$ with $P_{\mathrm{c}}$ and $P_{\mathrm{s}}$

[2]The equation is given in Appendix A.1

[3]How the phase $\phi_{\mathrm{mod}}$ effects the error signal $\varepsilon_{\mathrm{PDH}}$ is for example nicely shown in Riehle [73, section 9.2.2] and Shen et al. [74].

[4]The out-of-phase error signal with $\phi_{\mathrm{mod}} = \pi/2$ is often called the dispersion signal, while the in-phase error signal with $\phi_{\mathrm{mod}} = 0$ is called absorption signal, which originates from the relations in spectroscopy, for example phase-modulation saturation spectroscopy see Bjorklund [75] and Hall

being the power in the carrier and first-order side bands of the incident beam to the cavity, respectively.

Close to resonance, meaning for frequency deviations from the cavity resonance much smaller than the linewidth of the cavity, $\delta\nu \ll lw$, the error signal $\varepsilon_{\mathrm{PDH}}$ is proportional to the frequency deviation $\delta\nu$ [41], see equation 3.1 and figure 3.1 right red dashed line.

$$\varepsilon_{\mathrm{PDH}} = -\frac{8\sqrt{P_{\mathrm{c}}\,P_{\mathrm{s}}}}{lw}\delta\nu \tag{3.1}$$

As it is not possible to distinguish between frequency noise of the laser and cavity noise by looking at the error signal, the cavity noise affects the stability reachable with the PDH technique. While equation 3.1 only holds for a perfectly stable cavity, equation 3.2 [41] takes the cavity noise into account.

$$\varepsilon_{\mathrm{PDH}} = -\frac{8\sqrt{P_{\mathrm{c}}\,P_{\mathrm{s}}}\,\nu_0}{lw}\left[\frac{\delta\nu}{\nu_0} + \frac{\delta l}{l_0}\right] \tag{3.2}$$

In case of a closed servo loop, the fractional frequency deviation from cavity resonance is much smaller then the fractional length fluctuation of the cavity, $\delta\nu/\nu_0 \ll \delta l/l_0$ and thus we get from equation 3.1 and 3.2 that the laser instability only depends on the fractional length stability of the cavity $\delta\nu/\nu_0 = -\delta l/l_0$. Hence, the fractional length fluctuations of the cavity become visible in the power spectral density (PSD) of the fractional frequency stability of the laser $S_{\mathrm{y,L}}$.

### 3.1.2. Residual amplitude modulation

In practice, residual amplitude modulation (RAM) at the modulation frequency $f_{\mathrm{m}}$, which is an unavoidable byproduct of phase modulation, affects the PDH error signal and thus degrades the instability of the laser light [77]. Thus, the instability caused by RAM must be reduced below the cavity's instability to operate the laser system at the thermal noise floor limit, see section 5.5. RAM appears as the amplitude $I_0^{(\mathrm{ph})}$ of an additional photo-current $I^{(\mathrm{ph})}(f_{\mathrm{m}})$ in the PDH detection [77, 78] and adds an offset $\Delta\varepsilon_{\mathrm{RAM}} \propto I_0^{(\mathrm{ph})}$ to the PDH error signal $\varepsilon_{\mathrm{PDH}}$. This results in a shifted error signal $\varepsilon_{\mathrm{tot}} = \varepsilon_{\mathrm{PDH}} + \Delta\varepsilon_{\mathrm{RAM}}$ and thus a frequency offset $\Delta\nu_{\mathrm{RAM}}$ of the laser frequency compared to cavity resonance, see figure 3.2 [77, 74]. A detailed quantitative description and analysis how RAM affects the PDH signal is given for example in Shen et al. [74].

As long as the RAM's amplitude is constant and the resulting frequency offset $\Delta\nu_{\mathrm{RAM}}$ is much smaller than the cavity's linewidth $lw$, RAM results in a constant frequency offset $\Delta\nu_{\mathrm{RAM}}$ but does not degrade the laser stability. In practice, the RAM's amplitude is fluctuating and thus the laser stability is degraded as the locking point is constantly shifted in frequency due to the fluctuating offset $\Delta\varepsilon_{\mathrm{RAM}}$. This degradation is intrinsically lower for cavities with a steeper error signal slope, as the same change in

et al. [76].

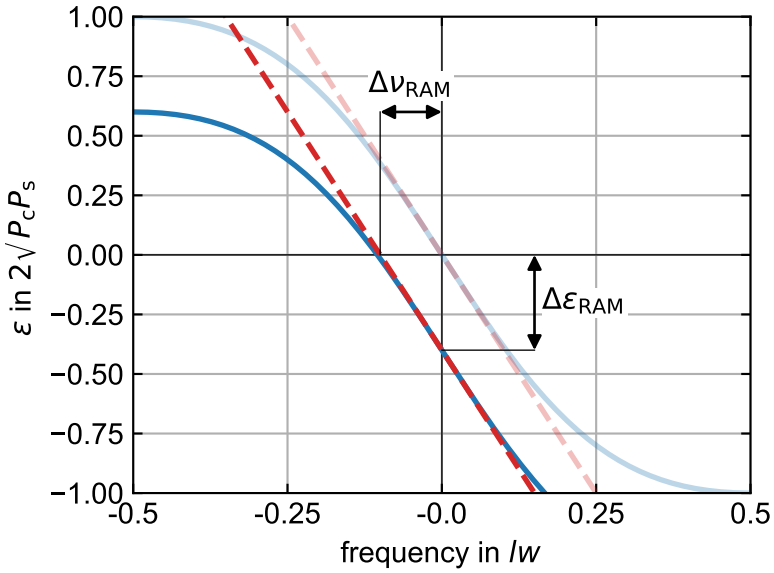


Figure 3.2.: The light red dashed and blue solid line show the PDH error signal $\varepsilon_{\mathrm{PDH}}$ with the same approximations as in figure 3.1 for frequencies within the cavity linewidth $\pm lw/2$. The saturated red dashed and blue solid line show the error signal $\varepsilon_{\mathrm{tot}}$ shifted by the offset $\Delta\varepsilon_{\mathrm{RAM}}$ caused RAM, which results in turn in a frequency shift $\Delta\nu_{\mathrm{RAM}}$ as the locking point is shifted.

RAM offset $\Delta\varepsilon_{\mathrm{RAM}}$ results in a smaller frequency shift $\Delta\nu_{\mathrm{RAM}}$. As the steepness of the error signal close to resonance is inversely proportional to the cavity's linewidth $lw$, see equation 3.2, cavities with higher finesse $\mathcal{F}$ and longer length $l_0$ show a lower sensitivity to RAM. This affects especially transportable laser systems, which in general use shorter cavities.

The most obvious and generally the largest contribution to RAM is caused by the natural birefringence of the EOM. The simplified setup in figure 3.3 provides a qualitative picture of this RAM contribution. Both the extraordinary axis of the EOM, drawn in green, and the applied electric field $E_{\mathrm{x}}$ are perfectly aligned with the $x$-direction. The light entering the EOM is linearly polarized along the polarization axis of a polarizer, drawn in blue, in front of the EOM and the light leaving the EOM is passing through a polarization analyzer, drawn in orange. The polarizer as well as the analyzer can be imagined as polarizing beamsplitters. The polarization axes of the polarizer and the analyzer, respectively, are tilted under the angles $\theta_{\mathrm{p}}$ and $\theta_{\mathrm{a}}$ with respect to the $x$-direction. Thus, the polarization of the entering light is slightly tilted from the extraordinary axis of the EOM. The phase shifts experienced by the light fractions polarized along the extraordinary and ordinary axis differ by $\Delta\phi_{\mathrm{e,o}}$ due to the birefringence of the EOM's crystal. As the phase shift of the extraordinary light is modulated with the frequency $f_{\mathrm{m}}$, the phase difference $\Delta\phi_{\mathrm{e,o}}$ is also modulated with the frequency $f_{\mathrm{m}}$ and thus the polarization of the combined light wave after the EOM changes with the modulation frequency $f_{\mathrm{m}}$. This polarization modulation is trans-

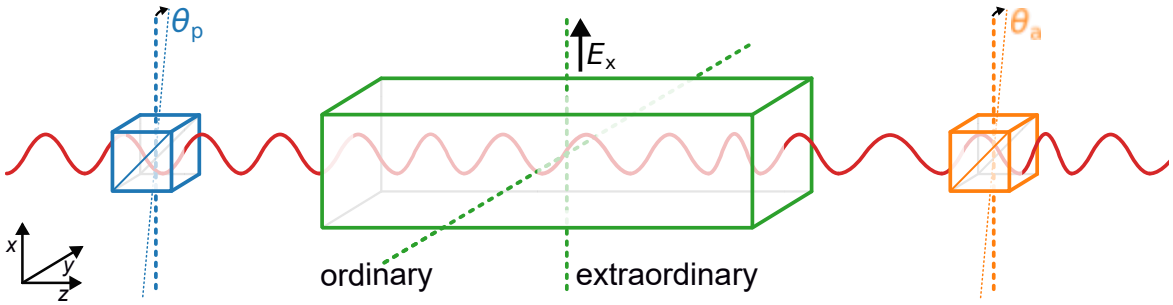


Figure 3.3.: Schematic sketch of an EOM's crystal (green) with its ordinary and extraordinary axes. The extraordinary axes is aligned with the x-direction as well as the applied electric field. A polarizer (blue) and an analyzer (orange) are placed before and after the crystal, respectively. The polarization axes of the polarizer and analyzer are aligned with the x axes if the angles $\theta_\mathrm{p} = 0$ and $\theta_\mathrm{a} = 0$, respectively. The angles $\theta_\mathrm{p}$ and $\theta_\mathrm{a}$ indicate a tilt of the polarization axes with respect to the x-direction in the x-y-plane. The light (red) is traveling along the z-axis.

ferred into an amplitude modulation with the modulation frequency $f_\mathrm{m}$ when passing through the analyzer and appears as photo current $I^{(\mathrm{ph})}(f_\mathrm{m})$ on a potential PD placed behind the analyzer as done in the PDH signal detection. The photo-current $I^{(\mathrm{ph})}(f_\mathrm{m})$ is given in equation 3.3 as derived in Wong and Hall [77].

$$I^{(\mathrm{ph})}(f_\mathrm{m}) = -\sin(2\theta_\mathrm{p})\,\sin(2\theta_\mathrm{a})\,|\epsilon_{\mathrm{x},0}|^2\,J_1^{(\mathrm{Bes})}(M)\,\sin(2\pi f_\mathrm{m} t)\,\sin(\Delta\phi_{\mathrm{e,o}}) \tag{3.3}$$

$$= I_0^{(\mathrm{ph})}\sin(2\pi\, f_\mathrm{m}\, t) \tag{3.4}$$

$$J_1^{(\mathrm{Bes})}(M) = \frac{1}{2\pi}\int_{-\pi}^{\pi}\exp(i[M\sin(\phi) - \phi])\,\mathrm{d}\phi \tag{3.5}$$

$\epsilon_{\mathrm{x},0}$ is the amplitude of the incident light field polarized along the x-axis, $J_1^{(\mathrm{Bes})}$ is the first order Bessel function and $M$ is the modulation depth. To not degrade the laser stability, the amplitude $I_0^{(\mathrm{ph})}$ has to be both constant and sufficiently small. Therefore, the parameters, $\theta_\mathrm{p}$, $\theta_\mathrm{a}$, $\epsilon_{\mathrm{x},0}$, $M$ and $\Delta\phi_{\mathrm{e,o}}$, have to stay constant, which requires a stabilization or the stability of several physical quantities that affect the crucial parameters like laser power, scattering, seismic noise, the radio frequency (RF)-power of modulation field $E_\mathrm{x}$ and environmental temperature [77].

One approach is to reduce initial RAM passively by separating the extraordinary and ordinary light of the EOM by using special crystal geometries, thus suppressing the polarization noise behind the EOM [79–83]. Additionally, the polarization axis of the polarizer and analyzer should be carefully aligned with the EOM's extraordinary axis to even further reduce the RAM. Note that only an alignment of the angles is generally not sufficient. Moreover, the EOM should be temperature stabilized to avoid large RAM fluctuations resulting from the temperature dependence of the EOM's birefringence. Alternatively, a crystal material with low temperature dependence of

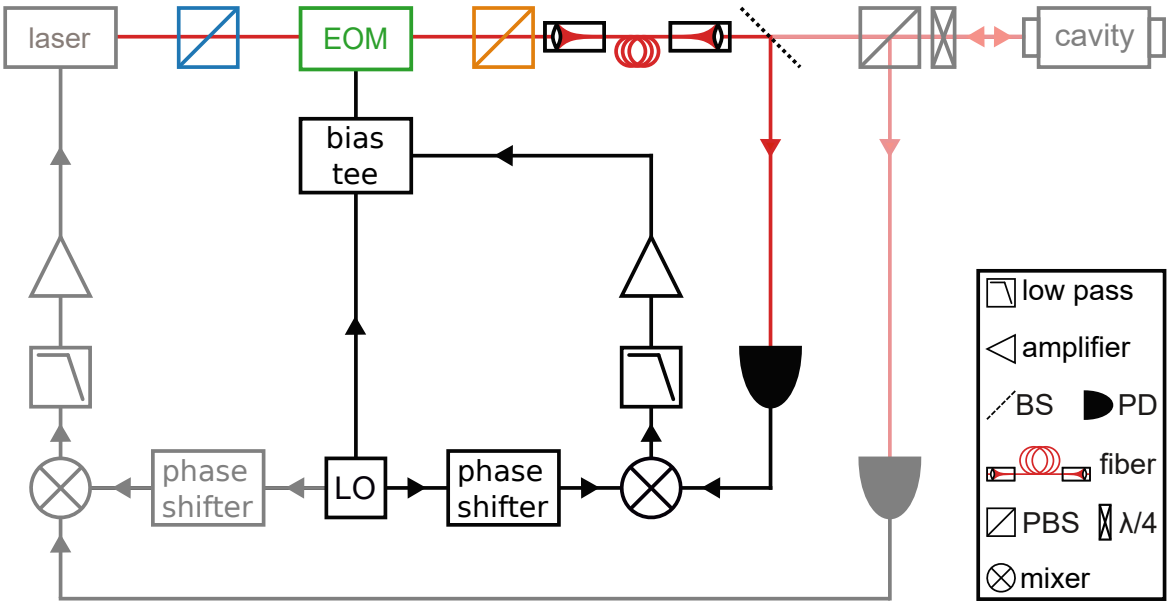


Figure 3.4.: Schematic sketch of an active RAM control. The deep colored componetns belong to the active RAM stabilization and the pale colored components belong to the PDH stabilization. A detailed description is given in the text.

the birefringence is used [83]. Besides the EOM itself also other birefringent materials, like optical fibers, before and after the EOM would cause polarization noise and hence contribute to RAM. Thus, putting the polarizer and analyzer shortly before and after the EOM effectively reduces the amount of optical path length that contributes to RAM and potentially needs temperature stabilization.

Alternatively, an active control [77, 84, 78, 85, 86] can be implemented as shown in figure 3.4. Two PBS are placed close to the EOM to reduce the optical path length that contributes to RAM and an optical fiber is used for spatial filtering as explained later. Even if in principle only the PBS after the EOM, the analyzer, is needed to make the active control work, the PBS before the EOM, the polarizer, and spatial filtering are often crucial to suppress the RAM sufficiently in practice. At some point between the analyzer and the optical cavity, a part of the light is split off and is reflected onto a PD, whose signal is processed equivalently to the PDH PD signal. Hence, the RAM, which is in-phase with the PDH signal, is detected. The resulting correction signal around DC is applied to the EOM via a bias tee. This additional DC voltage affects the phase shift $\Delta\phi_{\mathrm{e,o}}$ and thus is used to control $\Delta\phi_{\mathrm{e,o}}$ to zero.

The performance of the active stabilization depends on a uniform spatial distribution of the RAM. A non perfect beam profile or a non uniform RF field in the EOM due to, for example defects of the crystal, result in a non uniform distribution of the RAM and thus lead to different RAM signals on the PDH PD and the RAM PD. This difference due to a non uniform distribution cannot be compensated by an active control. Therefore, spatial filtering, for example with an optical fiber behind the EOM,

can be used to avoid a non uniform distribution. This RAM would not only appear on the in-phase demodulated signal but also on the quadrature signal. For a non perfect dispersion signal in the PDH lock also RAM in the quadrature component would affect the locking point. An approach stabilizing both the in-phase and the quadrature component can be found in Zhang et al. [78]. Especially to improve the stability on long time scales >10 s, a stabilization of the quadrature component might be interesting [78].

Besides RAM caused by the natural birefringence of the EOM, RAM can be caused by étalons. If RAM is thought of as side bands having not exactly the same amplitude or being not exactly opposite in phase, obviously an étalon, which has a frequency dependent amplitude and phase response, affects the sideband's amplitude and phase differently and thus gives rise to RAM. This RAM can not at all or only partly be reduced by an active stabilization [74]. Therefore, étalons should strictly be avoided, for example by tilting potential parallel surfaces or implementing optical isolators.

Recently, a completely different approach for suppression of RAM effects was given by Shi et al. [79]. They state that frequency shifts caused by RAM are not only related to the amplitude of the RAM, but also to a conversion factor defined by the cavity's mode matching and impedance matching. Thus, frequency shifts caused by RAM could also be suppressed with a cavity design reducing this conversion factor to zero [79]. However, this approach has not yet been demonstrated for cavities with an instability below $10^{-15}$.

### 3.1.3. Fundamental shot noise limit

The fundamental limit of the PDH stabilization is defined by the quantum nature of light and the resulting shot noise affecting the error signal. The fractional frequency noise PSD $S_{\mathrm{y,SN}}$ caused by shot noise is given in equation 3.6 derived from the equations given by Black [41].

$$S_{\mathrm{y,SN}} = \frac{h\,c^2}{8^2\,\mathcal{F}^2\,\nu_0\,P_{\mathrm{c}}} \tag{3.6}$$

With $P_{\mathrm{c}} = 10\,\mu\mathrm{W}$, $\mathcal{F} = 3 \cdot 10^5$ and $\nu_0 = 215\,\mathrm{THz}$, the PSD $S_{\mathrm{y,SN}}$ is in the order of $10^{-39}$, which is orders of magnitude below the noise floor of today's best cavities $S_{\mathrm{y}}(1\,\mathrm{Hz}) \approx 10^{-33}$ [44]. Therefore, as long as the power $P_{\mathrm{c}}$ is not much smaller than 10 µW, the achievable laser frequency stability using the PDH technique is limited by the cavity noise, whose fundamental limit is defined by the thermal noise in the cavity components.

## 3.2. Thermal noise in optical cavities

Thermal noise, also called thermodynamic noise, defines the lower limit for the clock laser instability as it results in length fluctuations of the cavity. Thermal noise is composed of several different kinds of noise such as Brownian, thermorefractive (TR)

and thermoelastic (TE) noise. An overview of the equations of thermal noise was already given in previous works, for example Chalermsongsak et al. [87], Gorodetsky [88] and Martin [89]. In this section, the equations used in this thesis are given and differences from previous publications are indicated.

Commonly, length fluctuations are expressed as the one-sided PSD of length fluctuations $S_\mathrm{x}$. $S_\mathrm{x}$ can be transferred to the one-sided PSD of fractional frequency fluctuations $S_\mathrm{y}$, the Allan deviation (ADEV) $\sigma_\mathrm{y}$ or the modified Allan deviation (mADEV) $\mathrm{mod}\,\sigma_\mathrm{y}$, which are more common quantities in the field of optical clocks. By dividing the PSD of length fluctuations $S_\mathrm{x}$ by the square of the mirror distance $l_0$, one gets the PSD of fractional length and therefore the PSD of fractional frequency fluctuations $S_\mathrm{y}$ as given in equation 3.7. From $S_\mathrm{y}$, the ADEV and the mADEV can be calculated [62], given in equation 3.8 and equation 3.9.

$$S_\mathrm{y} = S_\mathrm{x}/l_0^2 \tag{3.7}$$

$$\sigma_\mathrm{y}^2 = 2\int_0^\infty \frac{\sin^4(\pi\, f\, \tau)}{[\pi\, f\, \tau]^4}\, S_\mathrm{y}(f)\,\mathrm{d}f \tag{3.8}$$

$$\mathrm{mod}\,\sigma_\mathrm{y}^2 = 2\int_0^\infty \frac{\sin^6(\pi\, f\, \tau)}{[\pi\, f\, \tau]^4}\, S_\mathrm{y}(f)\,\mathrm{d}f \tag{3.9}$$

### 3.2.1. Brownian noise

Brownian noise is caused by Brownian motion, which is linked to the mechanical loss in a system [90, 91]. Its displacement noise $S_\mathrm{x,B}(f)$ is dependent on elastic properties of the cavity material (Young's modulus $Y$ and Poisson's ratio[5] $\eta$), the mechanical loss factor or angle $\Phi$, and the temperature $T$. The mechanical loss factor, which describes the damping in a material, is the reciprocal of the quality factor. A lower loss factor corresponds to a lower rate of energy loss.

The impact of the Brownian noise on the cavity's length instability as seen by the laser beam is estimated following the approach by Levin [92][6]. This approach utilizes the fluctuation-dissipation theorem to derive the PSD of the length fluctuations through the following thought experiment. First, it is assumed that a pressure variation $p(r,t)$ with the frequency of interest and a distribution following the beam intensity profile of the light probing the cavity is acting on the mirror surface. For a Gaussian beam profile, the amplitude $p_0(r)$ of the oscillating pressure $p(r,t)$ is given in equation 3.10.

$$p_0(r) = \frac{2\,F_0}{\pi\, w^2} e^{-\frac{2\,r^2}{w^2}} \tag{3.10}$$

[5] Commonly, $\sigma$ or $\nu$ are used as variables for the Poisson's ratio in the literature. As these variables represent in this work the ADEV and the optical frequency, $\eta$ is used instead.

[6] The corrections pointed out by Liu and Thorne [93] in their reference 6 are considered in this work.

$F_0$ is the amplitude of the oscillating force applied to the surface, $w$ is the $1/e^2$ beam radius, and $r$ is the spatial coordinate. Second, the average power dissipated in the cavity assuming homogeneous dissipation under the action of the oscillating pressure $p(r,t)$ is calculated. It is proportional to the material's mechanical loss factor $\Phi$ and the maximum elastic strain energy $W_0$, which is the energy of elastic deformation when the pressure $p_0(r)$ is applied to the surface. Third, inserting everything into the fluctuation-dissipation theorem and applying the conversion from equation 3.7 results in equation 3.11.

$$S_{\mathrm{y,B}} = \frac{4\,k_{\mathrm{B}}\,T}{\pi\,f\,F_0^2}\,W_0\frac{\Phi}{l_0^2} \tag{3.11}$$

$k_{\mathrm{B}}$ is the Boltzmann constant. As the elastic strain energy $W_0$ scales with $F_0^2$, the PSD $S_{\mathrm{y,B}}$ is independent of the assumed test force $F_0$. The total Brownian noise $S_{\mathrm{y,B}}$ is the sum of the Brownian noise contributions of the cavity components, which are the spacer $S_{\mathrm{y,B}}^{(\mathrm{sp})}$, the mirror substrates $2\cdot S_{\mathrm{y,B}}^{(\mathrm{sb})}$, and the mirror coatings $2\cdot S_{\mathrm{y,B}}^{(\mathrm{ct})}$.

$$S_{\mathrm{y,B}} = S_{\mathrm{y,B}}^{(\mathrm{sp})} + 2S_{\mathrm{y,B}}^{(\mathrm{sb})} + 2S_{\mathrm{y,B}}^{(\mathrm{ct})} \tag{3.12}$$

$$= \frac{4\,k_{\mathrm{B}}\,T}{\pi\,f\,F_0^2 l_0^2}[W_0^{(\mathrm{sp})}\,\phi_{\mathrm{sp}} + 2\,W_0^{(\mathrm{sb})}\,\phi_{\mathrm{sb}} + 2\,W_0^{(\mathrm{ct})}\,\phi_{ct}] \tag{3.13}$$

Furthermore, the maximum elastic strain energy $W_0$ depends on the geometry and material properties of the cavity components. It can be calculated either analytically [94, 95] or using the finite element method (FEM) [96]. Compared to the analytical solutions, FEM simulations give a more accurate result for the maximum elastic strain energy $W_0$ of the cavity components and can be easily applied to complex geometries. However, analytical equations nicely show the correlations between the properties of the cavity and the resulting Brownian noise.

For a cylindrically shaped spacer, an estimation of the maximum elastic strain energy $W_0^{(\mathrm{sp})}$ is given by Numata et al. [95], with the assumption that the mirrors have a small effect on the spacer. The resulting noise $S_{\mathrm{y,B}}^{(\mathrm{sp})}$ is given in equation 3.14. $A_{\mathrm{sp}}$ is the area of the front face of the spacer[7]. This equation holds for the central region of the spacer while it fails close to the spacer ends, where the mirrors are contacted to the spacer [96]. The so called excess energy, which appears close to the ends of the spacer, results in an underestimation of the analytically calculated spacer noise compared to FEM simulations.

For a half infinite mirror substrate, meaning the mirror has an infinite radius and infinite depth from the surface, the expected noise $S_{\mathrm{y,B}}^{(\mathrm{sb})}$ is given in equation 3.15. The noise calculated this way is an overestimation compared to the noise of the actual finite cylindrical mirror. However, it is a good estimation for the noise if the beam radius is much smaller than the mirror radius [92, 94].

For the mirror coating, Harry et al. [97] and Nakagawa et al. [98] give an equation based on a half infinite mirror substrate assuming a homogeneous loss angle $\phi_{\mathrm{ct}}$ of the

[7] For a cylindrical spacer with a hole, $A_{\mathrm{sp}} = \pi\left[r_{\mathrm{out}}^2 - r_{\mathrm{in}}^2\right]$

coating with a thickness of $d_{ct}$ and the same elastic properties as the mirror substrate, see equation 3.17. Thus, the Brownian noise contribution of the mirror coatings $S_{\mathrm{y,B}}^{(\mathrm{ct})}$ depends rather on the elastic properties of the substrates' material than on the elastic properties of the coating material. A correction for different elastic properties of substrate and coating is given by Harry et al. [97], see equation 3.16.

$$S_{\mathrm{y,B}}^{(\mathrm{sp})} = \frac{4\,k_{\mathrm{B}}\,T}{\pi\,f}\,\frac{1}{2\,\pi\,Y_{\mathrm{sp}}}\,\frac{1}{A_{\mathrm{sp}}\,l_0}\,\phi_{\mathrm{sp}} \tag{3.14}$$

$$S_{\mathrm{y,B}}^{(\mathrm{sb})} = \frac{4\,k_{\mathrm{B}}\,T}{\pi\,f}\,\frac{1-\eta_{\mathrm{sb}}^2}{2\,\sqrt{\pi}\,Y_{\mathrm{sb}}}\,\frac{1}{w\,l_0^2}\,\phi_{\mathrm{sb}} \tag{3.15}$$

$$S_{\mathrm{y,B}}^{(\mathrm{ct})} = \frac{2\,k_{\mathrm{B}}\,T}{\pi\,f}\,\frac{Y_{\mathrm{ct}}^2\,[1+\eta_{\mathrm{sb}}]^2\,[1-2\eta_{\mathrm{sb}}]^2 + Y_{\mathrm{sb}}^2\,[1+\eta_{\mathrm{ct}}]^2\,[1-2\eta_{\mathrm{ct}}]}{\pi\,Y_{\mathrm{sb}}^2 Y_{\mathrm{ct}}(1-\eta_{\mathrm{ct}}^2)}\,\frac{d_{\mathrm{ct}}}{w^2\,l_0^2}\,\phi_{\mathrm{ct}} \tag{3.16}$$

$$= \frac{4\,k_{\mathrm{B}}\,T}{\pi\,f}\,\frac{1-\eta_{\mathrm{sb}}-2\eta_{\mathrm{sb}}^2}{\pi\,Y_{\mathrm{sb}}}\,\frac{d_{\mathrm{ct}}}{w^2\,l_0^2}\,\phi_{\mathrm{ct}} \qquad \text{for } Y_{\mathrm{sb}} = Y_{\mathrm{ct}} \text{ and } \eta_{\mathrm{sb}} = \eta_{\mathrm{ct}} \tag{3.17}$$

Brownian noise results in flicker frequency noise of the cavity's length and thereby of the fractional length stability and of the fractional frequency stability. Thus, the PSD of the fractional frequency noise $S_{\mathrm{y,B}}$ caused by Brownian noise shows the typical $1/f$ behavior of ultra-stable lasers, whose fractional frequency stability is limited by Brownian noise. For all three components, the PSD of the fractional frequency noise $S_{\mathrm{y,B}}$ caused by Brownian noise decreases with higher spacer length $l_0$ and higher beam waist $w$, which also increases with higher spacer length $l_0$ and higher radius of curvature (ROC) of the mirror as derived in appendix A.4. This makes longer cavites beneficial to reduce the fractional frequency noise $S_{\mathrm{y,B}}$ caused by Brownian noise. Also, cavities operated at lower temperature $T$ result in a lower Brownian noise. By choice of material, the Brownian noise is affected by the mechanical loss factor $\Phi$, Poisson's ratio $\eta$ and Young's modulus $Y$. Especially, low-mechanical-loss materials are of interest to reduce the Brownian noise since the loss factor differs by orders of magnitude between suitable cavity materials as shown in section 3.3.

### 3.2.2. Thermoelastic and thermorefractive noise

Thermoelastic (TE) and thermorefractive (TR) noise, collectively known as thermo-optic (TO) noise, are caused by thermal dissipation that results in temperature fluctuations in the cavity components [99]. These thermodynamically driven temperature fluctuations cause on the one hand thermal expansion, leading to TE noise, and on the other hand a variation of the refractive index, leading to TR noise, which both result in effective length changes of the cavity, but with opposite sign, resulting in a partial cancellation for typically used cavity materials.

Thermal expansion of all cavity components affect the distance between the two mirror surfaces and thus the cavity length as seen by the laser beam due to deformation and strain in the cavity components. The variation in the refractive index has only an impact for components that interact with the light, which are obviously the mirror

coating and the substrate. Variation of the refractive index of the mirror substrate results in an optical path length fluctuation between the cavity and the laser, causing Doppler broadening equivalent to the Doppler broadening introduced by an optical fiber between the cavity and the laser as discussed in section 4. However, as the light only passes the mirror substrate when entering or leaving the cavity, the TR noise contribution caused by the substrate is negligibly small compared to its TE noise contribution $S_{\mathrm{y,TE}}^{(\mathrm{sb})}$ [100, 101]. As the laser beam penetrates into mirror coating being reflected by them, a change in reflective index of the mirror coating does cause a change in optical path length and thus results in a change in cavity length as seen by the laser light. Since the mirror coating's TE and TR noise have approximately equal values, but can be treated coherently with relative minus sign, the TO noise $S_{\mathrm{y,TO}}^{(\mathrm{ct})}$ of the mirror coating is reduced [88, 102, 103]. The total TO noise of all cavity components adds up to $S_{\mathrm{y,TO}}$:

$$S_{\mathrm{y,TO}} = S_{\mathrm{y,TE}}^{(\mathrm{sp})} + 2\,S_{\mathrm{y,TE}}^{(\mathrm{sb})} + 2\,S_{\mathrm{y,TO}}^{(\mathrm{ct})} \tag{3.18}$$

For TO noise in general, the adiabatic limit and the non-adiabatic case show a different frequency dependence. The adiabatic limit describes the range of Fourier frequencies where an averaging effect takes place, because the thermal diffusion length $l_{\mathrm{th}}$ is much smaller than the light's spot size[8] on the mirror $w$, $l_{\mathrm{th}} \ll w$. The thermal diffusion length describes the average distance the temperature fluctuations travel during the characteristic time at Fourier frequency $f$ and is defined by the thermal conductivity $\kappa$ and heat capacity per volume $C$ of the material: $l_{\mathrm{th}} = \sqrt{\kappa/[C\,2\pi\,f]}$. For much smaller thermal diffusion lengths compared to the physical dimensions or probed areas of the components, a temporal averaging takes place and the TO noise converges against the so-called adiabatic limit. This is for example the case if the diffusion length $l_{\mathrm{th}}$ is much smaller than the dimension of the contact area between mirror substrate and spacer. With typical contact dimensions in the cm range, this results in a cut-off frequency for the adiabatic limit of around 1 mHz using $f_{\mathrm{T}} = \frac{\kappa}{2\pi\,l_{\mathrm{th}}^2\,C}$ with $l_{\mathrm{th}} = 1\,\mathrm{cm}$, $\kappa = 1.38\,\mathrm{W\,K^{-1}\,m^{-1}}$ and $C = 1.7\,\mathrm{MJ\,m^{-3}\,K^{-1}}$ taken from table B.1. As typically the cavity's length stability for Fourier frequencies below 1 mHz is limited by other effects like fluctuations of the average cavity temperature, here only the adiabatic limit is of interest. The spacer's TE noise for the adiabatic limit and the quasi-static case where the time required for sound to travel across the spacer is significant shorter than the time of interest is given in equation 3.19 with the displacement field $\vec{u}$. [93, equation (3) and (13)].

$$S_{\mathrm{y,TE}}^{(\mathrm{sp})} = \frac{2\,k_{\mathrm{B}}\,T^2\,\kappa_{\mathrm{sp}}}{\pi^2\,f^2}\left[\frac{Y_{\mathrm{sp}}\,\alpha_{\mathrm{sp}}}{[1-2\,\eta_{\mathrm{sp}}]\,C_{\mathrm{sp}}}\right]^2 \frac{1}{l_0^2}\frac{\int \vec{\nabla}\,\vec{\nabla}\,\vec{u}\,\mathrm{d}V}{F_0^2} \tag{3.19}$$

[8] Note that Braginsky et al. [99, 104], Braginsky and Vyatchanin [105], Cerdonio et al. [106], and Liu and Thorne [93] use as spot size the radius $w_{1/\mathrm{e}}$ at which the intensity of the beam falls off to $1/\mathrm{e}$, while this work, Black et al. [107], Chan et al. [108], Chalermsongsak et al. [87], Evans et al. [103], Gorodetsky [88], Martin [89], and Numata et al. [109] use as spot size the radius $w$ at which the intensity falls off to $1/\mathrm{e}^2$ is. $w_{1/\mathrm{e}} = w/\sqrt{2}$. This was also pointed out by Black et al. [110]

The TE noise of the spacer reduces with larger heat capacity per volume $C_{\mathrm{sp}}$, smaller thermal conductivity $\kappa_{\mathrm{sp}}$, smaller Young's modulus $Y_{\mathrm{sp}}$ and smaller cofficient of thermal expansion (CTE) $\alpha_{\mathrm{sp}}$. A low CTE $\alpha_{\mathrm{sp}}$ is not only advantageous to reduce the the TE noise but also to reduce the impact of external temperature fluctuation on the cavity's length stability as described in section 5.9. Therefore often materials with CTE zero crossings are used as spacer material, like Silicon or ultra low expansion (ULE) glass, and the cavity is operated at its CTE zero crossing temperature, at which the CTE of the cavity reduces to zero. Thus, also the spacer's CTE and thus its TE noise reduces significantly for mixed material cavities or even reduces to zero for pure material cavities as described in section 3.3.

The substrate's TE noise is given for the case of a half-infinite mirror substrate in equation 3.20 [88, 99, 106]. The equations for TE noise in the adiabatic limit are given in Gorodetsky [88] and Braginsky et al. [99]. The correction $J^{(\mathrm{Cer})}$ for the non-adiabatic regime is given by Cerdonio et al. [106][9]. Here, the expansion of the beam waist $w$ and thus the probed mirror area define the cut-off frequency[10] $f_{\mathrm{T}}^{(\mathrm{sb})}$ as shown in equation 3.24 [99]. Typical cut-off frequencies for room temperature cavities are around 1 Hz using the values from table B.1 and 3.1.

$$S_{\mathrm{y,TE}}^{(\mathrm{sb})} = \frac{4\,k_{\mathrm{B}}\,T^2}{\sqrt{\pi}}\,\frac{\alpha_{\mathrm{sb}}^2\,(1+\eta_{\mathrm{sb}})^2\,w}{\kappa_{\mathrm{sb}}}\,\frac{1}{l_0^2}\,J^{(\mathrm{Cer})}\left(f/f_{\mathrm{T}}^{(\mathrm{sb})}\right) \tag{3.20}$$

$$J^{(\mathrm{Cer})}(f/f_{\mathrm{T}}^{(\mathrm{sb})}) = \left[\frac{2}{\pi^3}\right]^{\frac{1}{2}} \int_0^\infty \mathrm{d}u \int_{-\infty}^\infty \mathrm{d}v \frac{u^3\,\exp\left(-u^2/2\right)}{[u^2+v^2][\{u^2+v^2\}^2+\{f/f_{\mathrm{T}}^{(\mathrm{sb})}\}^2]} \tag{3.21}$$

$$J^{(\mathrm{Cer})}(f/f_{\mathrm{T}}^{(\mathrm{sb})}) = \frac{2}{3\sqrt{\pi f/f_{\mathrm{T}}^{(\mathrm{sb})}}} \qquad \mathrm{for} f/f_{\mathrm{T}}^{(\mathrm{sb})} \ll 1 \tag{3.22}$$

$$J^{(\mathrm{Cer})}(f/f_{\mathrm{T}}^{(\mathrm{sb})}) = \frac{1}{\left[f/f_{\mathrm{T}}^{(\mathrm{sb})}\right]^2} \qquad \mathrm{for} f/f_{\mathrm{T}}^{(\mathrm{sb})} \gg 1 \qquad \text{(adiabatic limit)} \tag{3.23}$$

$$f_{\mathrm{T}}^{(\mathrm{sb})} = \frac{\kappa_{\mathrm{sb}}}{\pi\,w^2\,C_{\mathrm{sb}}} \tag{3.24}$$

A correction for a finite substrate is given by Liu and Thorne [93]. The error for a half-infinite compared to a finite substrate is in the order of a few percent for common mirror substrates in ultra-stable cavities.

Especially, the CTE $\alpha_{\mathrm{sb}}$ has a big impact on the substrates TE noise as it enters quadratically and varies over wide range for different materials in contrast to the heat capacity per volume $C_{\mathrm{sb}}$, thermal conductivity $\kappa_{\mathrm{sb}}$ and Poisson's ratio $\eta_{\mathrm{sb}}$. In contrast to the spacer, more often also materials with no CTE zero crossing are used

[9] Note there is a typing error in equation (21) of Cerdonio et al. [106]. The first factor in the equation for $J^{(\mathrm{Cer})}$ should be $\sqrt{2/\pi^3}$ instead of $\sqrt{2/\pi}$, also to fit the curve in figure 1 of Cerdonio et al. [106], as pointed out by Black et al. [110] and Numata et al. [109].

[10] Due to different definitions of spot size radius as described in footnote 8 $l_{\mathrm{th}} = w/\sqrt{2}$ to stay consistent with the definition as used in all previous publications.

as mirror substrate material to profit from other material properties for example a low mechanical loss factor $\phi_{\mathrm{sb}}$ to reduce the Brownian noise contribution of the mirror substrates as described in section 3.3. Thus, the TE noise contribution of the substrate is often larger for mixed-material cavities compared to the TE noise contribution of the spacer.

The coatings' TO noise $S_{\mathrm{y,TO}}^{(\mathrm{ct})}$ is calculated using $S_{\mathrm{T}}$, which is the PSD of the fluctuations of the average temperature, as given in equation 3.25 [87, 89, 103, 104][11] [111][12] with different frequency dependence for the adiabatic limit, see equation 3.28, and non-adiabatic regime, see equation 3.27. Equation 3.25 to 3.29 use the substrate parameters, which need to be corrected through a correction factor as shown below.

$$S_{\mathrm{T}} = \frac{2\sqrt{2}k_{\mathrm{B}}T^2}{\pi\kappa_{\mathrm{sb}}w} J^{(\mathrm{Mar})}(f/f_{\mathrm{T}}^{(\mathrm{sb})}) \tag{3.25}$$

$$J^{(\mathrm{Mar})}(f/f_{\mathrm{T}}^{(\mathrm{sb})}) = \Re\left[\int_0^\infty u\exp(-u^2/2)\sqrt{\frac{u^2 + if/f_{\mathrm{T}}^{(\mathrm{sb})}}{u^4 + [f/f_{\mathrm{T}}^{(\mathrm{sb})}]^2}}\mathrm{d}u\right] \tag{3.26}$$

$$J^{(\mathrm{Mar})}(f/f_{\mathrm{T}}^{(\mathrm{sb})}) = \sqrt{\frac{\pi}{2}} \quad \text{for} \quad f/f_{\mathrm{T}}^{(\mathrm{sb})} \ll 1 \tag{3.27}$$

$$J^{(\mathrm{Mar})}(f/f_{\mathrm{T}}^{(\mathrm{sb})}) = \frac{1}{\sqrt{2f/f_{\mathrm{T}}^{(\mathrm{sb})}}} \quad \text{for} \quad f/f_{\mathrm{T}}^{(\mathrm{sb})} \gg 1 \quad \text{(adiabatic limit)} \tag{3.28}$$

$$f_{\mathrm{T}}^{(\mathrm{sb})} = \frac{\kappa_{\mathrm{sb}}}{\pi\omega^2 C_{\mathrm{sb}}} \tag{3.29}$$

These equations hold for the assumption that the optical penetration depth of the laser light is much smaller than the beam waist [89]. As for room temperature cavities, penetration depths are below 1 µm and beam waists are typically a few 100 µm, this assumption is fulfilled.

The TE noise for a mirror coating is given in equation 3.30 [105, 112, 103].

$$S_{\mathrm{y,TE}}^{(\mathrm{ct})} = S_{\mathrm{T}}\,\Gamma_{\mathrm{tc}}\left[d_{\mathrm{ct}}\,\alpha_{\mathrm{ct}} - d_{\mathrm{ct}}\,\alpha_{\mathrm{sb}}\,\frac{C_{\mathrm{ct}}}{C_{\mathrm{sb}}}\right]^2 \tag{3.30}$$

$\Gamma_{\mathrm{tc}}$ is the thick coating correction as given by Evans et al. [103], see appendix A.2. Without this correction, the equation only holds for similar elastic properties of the

[11] Martin [89] uses the material properties of the mirror coating ($\kappa_{\mathrm{ct}}$, $C_{\mathrm{ct}}$) to calculate the TO noise of the coating, see his equation 3.27 to 3.32, while Chalermsongsak et al. [87, 111], Evans et al. [103] and Gorodetsky [88] use the material properties of the substrate ($\kappa_{\mathrm{sb}}$, $C_{\mathrm{sb}}$), which especially for aluminium gallium arsenide ($\mathrm{Al_{0.92}Ga_{0.08}As}$)/gallium arsenide (GaAs) mirrors on fused silica (FS) substrates leads to very different results due to one order of magnitude difference in the thermal conductivity $\kappa$. This work uses the material properties of the substrate and applies the correction factor $\Gamma_{\mathrm{tc}}$, given by Evans et al. [103].

[12] Note there is a typing error in Chalermsongsak et al. [111]. In the line between their equation (5) and (6), the constants $\kappa_s$ and $C_s$ must be used instead of $\kappa_c$ and $C_c$. This leads to the TO curves shown in their figure 1.

mirror coating and substrate. Also note that average values for the CTE $\alpha_{\mathrm{ct}}$ and heat capacity $C_{\mathrm{ct}}$ of the different layers of the mirror coating are used as given by Evans et al. [103] and Fejer et al. [112], see appendix A.3.

The TR noise of a mirror coating is given in equation 3.31 [88, 103].

$$S_{\mathrm{y,TR}}^{(\mathrm{ct})} = S_{\mathrm{T}}\,\Gamma_{\mathrm{tc}}\,\left[\beta_{\mathrm{ct}}\,\lambda_0\right]^2 \tag{3.31}$$

$\beta_{\mathrm{ct}}$ is the effective TR coefficient as given in Evans et al. [103] and Gorodetsky [88], see appendix A.3.

The resulting TO noise is given in equation 3.32 [88, 103].

$$S_{\mathrm{y,TO}}^{(\mathrm{ct})} = S_{\mathrm{T}}\,\Gamma_{\mathrm{tc}}\,\left[d_{\mathrm{ct}}\,\alpha_{\mathrm{ct}} - \beta_{\mathrm{ct}}\,\lambda_0 - d_{\mathrm{ct}}\,\alpha_{\mathrm{sb}}\,\frac{C_{\mathrm{ct}}}{C_{\mathrm{sb}}}\right]^2 \tag{3.32}$$

Note that $S_{\mathrm{T}}$, $\Gamma_{\mathrm{tc}}$, $\alpha_{\mathrm{ct}}$ and $\beta_{\mathrm{ct}}$ depend not only on mirror coating material properties bus also on mirror substrate material properties. Thus, using the same mirror coating material, but different substrate materials can significantly change the TO noise contribution. To reduce TO noise, the layer structure can be optimized, for example by changing the thickness of the covering layer of the mirror coating [88, 103, 87, 111]. This optimization process has to be performed with respect to the frequencies of interest as the resulting TO noise for different layer structures shows a different frequency dependence [88].

## 3.3. Choice of cavity materials

The materials of the cavity components define the thermal noise floor of the cavity through their material properties, but also affect the cavity's vibration sensitivity, sensitivity to laser power fluctuations and temperature fluctuations. Following the equations of section 3.2, low Brownian noise can be reached with a cavity with high mechanical stability, corresponding to low mechanical loss factor $\Phi$, high Young's modulus $Y$ and high Poisson's ratio $\eta$, which is also important to reach low vibration sensitivity, see section 5.7. To reduce cavity instability caused by TO noise, laser power fluctuations and temperature fluctuations, high thermal conductivity $\kappa$, high heat capacity $C$, and a low CTE are beneficial as shown in sections 5.6 and 5.9. Also, operation at low temperature results in lower thermal noise, but is as mentioned in chapter 1 not reasonable for a transportable system.

Fused silica (FS) and ULE glass are potential materials for the mirror substrate and spacer, which are beneficial at room temperature compared to sapphire and silicon, which are used for cryogenic cavities, and zerodur, which is less favourable especially due to its higher mechanical loss factor. The values for FS and ULE glass are given in the appendix in table B.1. For the mirror coating, the material properties of crystalline $Al_{0.92}Ga_{0.08}As$/GaAs and commonly used amorphous tantalum pentoxide ($Ta_2O_5$)/fused silica ($SiO_2$) layers are also shown in table B.1. Crystalline $Al_{0.92}Ga_{0.08}As$/GaAs is beneficial compared to amorphous $Ta_2O_5/SiO_2$ due to its one order of magnitude lower mechanical loss factor [46].

Table 3.1.: Values for thermal noise calculation.

| spacer | value | substrate | value | coating | value | other | value |
|---|---|---|---|---|---|---|---|
| $l_0$ | 20 cm | ROC | 1 m | $N_{\mathrm{L}}$ [a] | 38 | $w$ [d] | 385 µm |
| $r_{\mathrm{out}}$ | 4 cm | - | - | $N_{\mathrm{H}}$ [a] | 39 | $\lambda_0$ | 1397 nm |
| $r_{\mathrm{in}}$ | 0.5 cm | - | - | $d_{\mathrm{ct}}$ [b] | 15.8 µm, 8.5 µm [c] | $T$ | 300 K |

[a] Assuming a coating made of quarter-wave layers starting and ending with a high-reflective-index layer.
[b] Calculated from equation A.22
[c] coating thickness for a $Ta_2O_5/SiO_2$ and a $Al_{0.92}Ga_{0.08}As/GaAs$ mirror, respectively
[d] Calculated from equation A.23 and A.24

Figures 3.5a-c show the calculated noise contributions $S_{\mathrm{y}}$ of the individual cavity components and the resulting ADEV $\sigma_{\mathrm{y}}$ and mADEV mod $\sigma_{\mathrm{y}}$ for a 20 cm long cavity made of different materials. To calculate the thermal noise contributions, the equations of section 3.2 and the values of table 3.1 and B.1 are used.

Figure 3.5 a shows the noise contributions for spacer and substrates both made of ULE glass with $Ta_2O_5/SiO_2$ mirrors. Here, the Brownian noise of the mirror substrates and coatings have the biggest contribution. To reduce the Brownian noise of the mirror substrate, fused silica is chosen in figure 3.5 b. It has a much lower mechanical loss factor and therefore shows lower Brownian noise, resulting in a lower ADEV and mADEV. However, fused silica has a higher CTE at room temperature than ULE glass, which results in higher TE noise and a higher sensitivity to temperature fluctuations of the resonator. The substrates' TE noise is still well below the coatings' Brownian noise, which makes it a negligible contribution for this cavity. To compensate the higher sensitivity to temperature fluctuations due to the different CTEs of ULE and FS glass, compensation rings of ULE glass can be placed on the backside of the mirror substrates, which results in roughly the temperature sensitivity of a full ULE glass cavity [113]. After reducing the Brownian noise of the substrate, the Brownian noise of the mirror coating is the main contribution as shown in figure 3.5 b. It can be reduced by using $Al_{0.92}Ga_{0.08}As/GaAs$ instead of $Ta_2O_5/SiO_2$ mirror coatings as shown in figure 3.5 c. Here, the FS substrates have the biggest contribution for frequencies below 10 Hz. For high frequencies, the TO noise of the coating is dominating. A successful reduction of the TO noise in crystalline mirrors is shown by Chalermsongsak et al. [111] and would shift the area of frequencies where TO is dominating to around 10 kHz.

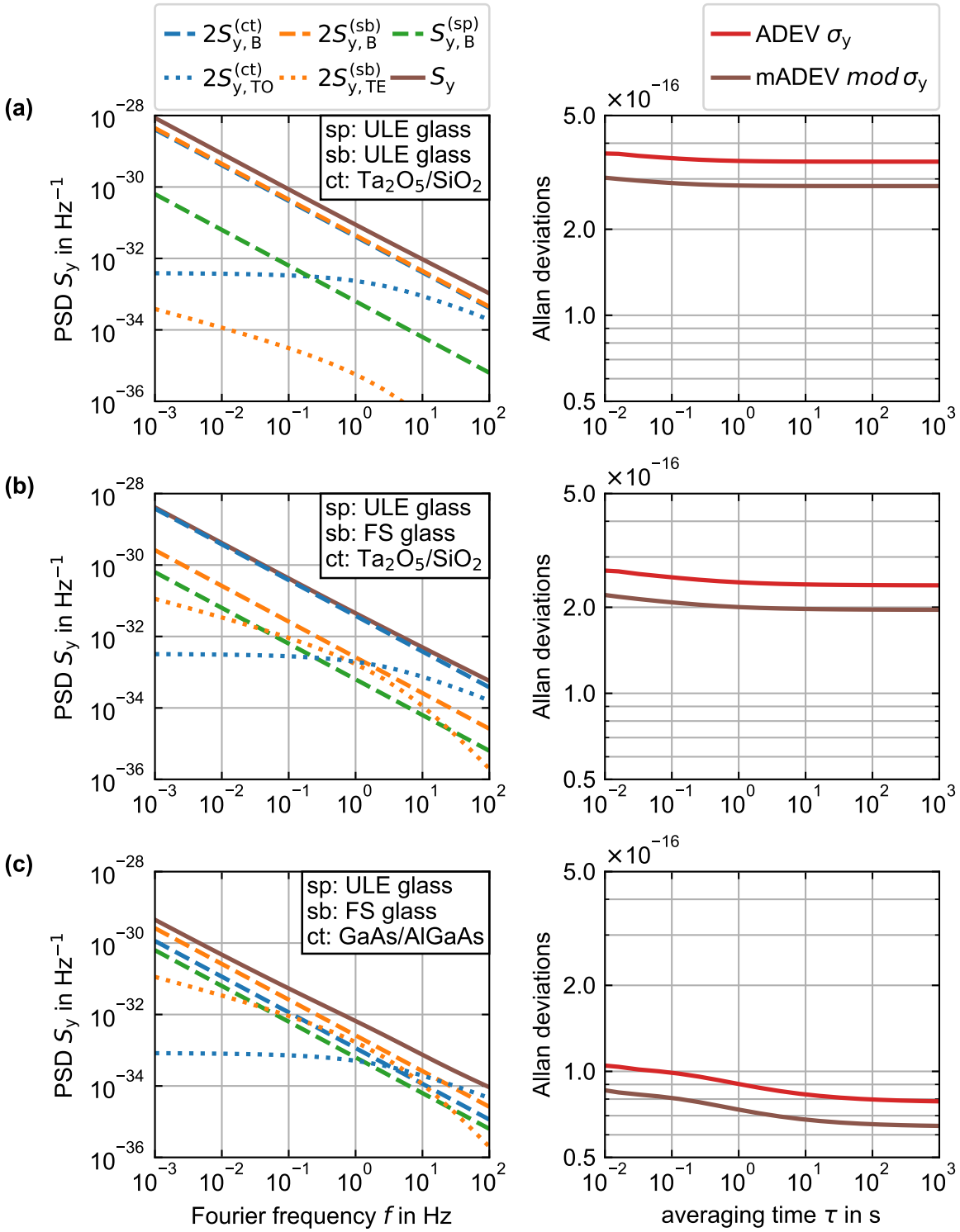


Figure 3.5.: The values in table 3.1 and B.1 and the equations in section 3.2 are used to calculate the ADEV, mADEV and the noise contributions of the single cavity components $S_y$.

# 4. Laser light distribution breadboard

For operating an optical clock, the light of the clock laser has to be distributed to the atoms being interrogated, to the ultra-stable reference cavity for pre-stabilizing the laser light frequency as well as to a second clock or frequency comb for potential clock comparisons. The light is normally traveling to the different components in free space or through optical fibers. Any change in optical path length between the components causes Doppler broadening of the clock laser linewidth. Fluctuations in optical path length result from changes in refractive index or geometrical path length, which can be caused by temperature changes, pressure changes and seismic or acoustic vibrations. The laser linewidth broadening depends on the medium the light is traveling through (e.g. optical fibers or air), the environmental conditions (e.g. air-conditioned laboratory or outdoors) and the distance the light is traveling.

During this work, clock comparisons with PTB's transportable Sr clock [28] were performed in different environments using a clock laser system with an instability of down to $\mathrm{mod}\,\sigma_\mathrm{y} = 3 \cdot 10^{-16}$, as described in Häfner et al. [51], which will be referred to as Sr1. A significant degradation of the stability at one second averaging time of the Sr1 laser system was observed due to a 2 m fiber with no noise compensation outside a well controlled laboratory environment. As the laser system presented in this work, which will be referred to as Sr2, aims for even lower instability and faces similar environments, active fiber noise cancellation must be applied to prevent such a degradation. An overview of different methods of active fiber noise cancellation that can be used for far and near stable-frequency transfer can be found for example in the review paper of Mehlstäubler et al. [15].

A schematic sketch of the phase noise cancellation as realized in this work and first shown by Ye et al. [114] is shown in figure 4.1. The fiber noise cancellation is based on a Michelson interferometer with a very short, extremely stable reference arm and a long arm including the optical fiber. The stability of the reference arm is transferred to the stability of the long arm by phase-stabilizing the light in the long arm to the reference light. For this purpose, the photodiode (PD) detects the beat frequency between the light frequencies of the two arms, from which a control signal is derived with a phase-locked loop (PLL) comparing the PD signal to a stable 100 MHz reference signal[1]. This control signal is applied to the control acousto-optic modulator (cAOM) in the long arm. It is important to note that the light passes both the fiber and the

[1] The reference signal is provided for example by a hydrogen maser or the optical frequency standard itself

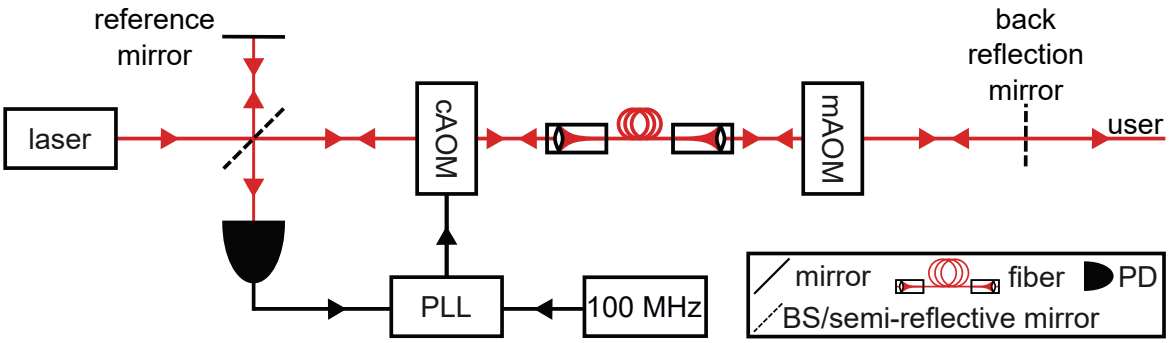


Figure 4.1.: Schematic sketch of a phase noise cancellation.

cAOM twice, meaning that the signal applied to thecAOM compensates one passage through the optical fiber. This way, for the light traveling to the user, the added noise at the back reflection mirror is reduced from the noise in the long arm to the noise in the reference arm. Besides the cAOM, an optional marker AOM (mAOM) is placed at the end of the long arm. It creates a frequency shift between the signal from the back reflection mirror and most other unwanted back reflections, which would otherwise disturb the fiber noise cancellation.

A light-weight, compact, and robust distribution breadboard was designed for stable frequency transfer between the components. Within this work, three generations of this breadboard were build: one for the Sr1 laser system, one for the Sr2 laser system presented in this work, and one for the transportable clock laser system (Al1) of an Aluminium (Al) ion quantum logic clock [115]. The first two systems use external-cavity diode lasers (ECDLs)[2] at 698 nm and at 1397 nm respectively. The Al1 laser system uses a distributed feedback (DFB) fiber laser[3] at 1069 nm. As the three laser systems are operated using different laser types and wavelengths, there are necessary slight differences in the design due to different size of the single components (e.g. optical isolators). First, the general concept of all three distribution breadboards is presented and then differences between the different generations are noted.

Figure 4.2 shows a general schematic sketch of the breadboards including the most relevant optical components. The grey area indicates which optical components are placed on the distribution breadboard itself. The breadboard has five ports to send light to the atoms, the reference cavity, a wavelength meter, and to a frequency comb or a second clock for comparison. In principle, every port can be used to send light to any component. However, as shown in figure 4.2, the ports are designed differently to better fulfill their intended function. Polarizing beam splitters (PBSs) are used to distribute the laser light to the five different ports.

Port 1 (green) sends light to the ultra-stable reference cavity. As cavities typically show a frequency drift in the order of $10\,\mathrm{mHz\,s^{-1}}$ to $100\,\mathrm{mHz\,s^{-1}}$, for example due to slow settling of the spacer, a drift correction between the cavity frequency and the clock laser frequency is needed. For this purpose, the light passes the cAOM twice on

[2]DL pro from TOPTICA Photonics
[3]Koheras ADJUSTIK from NKT Photonics

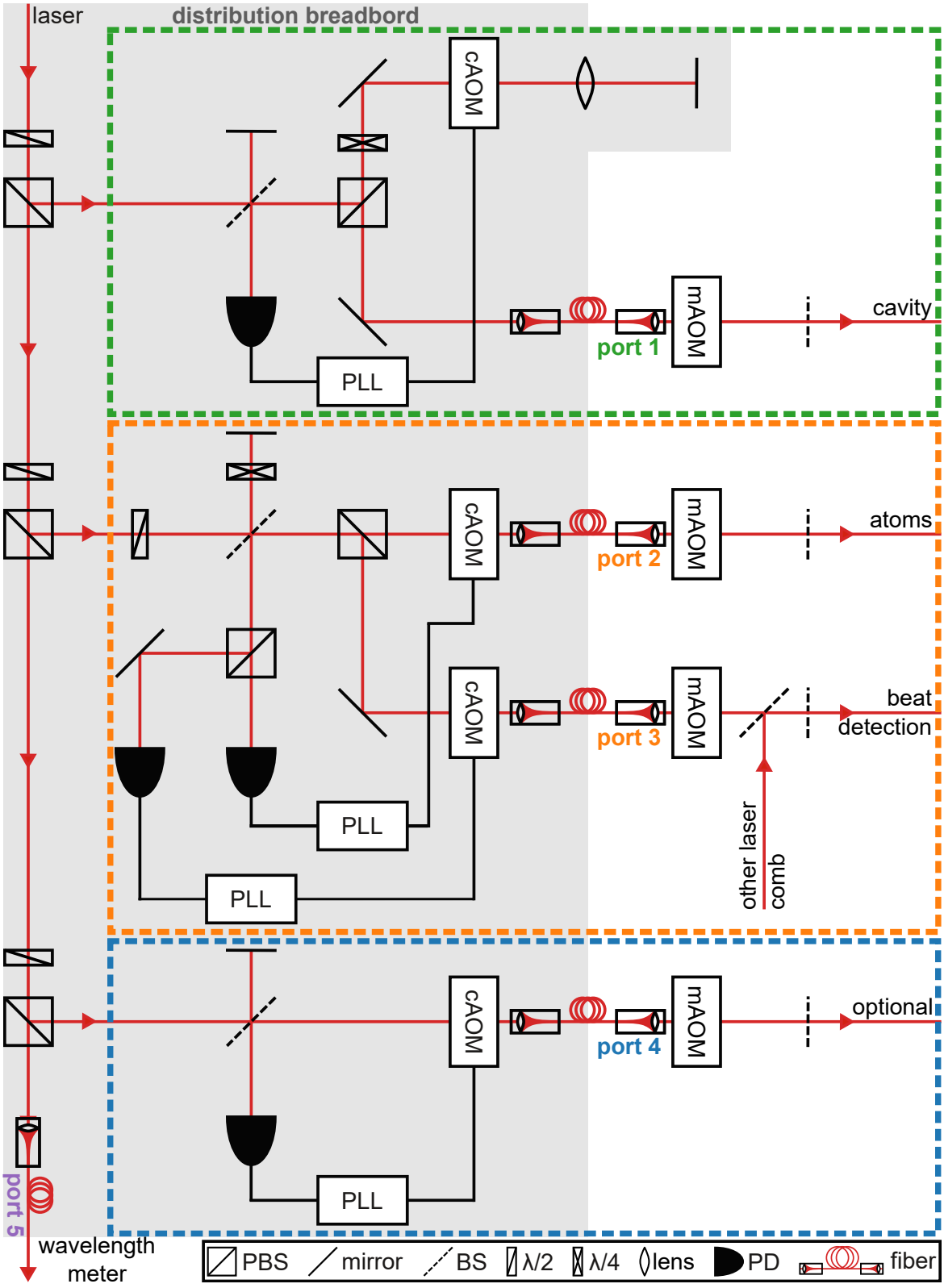


Figure 4.2.: Schematic sketch of the laser light distribution breadboard.

its way to and back from the cavity. A lens is placed in the middle between the double-pass cAOM and the mirror reflecting the light back whose focal matches exactly the distance to the mirror/double-pass acousto-optic modulator (AOM). This double-pass technique allows a change in the diffraction angle of the 1st order light of the AOM, without affecting the beam path elsewhere. This in turn allows a large change in radio frequency (RF) frequency at the double-pass AOM and therefore in its frequency shift. A more detailed description of this port including the optics on the cavity side is given in chapter 5.

Port 2 and 3 (orange) share the same reference mirror. Thus, there is no uncompensated path between the two ports. In contrast, there is an uncompensated path between the reference mirror of port 1 and the reference mirror of port 2/3. Here, a change in the geometrical length or refractive index between the two reference mirrors would add phase noise between the ports. An uncompensated path between the atom port and the cavity port could cause a degradation of the laser stability in the worst case. An uncompensated path between the atom port and the comparison port could cause a frequency shift between the clocks. Therefore uncompensated path between the ports, especially the atom and comparison port, should be avoided or if inevitable, kept as short as possible. The same applies for light traveling beyond the breadboard. Therefore, the first order of the marker acousto-optic modulator (mAOM) is used for both sending light back for the fiber noise cancellation and to overlap with the frequency comb. The light of the two compared systems should be superposed first, before placing the back reflection mirror.

Port 4 (blue) includes a simple fiber noise cancellation setup. It can be used for example as additional comparison port to compare against two other ultra-stable laser systems at the same time either directly or via a frequency comb. Another application is a two stage fiber noise cancellation to the cavity or the atoms as described in section 5.5.

Port 5 does not include any noise cancellation and can be used to monitor the rough clock laser frequency on a wavelength meter.

A detailed description of the optical setup around the cavity is given in chapter 5 and the setup close to the atoms in chapter 6.

The first generation breadboard (Sr1b) was built to replace the much larger and heavier distribution breadboard (Sr1a) of the Sr1 laser system. There is no fiber noise cancellation to the cavity provided from the optical setup at the cavity of the Sr1 laser system. Therefore, the Sr1b breadboard was designed to be placed direly above the ultra-stable cavity, see figure 4.3a, to keep the fiber between breadboard and cavity as short as possible. Before, the fiber between the old Sr1a distribution breadboard and the cavity caused a degradation in clock laser stability, as mentioned above. The breadboard also includes an atom port and a comparison port with a shared reference mirror as well as a wavelength meter port[4]. The ECDL is directly included in the distribution breadboard to achieve a more compact design. A sketch of the optical setup of the whole laser system including its distribution breadboard is given in Häfner et al. [51].

[4]The wavelength meter port is not included in the drawing in Häfner et al. [51]

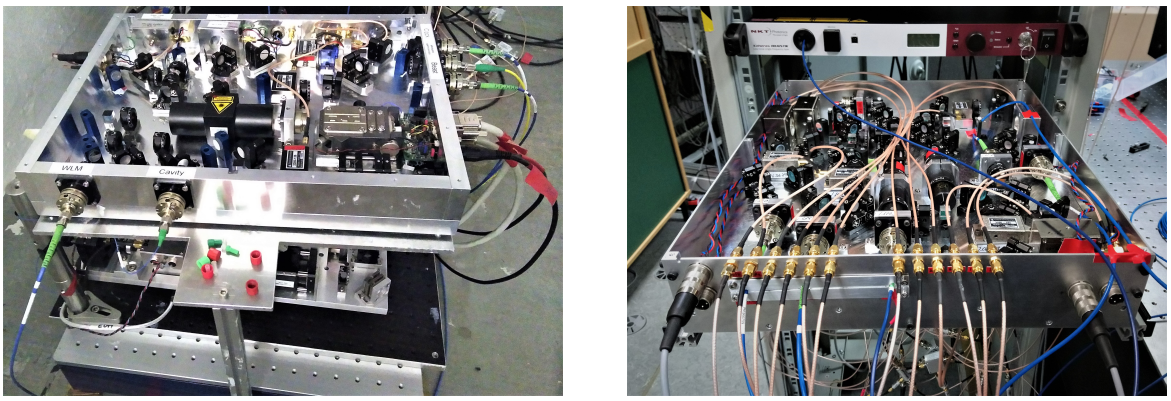

(a) (b)

Figure 4.3.: (a) Sr1b distribution breadboard (b) Al1 distribution breadboard

The second generation distribution breadboard (Sr2) is almost identical to the first generation, except that it includes a fiber noise cancellation for the fiber to the cavity and is operated at 1397 nm instead of 698 nm, which is twice the interrogation wavelength of a Strontium (Sr) lattice clock.

The third and last generation, the Al1 breadboard, is identical to the sketch in figure 4.2. As the Sr2 and Al1 breadboard include a fiber noise cancellation for the fiber to the cavity, there is no need to place them close to the cavity. Thus, they can be placed as a drawer inside a rack as shown in figure 4.3b. One difference of the Al1 bread board compared to the others is that the atom port needs approximately three orders of magnitude more power than the other ports. Normally, a few milliwatts are sufficient for each port. The Al1 laser system is operated at a quarter of the clock frequency to reach the spectrum where crystalline mirrors can be used to reduce the thermal noise of the cavity. Thus, the Al1 clock laser frequency needs to be frequency doubled twice with an expected low efficiency to reach the clock frequency, which is currently under investigation within another project. Therefore, the light reflected to the optional port is split off first and is used to send light to the atoms. The original atom port, port 2, can then be used for a multi-stage fiber noise cancellation, if needed. This way, the high light power needed for the atom port does not interfere with the other low-power ports.

The mechanical stability and mounting of the breadboard was also improved in the later generations, especially Al1. A detailed description of the last generation distribution breadboard and its improvements compared to the previous generations can be found in the Master thesis of Klocke [116] supervised within this work. The last generation breadboard has a footprint of $37\,\mathrm{cm} \cdot 43.5\,\mathrm{cm}$ and a decreased weight of less than 5 kg without optics at an increased mechanical stability compared to the previous generation [116]. The fractional frequency instability $\mathrm{mod}\,\sigma_\mathrm{y}$ and the maximal fractional frequency shift between the ports was determined by recording beat notes between the single ports with a frequency counter[5]. For averaging times smaller

[5] K+K FXE from K + K Messtechnik GmbH, using lamda averaging

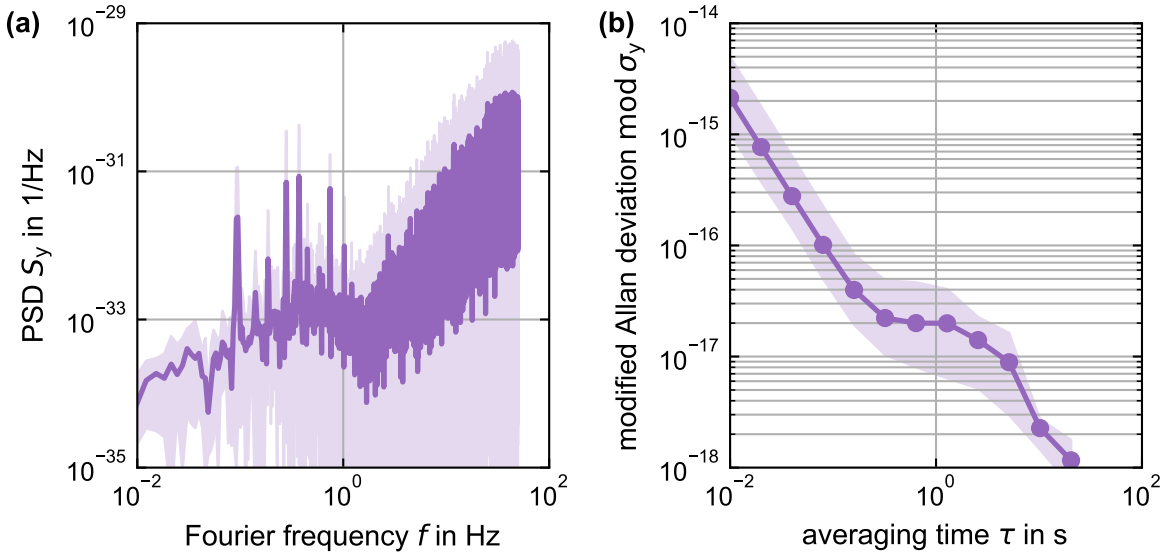


Figure 4.4.: Fractional frequency instability caused by light distribution and electronic noise. The solid lines represent the mean over the measurements between the three possible port pairs on the Sr2 breadboard and the shaded areas represent the scatter of the measurements.

than 0.1 s, noise caused by the electronic components of the beat note detection and recording has most likely a significant impact to the fractional frequency instability [116]. The fractional frequency instability mod $\sigma_y$ is well below $5 \cdot 10^{-17}$ for averaging times of $\tau \approx 1$ s and the maximal fractional frequency shift between the ports was determined to be smaller than $10^{-19}$ [116]. Neither the fractional frequency instability caused by the light distribution results in a significant increase of clock laser instability at around 1 s averaging time, at which the thermal noise floor is in the upper $10^{-17}$ range, nor the fractional frequency shift caused by the light distribution adds a significant contribution to the fractional uncertainty of today's optical clocks that is in the order of $10^{-18}$ [17–19, 22, 27, 28]. Thus, the clock operation is not degraded by be light distribution with such a distribution breadboard.

Figure 4.4 shows the fractional frequency instability of the Sr2 breadboard used for the laser system presented in this work. As a measurement between two ports with the same reference mirror does not show a significant lower instability compared to a measurement between two ports with different reference mirrors, it is assumed that rather the electronic noise puts a limit to the measured instability than the noise caused by uncompensated optical paths between the reference mirrors. Thus, the average over all measurements and their scatter is presented here. The fractional frequency instability mod $\sigma_y < 5 \cdot 10^{-17}$ for averaging times $\tau \approx 1$ s equivalent to the results found for the Al1 breadboard.

# 5. Transportable clock laser system

The laser system presented in this chapter is designed for a transportable Strontium (Sr) optical lattice clock [28]. The system is operated at 1397 nm or 214.6 THz, which is half the Sr clock transition frequency. Frequency doubling, as described in chapter 6, is applied to bridge the frequency difference between clock laser system and the clock transition frequency. This additional effort is taken to profit from the lower thermal noise contribution of crystalline mirrors, see section 3.2.1. The system uses an external-cavity diode laser (ECDL)[1], which is stabilized with the Pound-Drever-Hall (PDH) method to a 201.2 mm-long cavity consisting of an ultra low expansion (ULE) glass spacer, crystalline aluminium gallium arsenide ($Al_{0.92}Ga_{0.08}As$)/gallium arsenide (GaAs) mirrors [46] on fused silica (FS) mirror substrates and ULE glass compensation rings as shown in figure 5.1.

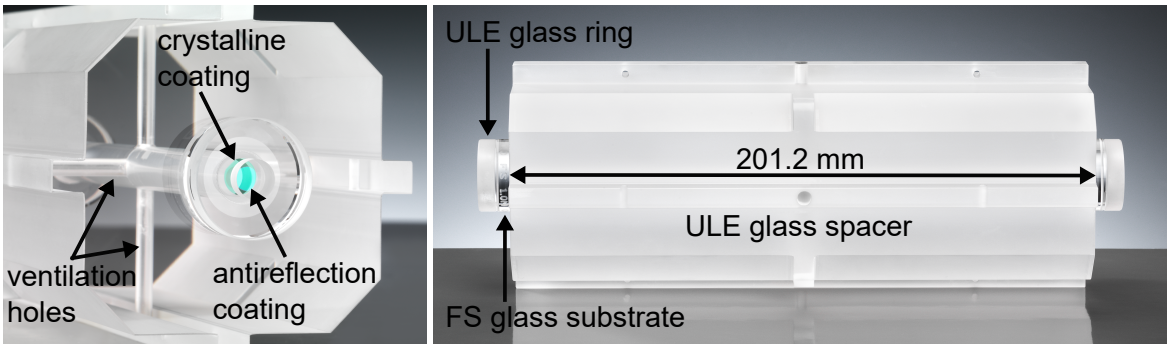


Figure 5.1.: Picture of the 201.2 mm-long ultra-stable cavity based on an ULE glass spacer, crystalline $Al_{0.92}Ga_{0.08}As$/GaAs mirrors [46] on FS mirror substrates and ULE glass compensation rings.

## 5.1. Finesse and cavity linewidth

The finesse $\mathcal{F}$ of the cavity's transverse electromagnetic (TEM) modes was determined using the ring-down method. Therefore, the laser light sent to the cavity was rapidly switched off using an acousto-optic modulator (AOM) and the laser light intensity transmitted through the cavity was detected with a photodiode (PD). An exponential decay $e^{-t/t_{\text{decay}}}$ of the laser light intensity is observed, whose decay time $t_{\text{decay}}$ defines the finesse $\mathcal{F}$ of the measured TEM mode in a Fabry-Pérot cavity.

$$\mathcal{F} = 2\pi\, FSR\, t_{\text{decay}} \tag{5.1}$$

[1] DL pro from TOPTICA Photonics

Table 5.1.: Finesse of the 20 cm cavity with different mirror combinations.

| | test setup | | | final setup |
|---|---|---|---|---|
| | M1 and M2 | M1 and M3 | M2 and M3 | M2 and M3 |
| $TEM_{00}$ mode | $< 100 \cdot 10^3$ | $< 100 \cdot 10^3$ | $\approx 300 \cdot 10^3$ | $136(9) \cdot 10^3$ |
| $TEM_{10}$ mode | $\approx 105 \cdot 10^3$ | $\approx 175 \cdot 10^3$ | $\approx 300 \cdot 10^3$ | $294(8) \cdot 10^3$ |
| $TEM_{01}$ mode | - | - | - | $\approx 70 \cdot 10^3$ |

The free spectral range (FSR) of this cavity is 745 MHz[2]. The ring-down measurements are performed under vacuum, due to the high absorption coefficient of water vapor at 1397 nm.

Three crystalline mirrors were available and are referred to as M1, M2 and M3[3]. In a test setup, the three combinations of these mirrors were optically contacted to the 20 cm spacer and their finesse was measured as shown in table 3.1. The third combination (M2 and M3) shows a much higher finesse of about $300 \cdot 10^3$ for the $TEM_{00}$ and the $TEM_{10}$ mode compared to the other two combinations. Thus mirror M1 shows a lower reflectivity than than M2 and M3, which were used for the final setup.

Figure 5.2 shows two exemplary measurements of the ring down for the $TEM_{00}$ (a) and $TEM_{10}$ (b) mode, after the cavity was put into its final setup and evacuated. The decay time of the $TEM_{00}$ mode averaged over several ringdown measurements is 29(2) µs, which corresponds to a finesse of $136(9) \cdot 10^3$. For the $TEM_{10}$ mode a decay time of 63(2) µs was determined, which results in a finesse of $294(8) \cdot 10^3$. The $TEM_{01}$

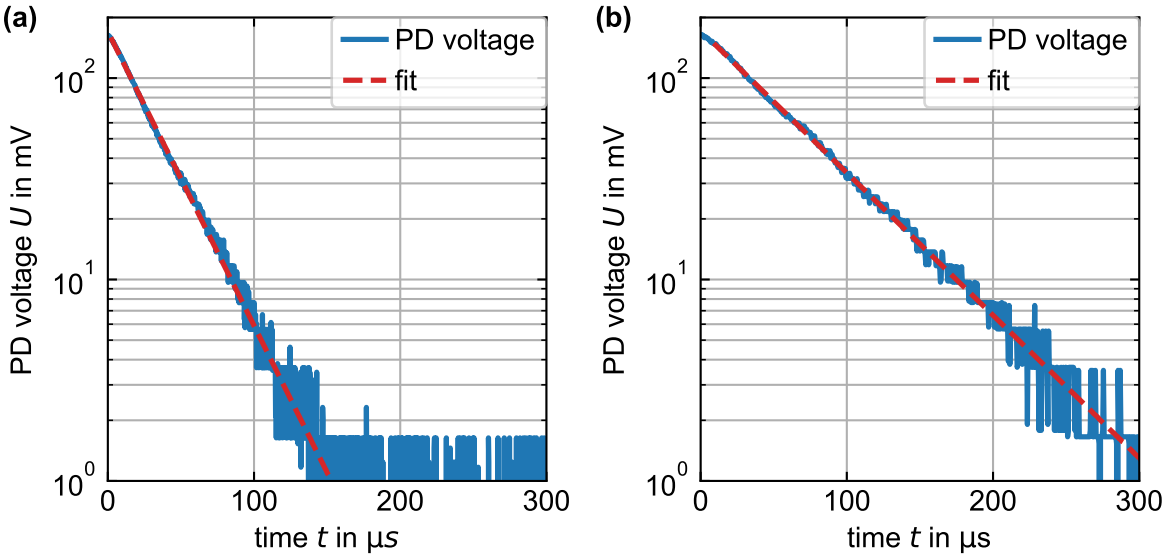


Figure 5.2.: Ring-down measurement of the cavity's $TEM_{00}$ (a) and $TEM_{10}$ (b) mode.

[2] $FSR = c/[2l_0]$

[3] Produced by Crystalline Mirror Solutions

mode shows a finesse about $70 \cdot 10^3$, which indicates that during assembling likely a dust particle or similar fell on one or both of the mirrors, reducing the finesse of the $TEM_{01}$ and $TEM_{00}$ modes compared to the $TEM_{10}$ mode. As the linewidth of a cavity reduces with higher finesse and thus the steepness of the PDH error signal increases with higher finesse, see equation 3.1, it is advantageous to operate the cavity at the $TEM_{10}$ mode to get a factor of two more sensitive error signal and lower sensitivity to residual amplitude modulation (RAM). Thus, the cavity is operated at its $TEM_{10}$ mode to profit from its higher finesse, which results in a cavity linewidth of 2.53(4) kHz.

## 5.2. Mode spacing

The fractional frequency instability of a laser stabilized to an ultra stable reference cavity can be degraded if another TEM mode has only a small frequency difference to the TEM mode used for stabilization as it would be excited and affect the PDH error signal. Therefore, the cavity length is optimized within a range of $200\,\text{mm} \pm 5\,\text{mm}$ with the goal that the first higher order mode found within $\pm 10\,\text{MHz}$ of the $TEM_{00}$ and $TEM_{10}$ modes has an as high order as possible to reduce the impact of higher order modes. At a length of 201.2 mm, a longitudinal mode spacing[4] of 745 MHz corresponding to the FSR and a transverse mode spacing[4] of 153 MHz was found. The first higher order mode within $\pm 10\,\text{MHz}$ is 39 orders above.

## 5.3. Birefringence

Crystalline mirrors, as used in this cavity, show a birefringent behavior [46], which results in a splitting of the cavity modes as the light experiences different cavity lengths depending on its polarization. The difference in cavity length $\Delta l_{\Delta\text{n}}$ experienced by linear polarized light aligned with the slow axes compared to light aligned with the fast axes of the mirrors differs by twice the penetration depth $l_{\text{pen}}$ times the birefringence $\Delta n$, $\Delta l_{\Delta\text{n}} = 2 \cdot l_{\text{pen}} \cdot \Delta n$. The penetration depth $l_{\text{pen}}$ can be expressed according to equation 5.2 via the reflection delay $t_{\text{delay}}$ and the average refractive index of the coating $n_{\text{ct}}$ as given in equation A.21 [118].

$$l_{\text{pen}} = \frac{c\, t_{\text{delay}}}{2\, n_{\text{ct}}} \tag{5.2}$$

The reflection delay is given by equation 5.3, which assumes an infinite number of mirror layers [118]. As the penetration depth is much smaller than the coating thickness, this approximation is decent and only results in a relative error of approximately 0.01 %.

$$t_{\text{delay}} = \frac{1}{2\,\nu_0} \left( \frac{n_{\text{I}}}{n_{\text{H}}} \right) \frac{n_{\text{H}}}{n_{\text{H}} - n_{\text{L}}} \tag{5.3}$$

[4] $\Delta\nu_{mnq} = FSR\left[q + \frac{m+n+1}{\pi} \arccos(\sqrt{g_1 g_2})\right]$ with $TEM_{mn}$, q describing the longitudinal mode order and $g_1$ as well as $g_2$ being the stability parameter of a Fabry-Pérot cavity as given in equation A.25 and A.26, see for example Siegman [117].

Here, $n_\mathrm{I}$ is the reflective index of the incident material, which is $n_\mathrm{I} = 1$ for vacuum. Additionally, the first layer is assumed to be a high reflective index layer.

The splitting $\Delta\nu_{\Delta\mathrm{n}}$ depends on the orientation of the mirrors' polarization axes to each other, described by the angle $\theta_{\Delta\mathrm{n}}$. For a parallel orientation of the mirror axes, $\theta_{\Delta\mathrm{n}} = 0$, the splitting is maximal, while for perpendicular orientation, $\theta_{\Delta\mathrm{n}} = \pi/2$, the splitting is zero. Thus, the splitting is given by the equation 5.4.

$$\Delta\nu_{\Delta\mathrm{n}} = \nu_0 \frac{2\, l_\mathrm{pen}\, \Delta n \cos(\theta_{\Delta\mathrm{n}})}{l_0} \tag{5.4}$$

The crystallographic orientation and thus the polarization axes of the mirror are indicated by a flat, as know from silicon wafers in the semiconductor industry. For this cavity, the mirrors' flats are oriented parallel to each other in order to achieve a maximum splitting between the two modes.

The splitting $\Delta\nu_{\Delta\mathrm{n}}$ was determined by locking the laser to the two $\mathrm{TEM}_{10}$ modes and measuring the laser frequency by comparing it to a second ultra-stable laser system based on a silicon resonator [44] via a frequency comb. The splitting $\Delta\nu_{\Delta\mathrm{n}}$ for this cavity is about 16 kHz, which results in a birefringence $\Delta n = 3{\cdot}10^{-5}$ using equations 5.2 to 5.4 and the values in table B.1.

This birefringence is small compared to previously published values, which are around $10^{-3}$ [46, 119]. Also, the birefringence of a second clock laser system build in this work for an $Al^+$ clock, which is identical to this system, but operated at 1070 nm, was measured. The splitting $\Delta\nu_{\Delta\mathrm{n}} = 345\,\mathrm{kHz}$, resulting in a birefringence of $\Delta n = 7.6 \cdot 10^{-4}$. After discussion with the supplier of the crystalline mirrors, the most likely explanation for the unexpected low birefringence is that the mirror flats accidentally were not aligned to the same crystallographic axis during production. Thus, the angle is $\theta_{\Delta\mathrm{n}} \neq 0$ and the splitting is not maximal.

However, in practice one mode of the two modes caused by birefringence can be sufficiently suppressed by using linearly polarized light aligned either with the fast or with the slow axis of the cavity. To obtain the desired linearly polarized light, a Faraday rotator is placed in front of the cavity instead of the typical quarter waveplate within the setup of the PDH locking.

## 5.4. Thermal noise limit

For this cavity, the thermal noise floor was calculated using the equations in section 3.2. The values and dimension given in figure C.1, table B.1 and 5.2 are used for the finite element method (FEM) simulation and calculation of the thermal noise.

For the Brownian noise contributions, the elastic strain energy $W_0$ of the spacer, mirror substrates and compensation rings was calculated using the FEM to take the excess noise [96] and the complex design of the spacer into consideration, see section 3.2.1 around equation 3.11 or Kessler et al. [96]. As the system is operated at the $\mathrm{TEM}_{10}$ mode, instead of equation 3.10 the following equation taking the $\mathrm{TEM}_{10}$ beam

Table 5.2.: Values for thermal noise calculation.

| substrate[a] | value | coating[b] | value | rings[d] | value | other | value |
|---|---|---|---|---|---|---|---|
| $\varnothing_{(\mathrm{sb})}$ | 25.4 mm | $N_\mathrm{L}$ | 38 | $\varnothing_{\mathrm{out}}^{(\mathrm{cr})}$ | 25.4 mm | $w$[e] | 385 µm |
| $d_\mathrm{sb}$ | 6.35 mm | $N_\mathrm{H}$ | 39 | $\varnothing_{\mathrm{in}}^{(\mathrm{cr})}$ | 8 mm | $\lambda_0$ | 1397 nm |
| ROC | 1 m | $d_\mathrm{ct}$[c] | 8.5 µm | $d_\mathrm{cr}$ | 6 mm | $T$ | 297 K |
| annulus | 6.9 mm | - | - | - | - | - | - |

[a] Cylindrical substrate with diameter $\varnothing_{(\mathrm{sb})}$ and height $d_\mathrm{sb}$.
[b] The coating is made of quarter-wave layers starting and ending with a high-reflective-index layer.
[c] Calculated from equation A.22
[d] The compensation rings have hollow cylindrical shape with an outer diameter $\varnothing_{\mathrm{out}}^{(\mathrm{cr})}$, inner diameter $\varnothing_{\mathrm{in}}^{(\mathrm{cr})}$ and height $d_\mathrm{cr}$ calculated from equation A.22.
[e] Calculated from equations A.23 and A.24

profile into account is used. A different mode profile leads to a different maximum elastic strain $W_0$ at the same test force $F_0$.

$$p_0(r)(x,y) = \frac{2F_0}{\pi w^2}\frac{4y}{w^2}e^{-\frac{2(x^2+y^2)}{w^2}} \tag{5.5}$$

However, the difference compared to a FEM calculation using the $\mathrm{TEM}_{00}$ mode beam profile is less than 10 %. Thus, for estimating the noise of the thermo-optic (TO) contributions, the equations based on the $\mathrm{TEM}_{00}$ beam profile are used for simplicity.

Figure 5.3 shows the five biggest contributions to the thermal noise floor. The contributions of the compensation ring as well as the thermoelastic (TE) noise of the spacer and the thermorefractive (TR) noise of the substrate are significantly lower than the five main contributions. Thus, they are neglected here. As expected, the Brownian noise contribution of the spacer increases compared to figure 3.5 c mainly due to the excess noise in the spacer at the mirror substrate edges [96], which is not considered in the equations. Thus spacer, mirror coating and substrate contribute equally to the overall thermal noise.

All thermal noise curves depend on various material properties, which have partly been measured only with considerable uncertainty or even only derived from other materials, see table B.1. Thus, single curves may easily have an uncertainty of a few ten percent. To provide a conservative estimate, preferably values that result in a higher noise floor were chosen in the case of unclear values.

For this cavity, the Brownian noise contribution of the mirror substrate and the spacer are over a wide frequency range the biggest contribution. The TE noise of the mirror substrate contributes significantly for Fourier frequencies around 1 Hz and the TO noise of the mirror coating dominates for Fourier frequencies above 10 Hz.

Due to a lower mechanical loss factor and higher thermal conductivity of silicon compared to FS glass, silicon mirror substrates would reduce the thermal noise floor

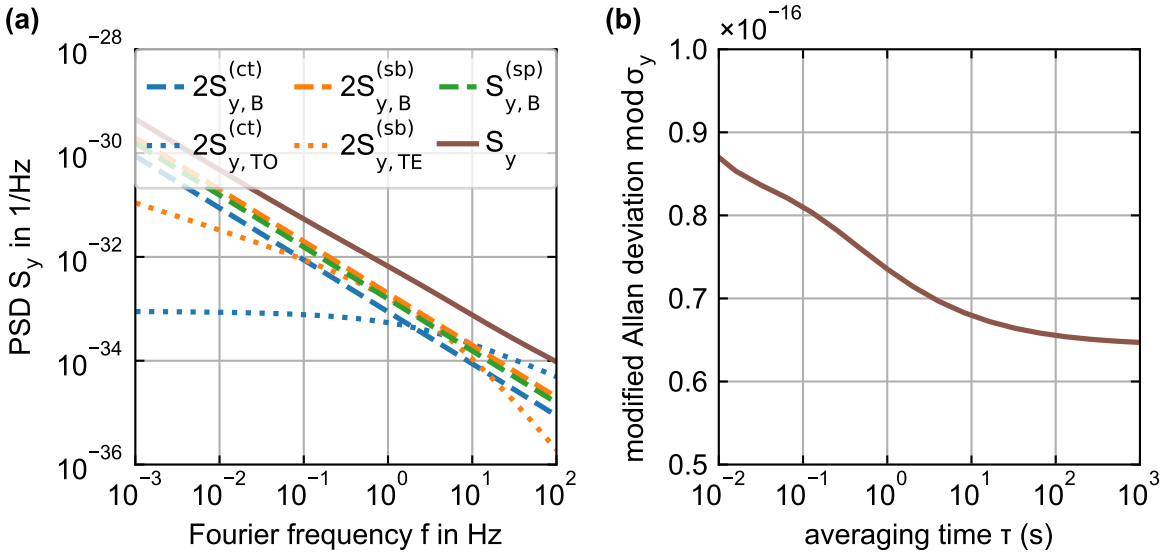


Figure 5.3.: Major thermal noise contributions for the presented cavity, see text.

to approximately $\mathrm{mod}\,\sigma_y = 4.4 \cdot 10^{-17}$ as they reduce the substrates' and mirrors' Brownian and TO noise contributions[5]. The Brownian noise contribution of the ULE glass spacer remains unaffected and adds the biggest contribution to the overall thermal noise floor in case of silicon mirror substrates. Despite the lower mechanical loss factor and higher thermal conductivity, silicon has a four times higher cofficient of thermal expansion (CTE) compared to FS glass. A higher CTE of the mirror substrate increases the temperature sensitivity of the cavity as described in section 5.9.

## 5.5. Residual amplitude modulation

Especially for a transportable system, a passive reduction of the RAM is the most convenient solution, as it requires no additional electronics and less optical components compared to an active stabilization of the RAM. A commercial available free-space electro-optic modulator (EOM)[6] with a flat input surface and an wedged output surface to separate the extraordinary and ordinary light beam and an active temperature stabilization was tested to determine if the passive reduction of the RAM is sufficient and an active stabilization of the RAM can be avoided.

All optical components needed for the PDH stabilization were placed on a breadboard, which was screwed to the vacuum chamber of the cavity as shown in section 5.9, figure 5.16. A partly reflecting mirror was placed before the EOM, which serves as a reference surface for the phase noise cancellation between distribution and PDH

[5]The equations from section 3.2 and the values from table 5.2 and B.1 are used for the calculation. For the spacer contribution the curve in figure 5.3 is used to take the excess noise of the spacer as described by Kessler et al. [96] into account.

[6]PM7-SWIR from QUBIG.

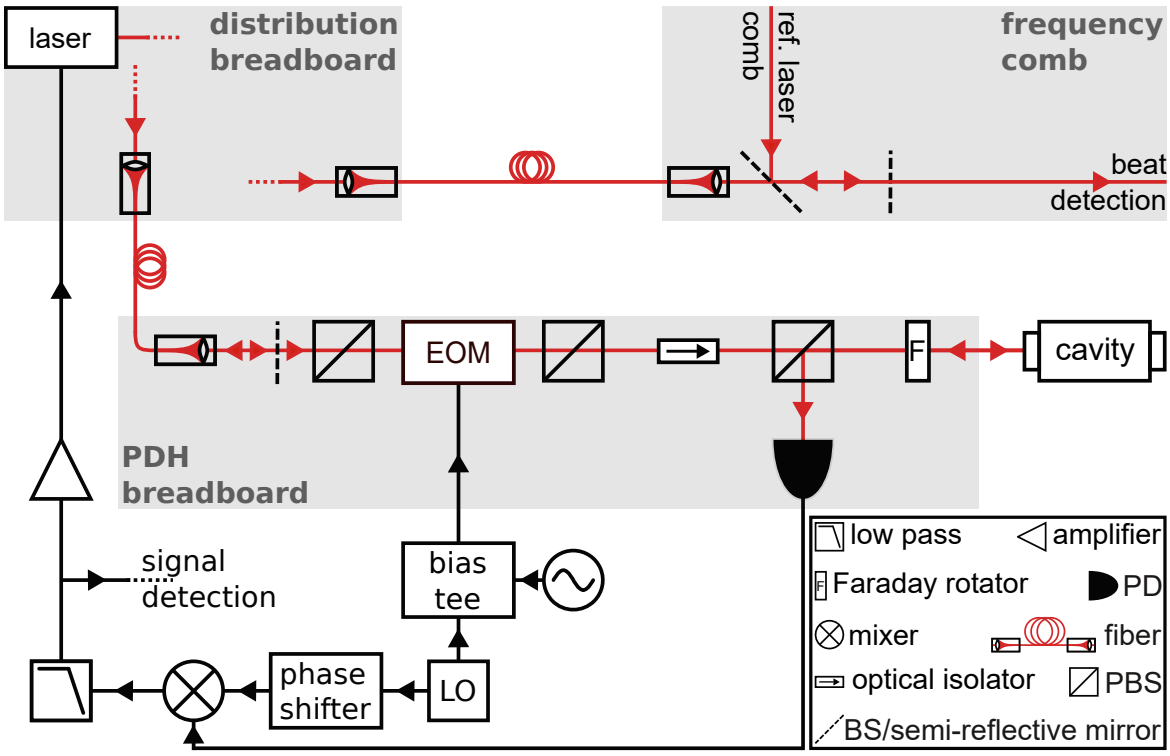


Figure 5.4.: Laser system setup using a passive RAM reduction with an free-space EOM

breadboard as shown in figure 5.4.

To determine the fractional frequency instability caused by RAM around 1 Hz, an oscillation of 1 Hz was added via the bias tee to the EOM input signal. The laser's frequency was locked to the cavity's resonance and compared via a frequency comb to an ultra-stable reference system [44]. The resulting laser frequency oscillation at 1 Hz was measured. Then the laser was unlocked from the cavity resonance and its frequency was shifted a few 10 MHz away from a cavity resonance. The amplitude of the voltage oscillation of the demodulated PDH signal at 1 Hz was measured. The resulting volt to frequency conversion factor for this setup is $48(5)\,\mathrm{V\,Hz^{-1}}$. The 1 Hz oscillation at the bias tee was switched off and the demodulated PDH signal was measured with a fast Fourier transform (FFT) analyzer[7]. The measured voltage oscillations were converted into frequency fluctuations using the previously determined conversion factor. Figure 5.5 shows the power spectral density (PSD) and the modified Allan deviation (mADEV) of the expected fractional frequency fluctuation caused by the RAM. The shaded areas indicate the measurement uncertainty including the statistical uncertainty of the measurement and the uncertainty of the conversion factor. The instability caused by RAM is in the higher $10^{16}$ region at one second.

For the same type of free-space EOM operated at 578 nm, Jin [83] reported a fractional frequency instability of approximately $8 \cdot 10^{-16}$ at 1 s. Jin [83]'s cavity has a

[7] CF-9400 FFT analyzer form the company Onosokki

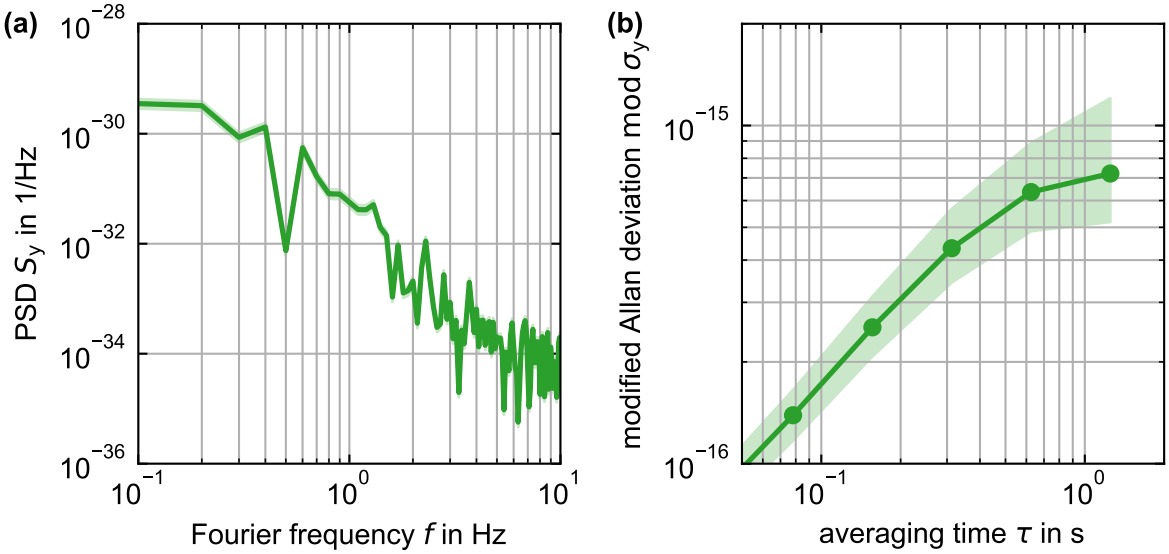


Figure 5.5.: Fractional frequency instability caused by RAM using an commercial free-space EOM.

linewidth 1.3 times higher than the linewidth of this cavity, making their system presumably more sensitive to RAM. Based on the available knowledge of the two systems, the RAM produced by such an EOM agrees within the measurement uncertainty.

To operate the laser system at its thermal noise floor, the intrinsic RAM needs to be reduced by more than an order of magnitude. Therefore an active control was implemented in the setup as introduced in section 3.1.2. Unfortunately, the required suppression was not achieved by the active control, most likely due to a non-uniform spatial distribution of the RAM over the beam cross section.

Other promising free-space EOM designs that offer a low enough RAM to reach the thermal noise floor of this system have been reported for wedged ammonium dihydrogen phosphate (ADP) crystals [83] and Brewster-cut lithium niobate ($LiNbO_3$) crystals build for previous laser systems at Physikalisch-Technische Bundesanstalt (PTB) [43, 51]. ADP crystals show a transmission of less than 20 % at 1397 nm [120] and are thus not suitable for this system. The $LiNbO_3$ based EOM has decent optical properties at 1397 nm and causes fractional frequency instabilities $\sigma_y = 1 \cdot 10^{-17}$ for a cavity linewidth of 1.1 kHz [121, 43] and mod $\sigma_y = 5 \cdot 10^{-17}$ [121, 51] for a cavity linewidth of 2.7 kHz at 1 s averaging time operated at 698 nm. Thus, the expected instability for this system should be in the mid $10^{-17}$ range, meaning this EOM could meet the requirements. Such an EOM was removed from the current transportable clock laser system [51] and tested with this system while writing this work. An upper boundary of the instability caused by RAM was determined to be in the mid $10^{-17}$ range. No significant reduction of the laser performance, as demonstrated in section 5.10, was found. Thus, if such an EOM is available, the system can be operated without active RAM stabilization. However, while performing the measurements here in after, all home-made $LiNbO_3$ EOMs were required for operation of the current clock laser sys-

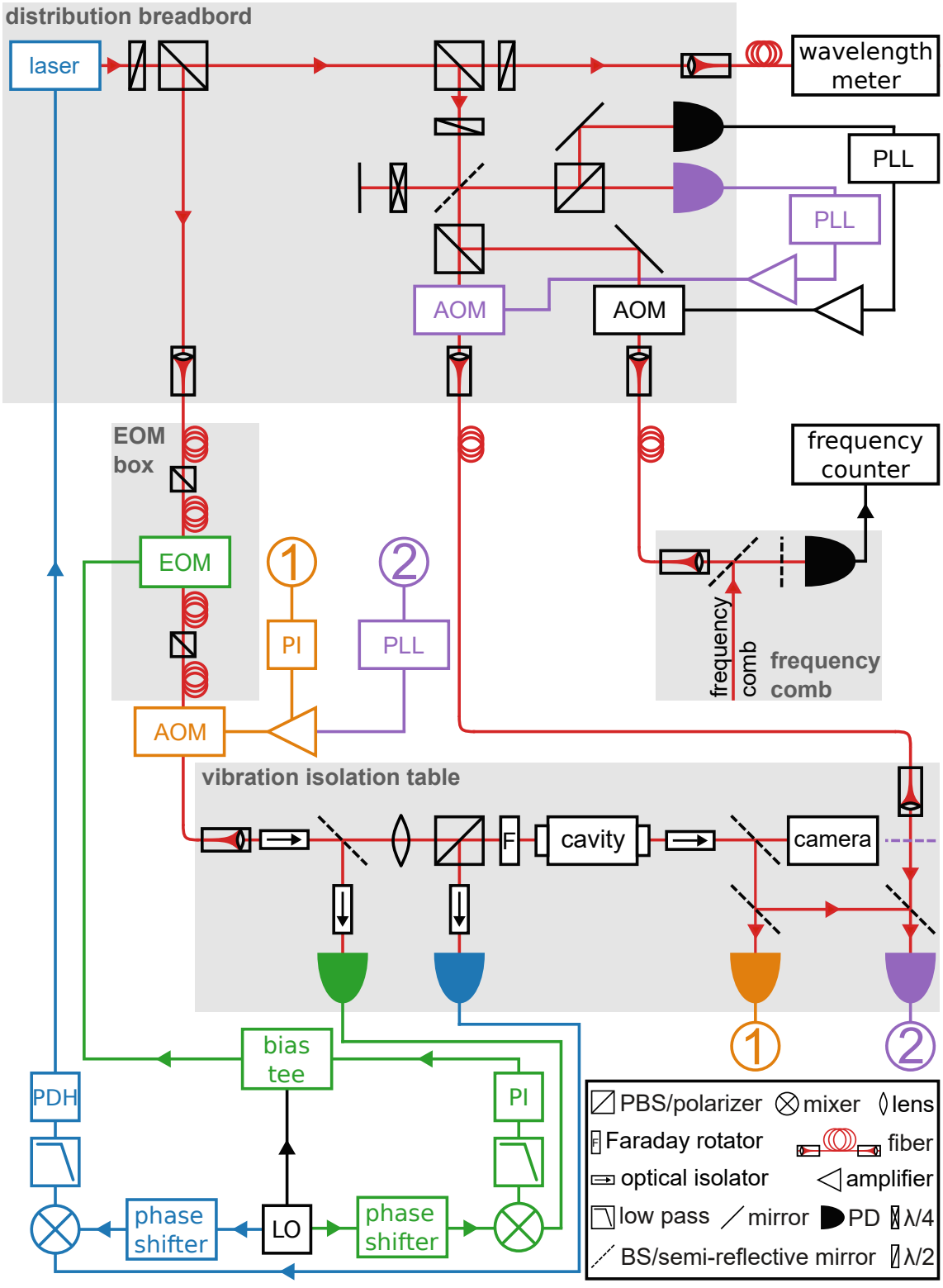


Figure 5.6.: Schematic sketch of the laser system, as used for the characterization: blue: PDH stabilization, green: active RAM control, orange: power stabilization and purple: two-stage phase noise cancellation.

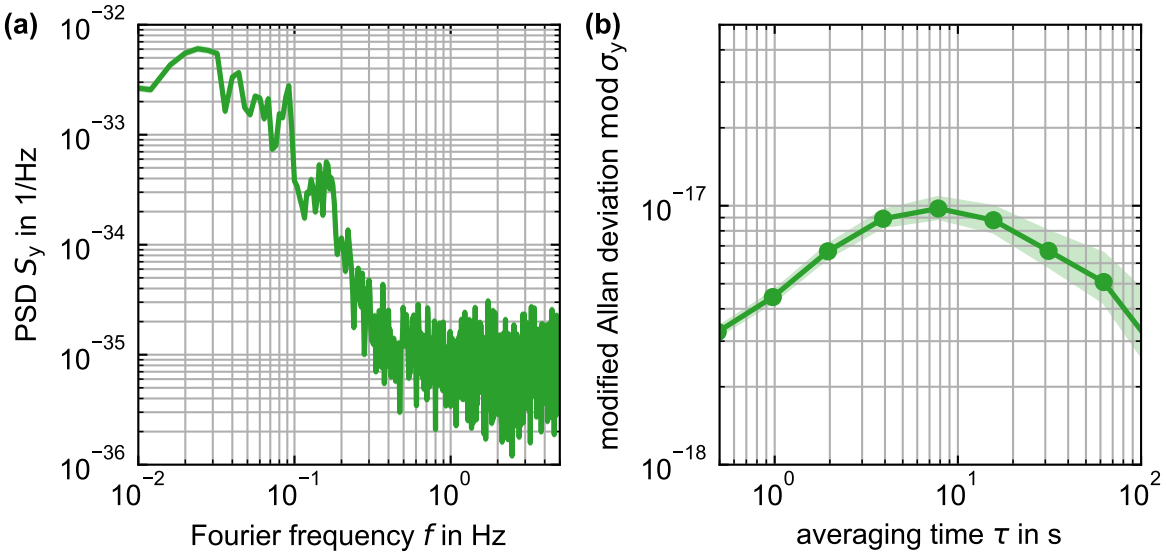


Figure 5.7.: Fractional frequency instability caused by RAM using a temperature stabilized waveguide EOM together with an active RAM control.

tems and thus a waveguide EOM[8] together with an active stabilization of the RAM was used, see green components in figure 5.6. To reduce the intrinsic RAM fluctuations caused by refractive index changes of the EOM and the fibers between the polarizers, the waveguide EOM was screwed to a temperature stabilized copper block and placed together with the two in-line polarizers inside an Aluminium (Al) box. Additionally, a two-stage optical path length stabilization, see purple components in figure 5.6, was implemented as the simple path length stabilization as shown in figure 5.4 caused an étalon in combination with the back reflection mirror, which potentially causes RAM fluctuations.

The remaining instability caused by RAM was evaluated in the same way as for the free-space EOM and is below $2 \cdot 10^{-17}$, see figure 5.7. The measurement of the instability is limited by electronic noise for frequencies above 0.5 Hz.

Even though a lower instability is reached compared to the homemade free-space EOM, the simpler setup in figure 5.4 is clearly advantageous for a transportable system as it is still below its thermal noise floor.

## 5.6. Photothermal noise

As a fraction of the optical power oscillating in the cavity is absorbed by the mirror coatings, a fluctuation in optical power results in a temperature fluctuation of the cavity. These temperature fluctuations cause refractive index variations and thermal expansion of the cavity components, which in turn result in an optical length change of the cavity, equivalent to TO noise, as described in section 3.2. This optical

[8] phase modulator from EOSPACE

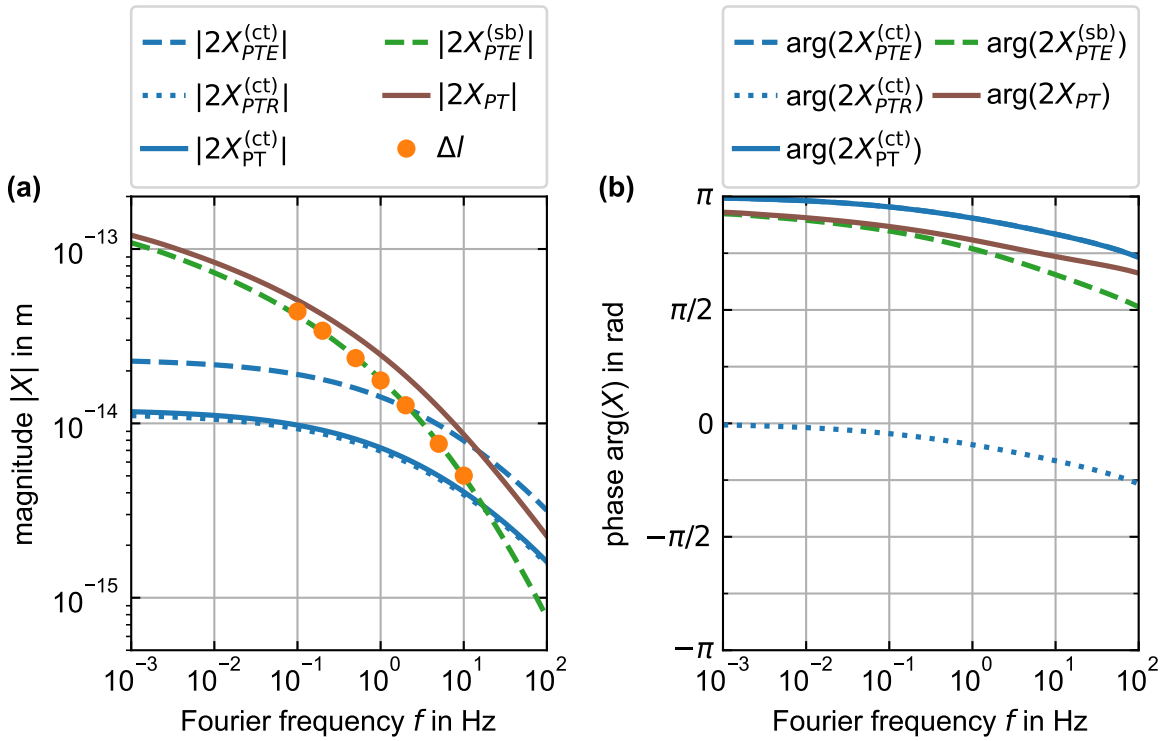


Figure 5.8.: Photothermal noise of the different contributors as a function of frequency. The lines show calculated curves and the dots measured data.

power-induced instability is called photothermal (PT) noise. Its fundamental limit in case of constant optical power is produced by the shot noise of the absorbed radiation [99, 106]. The photothermorefractive (PTR) noise of the mirror coatings and the photothermoelastic (PTE) noise of the substrates and coatings are the biggest contributions to the overall PT noise of this cavity. Theoretical models and a detailed description of the photothermal noise are given amongst others in Farsi et al. [122], Gorodetsky [88], De Rosa et al. [123] and Cerdonio et al. [106].

The power absorbed by the cavity mirrors $\delta P_{\mathrm{abs}}$ is for low Fourier frequencies equal to the intracavity power $\delta P_{\mathrm{cav}}$ times the mirrors absorption coefficient $\chi_{\mathrm{abs}}$ and shows a low pass behavior at higher Fourier frequencies with a cut off frequency $f_{\mathrm{T}}^{(\mathrm{cav})} = lw/2$.

$$\delta P_{\mathrm{abs}} = \frac{\delta P_{\mathrm{cav}} \chi_{\mathrm{abs}}}{1 + if/f_{\mathrm{T}}^{(\mathrm{cav})}} \tag{5.6}$$

The equations for the transfer function $\delta X_{\mathrm{PT}}$ between the absorbed power $\delta P_{\mathrm{abs}}$ and resulting optical cavity length fluctuations $\delta l$ including the PTE noise of the substrate $\delta X_{\mathrm{PTE}}^{(\mathrm{sb})}$, PTE noise of the coating $\delta X_{\mathrm{PTE}}^{(\mathrm{ct})}$ and PTR noise of the coating $\delta X_{\mathrm{PTR}}^{(\mathrm{ct})}$ are given in appendix A.5. The calculated magnitude $|\delta X_{\mathrm{PT}}|$ and phase $\arg(\delta X_{\mathrm{PT}})$ of the resulting optical cavity length fluctuations are shown in figure 5.8 for $\delta P_{\mathrm{cav}} \cdot \chi_{\mathrm{abs}} = 0.25\,\mu\mathrm{W}$. As $|\delta X_{\mathrm{PTE}}^{(\mathrm{ct})}|$, blue dashed line, and $|\delta X_{\mathrm{PTR}}^{(\mathrm{ct})}|$, blue dotted line, are different in phase by $\pi$, the two contributions partly cancel and result in a total coating contribu-

tion $|\delta X_{\mathrm{PT}}^{(\mathrm{ct})}|$, blue solid line. The transfer function of the total PT noise of all three contributions is depicted by the brown curve.

At the frequencies of interest, a sine wave optical power modulation is applied to the cavity and the response of the laser frequency is measured. For this measurement, the setup in figure 5.6 with some small changes is used. The radio frequency (RF) power driving the orange AOM is modulated with a sine wave, thus modulating the optical power going to the cavity. The orange PD measures the laser power transmitted through the cavity, which is correlated to the power oscillating inside the cavity. The laser frequency is compared against a second ultra-stable laser [44] via an optical frequency comb. The resulting cavity length change of these measurements is plotted in figure 5.8, orange dots. The progression of the cavity length change, orange dots, seems to follow the curve for the PTE noise of the substrates, green curve, and not, as expected, the brown curve, which represents the expected total PT noise including the coating contributions.

An equivalent behavior for $Al_{0.92}Ga_{0.08}As/GaAs$ coatings on FS glass substrates is observed by Chalermsongsak et al. [111], but for a coating layer structure optimized to achieve PTR and PTE noise cancellation of the coating. Thus, only the PTE noise contribution of the substrate should remain. For better comparability, the same values of the material properties are used in this work. As the coating in this work consists simply of quarter-wavelength (QWL) layers, the PTR and PTE noise cancellation should be less compared to the structure in Chalermsongsak et al. [111]. Still, the measurement indicates that the gap between PT noise of the coating and PTE noise of the substrate might be bigger than expected for a QWL layer structure. For the coating, this would mean higher PTR noise, lower PTE noise or both as this results in better cancellation and a lower PT noise coating contribution. As mentioned above, the thermal noise curves depend on various material properties, which are only known with considerable error, see table B.1. Thus, the calculated values of PTR and PTE noise contribution might differ by a few 10 % from the true values, due the limited knowledge of the material properties. For example, 35 % higher PTR noise and 35 % lower PTE noise of the coating would justify the observed behavior. For the following estimations, the PT noise of the cavity is assumed to follow the behavior of the substrate PTE noise for frequencies smaller 10 Hz, which represents the measurements well.

The instability caused by PT noise is studied for approximately 10 µW of optical power coupled into the cavity. The transmission PD, orange in figure 5.6, detects optical power fluctuations of the laser light exiting the cavity. These power fluctuations are proportional to the intra-cavity power fluctuations and thus the power absorbed by the mirrors for Fourier frequencies $f \ll f_{\mathrm{T}}^{(\mathrm{cav})}$, which are the frequencies investigated. By fitting the expected curve for the PT noise to the measured length fluctuations of the cavity, a conversion factor of $0.25(2)\,\mu\mathrm{W}/560(3)\,\mathrm{mV}$ between the PD voltage and the absorbed power $\delta P_{\mathrm{abs}}$ is determined for this setup. The PT noise results in an instability in the order of $10^{-16}$ at one second that increases for higher averaging times, which puts a limitation to the laser system's instability. To reduce the PT noise

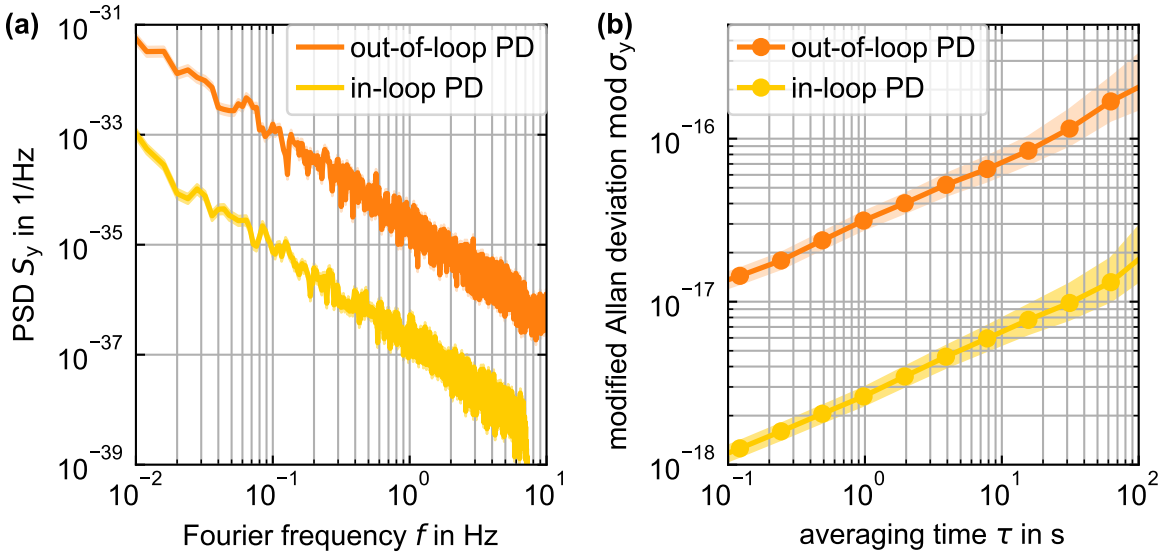


Figure 5.9.: Upper limit, orange, and lower limit, yellow, for the fractional frequency instability caused by optical power fluctuations of the interactivity light.

contribution, either an active stabilization of the optical power coupled into the cavity could be implemented or the absolute optical power coupled in to the cavity has to be reduced assuming that this also lowers the absolute power fluctuations by the same factor. For this system, the absolute power coupled into the cavity has to be reduced below 1 µW, which would result in a limitation caused by electrical noise of the PD detectors. Thus, a power stabilization is implemented as shown in figure 5.6 by the orange components.

The direct current (DC) signal of the PD detecting the transmitted optical power of the cavity is processed in a proportional-integral (PI) controller. The controller output changes the output power of an RF amplifier, which drives an AOM. This way, the optical power of the light in the AOM's first diffraction order is manipulated and thus stabilized at the transmission PD. The corner frequency of the controller was set close to the cavity linewidth. One limitation in this power stabilization is stray light or light from other sources, which is detected by the in-loop PD detector and results in a wrong manipulation of the optical power. To reduce this effect, an optical band pass filter, 1400 nm ± 2.4 nm[9], is installed before the PD. The remaining instability caused by PT noise is estimated measuring the power fluctuations with an out-of-loop PD, the green RAM PD in figure 5.6. The resulting instability exceeds the thermal noise floor for averaging times above 10 s as shown in figure 5.9. However, this estimation is an upper limit, as the out-off-loop PD is not equipped with an optical band pass filter, but was only shielded from the laboratory illumination with moderate effort. It can be expected that this measurement is affected by stray light and especially light of other sources, since a full protection from light in the laboratory could not be

[9]item number FB1400-12 from Thorlabs

realized. Furthermore, pointing of the laser beam entering the cavity leads to higher power fluctuations on the out-of-loop RAM PD in front of the cavity when stabilizing the power of the light transmitted through the cavity using the in-loop PD behind the cavity. Figure 5.9 also shows the fractional frequency fluctuation based on the power fluctuations detected by the in-loop PD, giving a lower boundary of the expected laser fractional frequency instability caused by PT noise. As can be seen in figure 5.22, the out-of-loop signal is indeed an overestimation, as it surpasses the total measured noise of the entire laser system.

## 5.7. Vibration sensitivity

To make the cavity's optical length insensitive to seismic noise, vibration isolation platforms are used to reduce the seismic noise together with a special cavity mounting. These mountings in general fix the cavity in all spatial direction to make it transportable, but at the same time offer a low vibration sensitivity of the cavity's optical length. Such mountings were realized for spherical [47, 48], cubical [49, 50], cylindrical [51–55] and double tetrahedral [56] spacer designs. The cavity presented in this work uses a cylindrical design as it offers an increase in optical length without a cubic increase of spacer volume and therefore mass. This is especially advantageous for transportable systems, which head for a compact and light design, but at the same time a low thermal noise floor, which decreases with cavity length. The cylindrical mounting is based on the idea and findings of past cavities, especially Häfner et al. [51], 12 cm-long spacer, and Chen et al. [124], 10 cm-long spacer. Häfner et al. [51] present a comparable complex mounting, which allows independent mounting and optimization for the three spatial directions as well as avoids overdetermination of the degrees of freedom, while the mounting in Chen et al. [54] allows for independent mounting of the spatial direction but has an overdetermination of the degrees of freedom. In Chen et al. [54], vibration sensitivities of $0.8 \cdot 10^{-10}/g_0$, $0.17 \cdot 10^{-10}/g_0$ and $3.9 \cdot 10^{-10}/g_0$ were achieved in the horizontal ($x$-)direction, the vertical ($y$-)direction and along the cavity axis ($z$-direction), respectively. In Häfner et al. [51], vibration sensitivities of $2.3 \cdot 10^{-10}/g_0$, $0.7 \cdot 10^{-10}/g_0$ and $12.3 \cdot 10^{-10}/g_0$ were achieved in the vertical ($y$-)direction, the horizontal ($x$-)direction and along the cavity axis ($z$-direction), respectively, see table 5.3. According to the authors, the comparably high value along the cavity axis most likely originates from an imperfect realization of the mounting idea, an inclined wire in this case. Comparing these two mountings, the overdetermination of the mounting in Chen et al. [54] does not significantly increase the vibration sensitivity of the cavity, while a technically simple implementation is of interest as the vibration sensitivity of the mounting scheme is in the end limited by its technical feasibility. Therefore, the cavity mounting used in this work emphasizes a simple technical feasibility, at the cost of an over determination of the degrees of freedom.

The mounting concept applied here is based on the idea to independently mount the cavity in the three Cartesian directions, as this allows a mounting force that is only acting perpendicularly, $x$-, $y$-, and $z$-directions, to its corresponding symmetry planes,

Table 5.3.: Vibration sensitivity values for selected cavity designs.

| design | cylindrical | | | | cubic | |
|---|---|---|---|---|---|---|
| length | 20 cm (this work) | | 12 cm | 10 cm | 10 cm | 5 cm |
| | dynamic | static | [51] | [54] | [50] | [49] |
| horizontal ($x$) in $10^{-10}/g_0$ | 0.2(1) | 0.6 | 2.3 | 0.8 | 0.9 | 0.25 |
| vertical ($y$) in $10^{-10}/g_0$ | 0.3(3) | 4.1 | 0.7 | 0.17 | 2 | 0.02 |
| along optical axis ($z$) in $10^{-10}/g_0$ | 0.3(1) | 0.2 | 12.3 | 3.9 | 2 | 0.001 |

$y$-$z$-, $x$-$z$- and $x$-$y$-plane, of the cavity and thus accelerations do not change the optical cavity length in first order [125, 51]. To allow mounting perpendicular to the cavity's symmetry planes, the cavity design offers bars for the mounting in $x$- and $y$-direction and triangular ears for the mounting in $z$-direction, see figure 5.10. Due to tolerances in the manufacturing and assembling of the cavity components, its actual optical axis does not perfectly overlap with its ideal optical axis, the intersection line between $y$-$z$- and $x$-$z$-plane. Consequently, a tilt of the spacer's front faces would result in an optical length change. To avoid these tilts, the cavity is mounted at its Airy points [126] in $x$- and $y$-directions, which were found using FEM simulations. The cavity is mounted at 10 points, four in the $x$- and $y$-direction and two in the $z$-direction.

The expected vibration sensitivity for spacers with different length and diameter was simulated for such a 10-point-mounting using a FEM model based on experience with past cylindrical cavities, for example the achieved vibration sensitivities, the placement accuracy of the mounting points or the tilts in the mounting wires. Finally, a spacer design that allows for a thermal noise floor $\mathrm{mod}\,\sigma_\mathrm{y} \approx 7 \cdot 10^{-17}$ at $\tau = 1\,\mathrm{s}$ as calculated in section 5.4 and a predicted vibration sensitivity of approximately $5 \cdot 10^{-17}/\mu g_0$ was found. Thus, in combination with commercially available vibration isolation platforms, an instability of $\mathrm{mod}\,\sigma_\mathrm{y} \approx 1 \times 10^{-16}$ at $\tau = 1\,\mathrm{s}$ should be reached. The spacer has a length of 20 cm and a diameter of approximately 8 cm, see engineering drawing in appendix C.1.

To get an independent mounting in the three Cartesian directions, the mounting must be rigid perpendicular to the symmetry plane, but soft parallel to the symmetry plane and also symmetric to the cavity's planes of symmetry. The basis of the mounting is a spring steel wire welded to three set screws, one in the middle and two at its ends. A clamp for the bars and triangular ears is realized by the middle set screw in combination with a fluorine rubber ring, a washer and two nuts on each side, see figure 5.10. The two set screws at the end of the wire are used in combination with a fluorine rubber ring, two washers and a nut to preload the wire. Thus, equivalent to a preloaded rope, the force transfer along the wire is much larger than perpendicular to the wire, which allows independent mounting in the three Cartesian directions. Stainless steel stranded wire, as used in Häfner et al. [51], would seem to be more suitable as it is more flexible than spring steel wire. However, mechanical relaxations of stainless

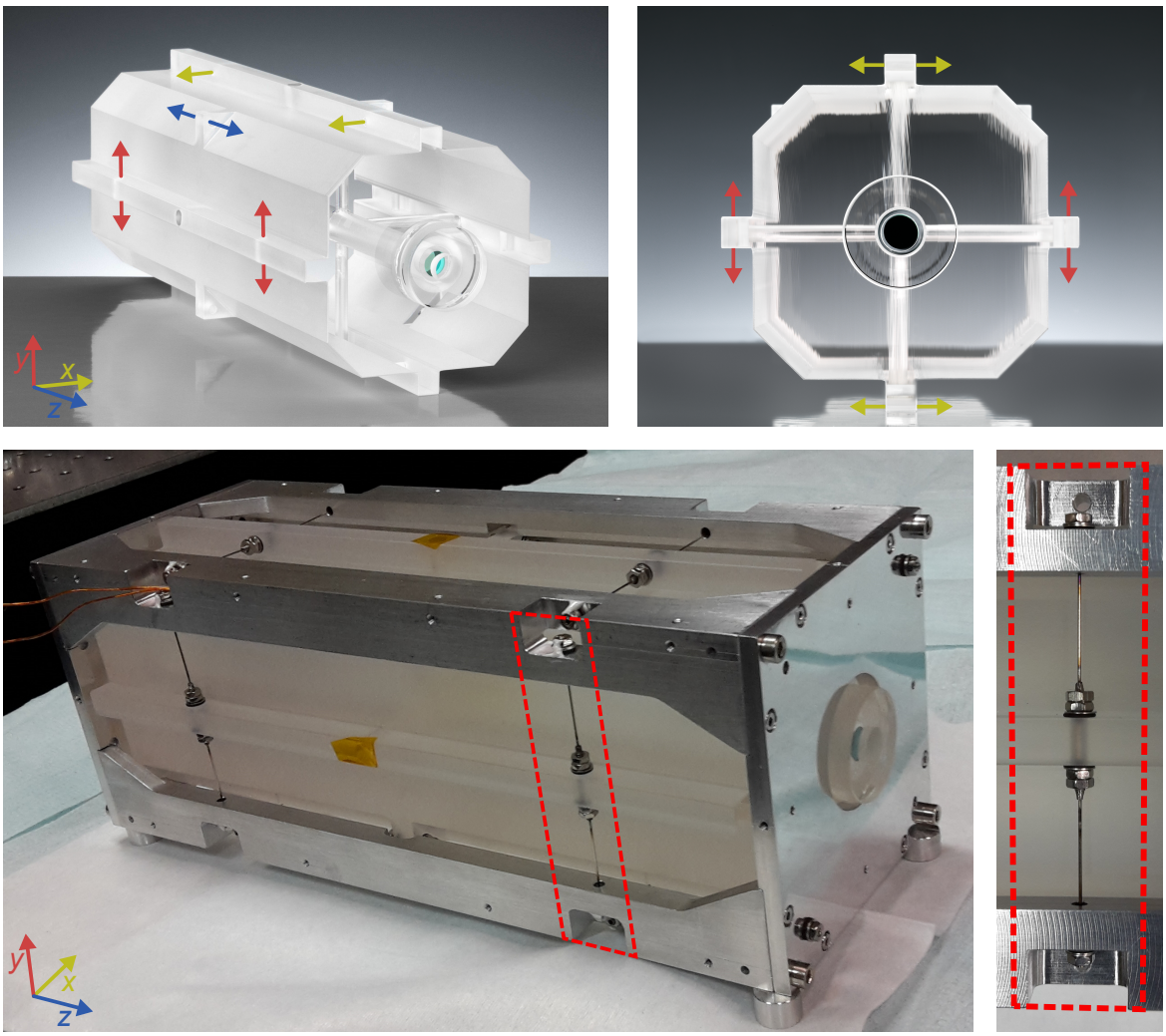


Figure 5.10.: Mounting of the cavity, for further description see text.

steel stranded wire are suspected to cause frequency jumps of a previous laser system [51]. The fluorine rubber rings compensate the higher stiffness of the spring steal wire and furthermore serve as thermal insulation, see section 5.9. The mounting is designed to withstand shock loads of 30 times the gravitational acceleration $g_0$, which allows all kinds of terrestrial transports of the system.

Especially, laser noise at the single cycle frequency $f_{\mathrm{cy}}$ contributes to the Dick effect assuming single Rabi or Ramsey interrogation [58]. For a single cycle duration $t_{\mathrm{cy}}$ of typically 1 s, this requires low laser instability especially around one 1 Hz. To achieve a low vibration sensitivity and thus a low laser instability at these frequencies, it is important that the cavity's eigenfrequencies are well above 1 Hz. The eigenfrequency of the spacer is calculated to be approximately 11 kHz. It is more complicated to estimate the resonance frequencies including the cavity mounting. Therefore, the complete setup, including the vacuum chamber, heat shields and vibration isolation table, as described in sections 5.8 and 5.9, was exited with an acoustic frequency sweep

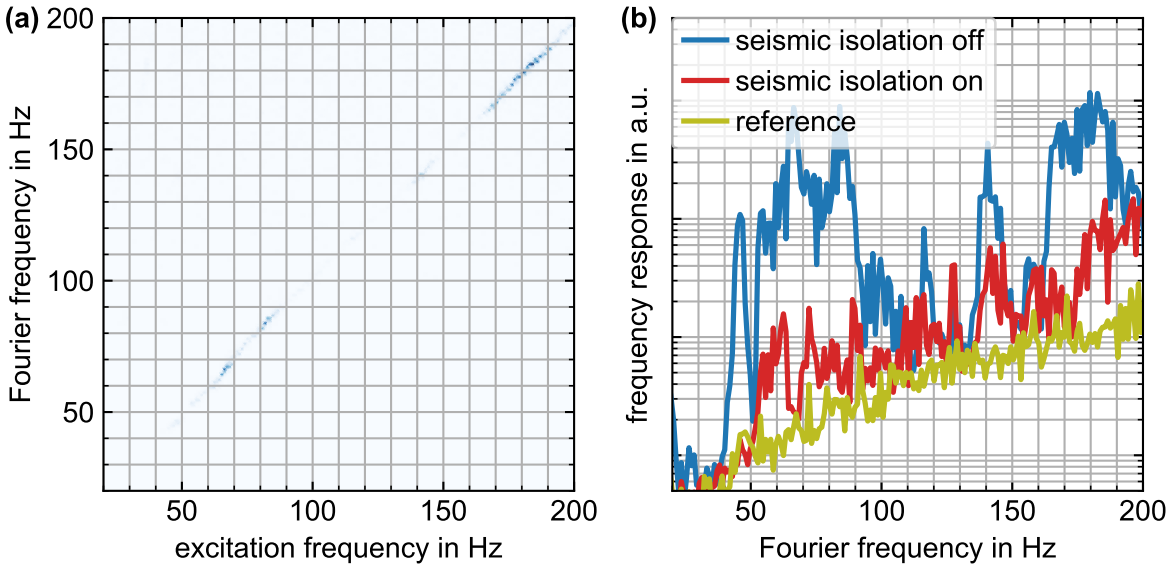


Figure 5.11.: (a) Frequency spectra of the laser frequency over the excitation frequency as a response to an acoustic frequency sweep. (b) Maximum values of the frequency spectra of a laser to an acoustic frequency sweep, see details in the text.

from 20 Hz to 200 Hz and the cavity's frequency response was observed as shown in figure 5.11. Figure 5.11 a shows the frequency spectrum of the laser frequency over time for an acoustic frequency sweep from 20 Hz to 200 Hz. Figure 5.11 b shows the maximum values of such a heat map for the single Fourier frequencies. The olive curve shows the frequency spectrum of the laser without acoustic excitation. The red curve shows the frequency spectrum of the laser when an acoustic frequency sweep is performed. The vibration isolation platform[10] was switched off, which should increase especially the impact of vibration caused by eigenfrequencies of the laboratory. The same acoustic sweep was played and the blue curve was detected. For frequencies below 50 Hz, the frequency spectrum of the red curve follows the reference curve, thus no significant impact of acoustic noise at these frequencies is expected to degrade the laser's instability. For frequencies above 50 Hz, a degradation of the cavity's instability is observed. However, by comparing the blue and red curve it seems that most of the frequency instability is caused rather by laboratory eigenfrequencies than by the cavity mounting, as they are significantly damped when the vibration isolation platform is switched on. Only the peak at roughly 128 Hz might be a cavity resonance as it appears with a similar height in both spectra. Thus, no eigenfrequency of the cavity mounting was found to be below 50 Hz and most likely also not below 120 Hz.

For Fourier frequencies much below the eigenfrequencies of the cavity, the transfer function between acceleration and deformation of the cavity and thus its optical length change is assumed to be constant. To estimate the remaining impact of seismic noise

[10] TS-150 from table stable

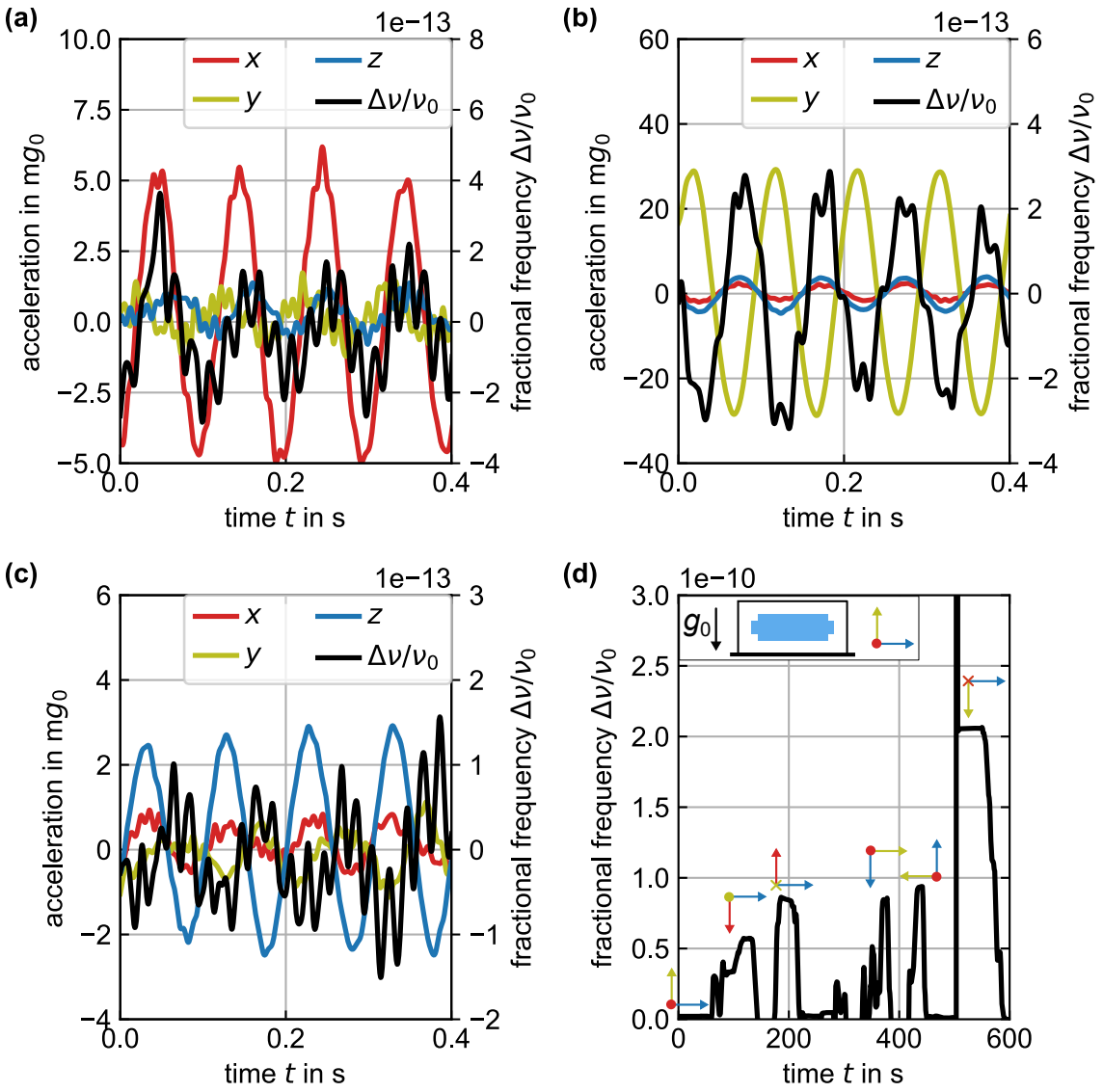


Figure 5.12.: (a-c) Dynamic vibration sensitivity measurement with an excitation frequency of 10 Hz. All curves are low-pass filtered with 100 Hz to increase the visibility of the oscillation. (d) Static vibration sensitivity measurement.

on the frequency instability, the vibration isolation platform was used as a shaking table and the cavity, within its complete setup including vacuum chamber and heat shields, was excited in all three Cartesian directions with a sine function between 7 Hz and 30 Hz. The seismometer placed on the vibration isolation platform separately detects the accelerations in all three Cartesian directions. Unfortunately, a perfect sine wave acceleration in one direction was not possible using the vibration isolation table as shaking table. Especially for the $x$- and $z$-direction, large accelerations in $y$-direction were detected, which for some measurement even exceed the accelerations

in the excited direction. With only one seismometer, the acceleration present at the position of the cavity can only be estimated with a large uncertainty. Thus, a second seismometer was placed at the platform and all eight actuators of the table were addressed separately. with proper adjustment of the eight input signals, the acceleration in the direction of interest exceeds the acceleration in the two other directions by at least a factor three. Figure 5.12 shows the acceleration measured in the three Cartesian directions of one of the two seismometers together with the fractional frequency change of the laser, which was measured against a second ultra-stable laser [43]. All the visible oscillations with higher frequency than the excitation frequency of 10 Hz are also present without the excitation and are not harmonics. The vibration sensitives as given in table 5.3, first column, were found.

In a second measurement to determine the cavity's vibration sensitivity, the cavity was turned upside down and its change in frequency was detected, see figure 5.12 d. The measurement was performed for all three Cartesian directions. The resulting vibration sensitivities are given in table 5.3, second column. The values found for the $x$- and $z$-direction are in the same order of magnitude for the static and the dynamic method, while for the $y$-direction the static value is one order of magnitude larger than the value found with the dynamic method. All values found with the static method tend to be larger than their equivalent dynamic value. This might be caused by a non linear behavior between cavity length change and the magnitude of the acceleration as assumed in first order. Especially, the $y$-direction is vulnerable against non linearity as the mounting of the heat shields is highly non symmetric to the $x$-$z$-plane, which might cause squeezing or stretching of the cavity due to mechanical stress in the heat shields and cavity mounting induced when turning the cavity upside down. Even if considering the higher static values, the vibration sensitivity of this 20 cm-long cavity is comparable to previous cavity designs with a length of at least 10 cm, see table 5.3. Considering the dynamic values, this 20 cm-long cavity provides lower vibration sensitivity than past cavities with a length of at least 10 cm.

Finally, the remaining seismic noise on the vibration isolation table was detected with a seismometer and using the average of the dynamic and static vibration sensitivity, the resulting fractional frequency instability was calculated, see figure 5.13. The lower contribution of the $y$-direction compared to the $x$- and $z$-direction at low Fourier frequencies is manly due to the much better vibration isolation of the platform in $y$-direction than in $x$- and $z$-direction, while the difference at higher Fourier frequency mainly results form the different vibration sensitivities in the Cartesian directions of the cavity. The fractional frequency instability caused by seismic noise in the $y$-direction might put a limitation to the laser's instability. However, this curve has a large measurement uncertainty resulting from the large difference between dynamic and static measurements. The large difference between the static vibration sensitivity and the dynamic vibration sensitivity may be caused by a non-linear behavior between fractional frequency change and acceleration instead of the linear behavior assumed so far. Such a non-linear behavior may for example be caused by the mounting of the heat shields, which are wedged between glass spheres. Assuming that the dynamic measurements give a better picture for the actual vibration sensitivity due to

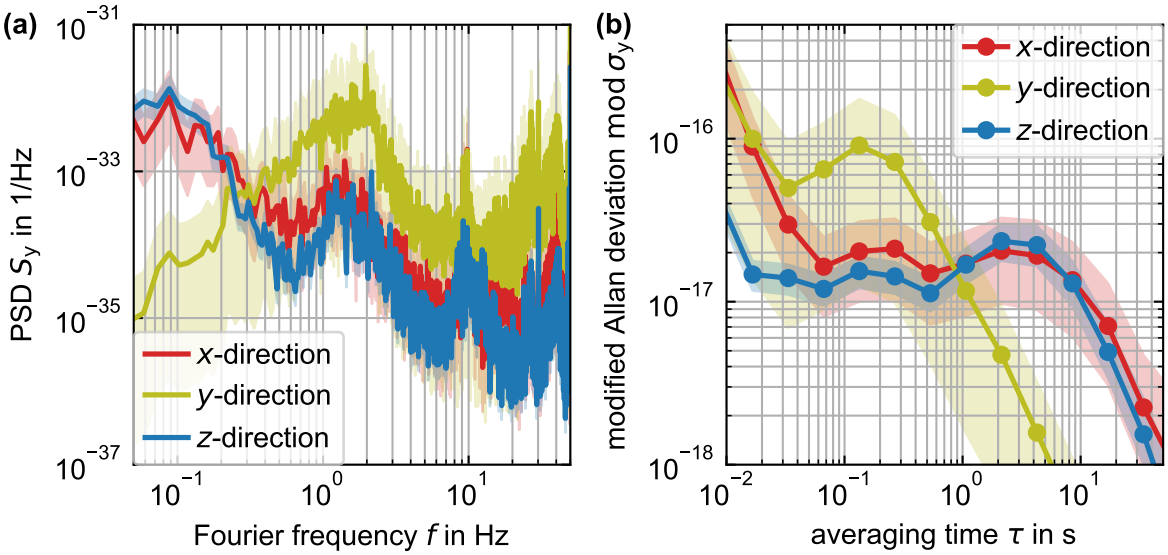


Figure 5.13.: Fractional frequency instability caused by seismic noise.

the lower acceleration during the measurement, the curve for the $y$-direction would shift down and result in an equal instability as the $x$- and $z$-direction, which would be sufficiently below the thermal noise floor. Otherwise, an active feed forward correction for remaining accelerations either to the laser's frequency or the vibration isolation platform itself might be implemented.

## 5.8. Pressure variations

A change in refractive index $n$ of the inter-mirror material causes a change in the optical cavity length $l_{\mathrm{opt}} = l_0 n$ and therefore the fractional length $\delta l/l_0$ and fractional frequency $\delta\nu/\nu_0$ stability of the cavity. The refractivity $n-1$ of air as a function of pressure is described by the Edlén equation [127], which is given in equation 5.7 for a wavelength of 1397 nm and a humnidity of 30 % [128, 129].

$$n - 1 \approx [2.68^{-9}/\mathrm{Pa}] \cdot p \tag{5.7}$$

This leads to a direct dependence between pressure fluctuations $\delta p$ and the fractional frequency stability $\delta\nu/\nu_0$ of the cavity.

$$\frac{\delta\nu}{\nu_0} = \delta n \approx [2.68^{-9}/\mathrm{Pa}] \cdot \delta p \tag{5.8}$$

With a target stability $\delta\nu/\nu_0 \approx 10^{-16}$ at one second, pressure fluctuations $\delta p \ll 3.7 \times 10^{-8}$ Pa over one second are required.

The pressure inside the cavity $p_{\mathrm{cav}}$ can be estimated with equation 5.9 based on the pressure at the pump $p_{\mathrm{pump}}$ and the pressure difference between the pump and the

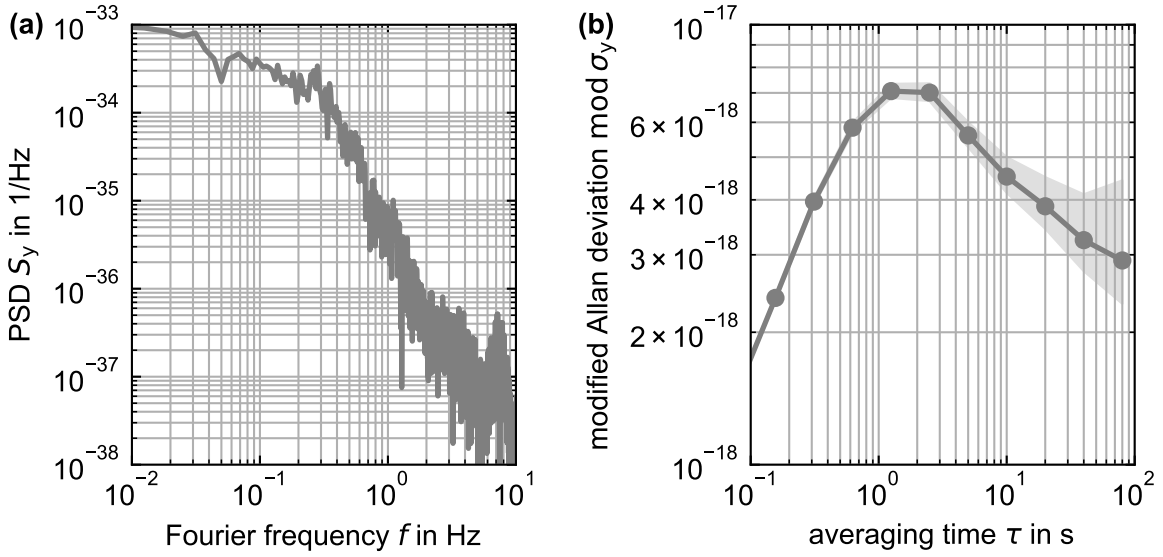


Figure 5.14.: Fractional frequency instability caused by pressure fluctuations.

inside of the cavity $\Delta p$.

$$p_{\mathrm{cav}} = p_{\mathrm{pump}} + \Delta p \tag{5.9}$$

In this setup, an ion pump[11] is used to generate low pressure in the vacuum chamber. From the pump current $I_{\mathrm{pump}}$, the pressure $p_{\mathrm{pump}}$ can be calculated using equation 5.10 given by the manufacturer.

$$p_{\mathrm{pump}} = \frac{0.0666}{10} I_{\mathrm{pump}} \frac{5600}{U_{\mathrm{pump}}} \tag{5.10}$$

$U_{\mathrm{pump}}$ is the voltage applied to the ion pump, which is 7 kV.

The pressure difference $\Delta p$ between the inside of the cavity and the pump is defined by the throughput $q_{\mathrm{pV}}$ and the conductivity of piping $K_{\mathrm{pipe}}$ [130].

$$\Delta p = \frac{q_{\mathrm{pV}}}{K_{\mathrm{pipe}}} \tag{5.11}$$

The conductivity of piping is given by $K_{\mathrm{pipe}} = 121 \varnothing^3_{\mathrm{pipe}} / l_{\mathrm{pipe}}$ assuming air as pumping gas, as for this setup the conductivity of piping is dominated by the ventilation holes of the spacer, as they have by far the smallest ratio of cubic diameter and length $\varnothing^3_{\mathrm{pipe}} / l_{\mathrm{pipe}}$. The throughput $q_{\mathrm{pV}} = p_{\mathrm{pump}} \cdot s_{\mathrm{eff}}$. $s_{\mathrm{eff}}$ is the effective pumping speed given by the pumping speed of the pump $s_{\mathrm{pump}}$ and the conductivity of piping $K_{\mathrm{pipe}}$: $1/s_{\mathrm{eff}} = 1/s_{\mathrm{pump}} + 1/K_{\mathrm{pipe}}$.

The pressure fluctuations at the ion pump were measured and their resulting fractional frequency instability was calculated with the equations above, see figure 5.14. The instability caused by pressure fluctuations is well below the expected thermal noise floor.

[11] The TiTan Ion pump 10SW from Gamma Vacuum

## 5.9. Temperature stabilization

In general, temperature changes lead to thermal expansion of a material. The correlation between expansion and temperature is expressed through the material's CTE $\alpha$. For some materials, the CTE itself has a strong temperature dependence and may even change from positive to negative values. Such CTE zero crossings, where $\alpha \approx 0$, help to reduce the impact of temperature fluctuations on the length of ultra-stable cavities. Materials with CTE zero crossings, which also offer decent material properties to get a low thermal noise as discussed in section 3.3, are for example sapphire, silicon or ULE glass. The most appropriate choice for a transportable setup is ULE glass, as its CTE zero crossing temperature $T_0$ is at room temperature, while sapphire and silicon offer CTE zero crossing temperatures at cryogenic temperatures.

ULE glass has adequate material properties to serve as spacer material, but is not a suitable choice as a substrate material. Due to its high mechanical loss factor, it would increase the cavity's instability above $10^{-16}$ as shown in figure 3.5. FS glass is used instead, which has a lower mechanical loss factor, but a CTE of $5 \times 10^{-7}\,\mathrm{K}^{-1}$ at room temperature. Due to its higher CTE, the FS glass substrate reduces the thermal length stability of the cavity and shifts its CTE zero crossing temperature as described by Legero et al. [113]. To reduce the impact of the FS glass mirror substrate on the thermal length stability of the cavity and push back its CTE zero crossing close to the one of a pure ULE glass cavity, ULE glass compensation rings are optically contacted to the backside of the mirror substrate as suggested by Legero et al. [113].

The fractional length change of a cavity spacer caused by a temperature change $\Delta T = T - T_0$ does only depend on $\alpha$, which is assumed to show a quadratic temperature dependence close to the CTE zero crossing temperature $T_0$.

$$\alpha(T - T_0) = \alpha'(T - T_0) + \alpha''(T - T_0)^2 \tag{5.12}$$

$$\frac{\Delta l(T - T_0)}{l_0} = \frac{1}{2}\alpha'(T - T_0)^2 + \frac{1}{3}\alpha''(T - T_0)^3 \tag{5.13}$$

$\alpha'$ is approximately $2 \times 10^{-9}\,\mathrm{K}^{-2}$ and $\alpha''$ is approximately $1 \times 10^{-11}\,\mathrm{K}^{-3}$ [113] for ULE glass close to its CTE zero crossing temperature $T_0$. Assuming that the cavity's temperature can be stabilized to its CTE zero crossing temperature $T_0$ within 0.5 K, a fractional length instability of below $1 \times 10^{-16}$ requires a temperature stability of below 0.1 µK.

Temperature stabilization is much more critical for temperature fluctuations at low frequencies, as the cavity's temperature response shows a low pass behavior. The cut-off frequency and damping are defined among others by the material's heat capacity and total mass of the resonator. Thus, a high resonator mass is advantageous to reach low temperature instability. However, portability of the laser system requires a compact and light-weight design. Another important impact on the cavity's temperature stability has the heat transfer between the cavity and its environment, which can be separated into thermal convection, thermal conduction and thermal radiation. Thermal convection is reduced to an insignificant level compared to thermal conduction

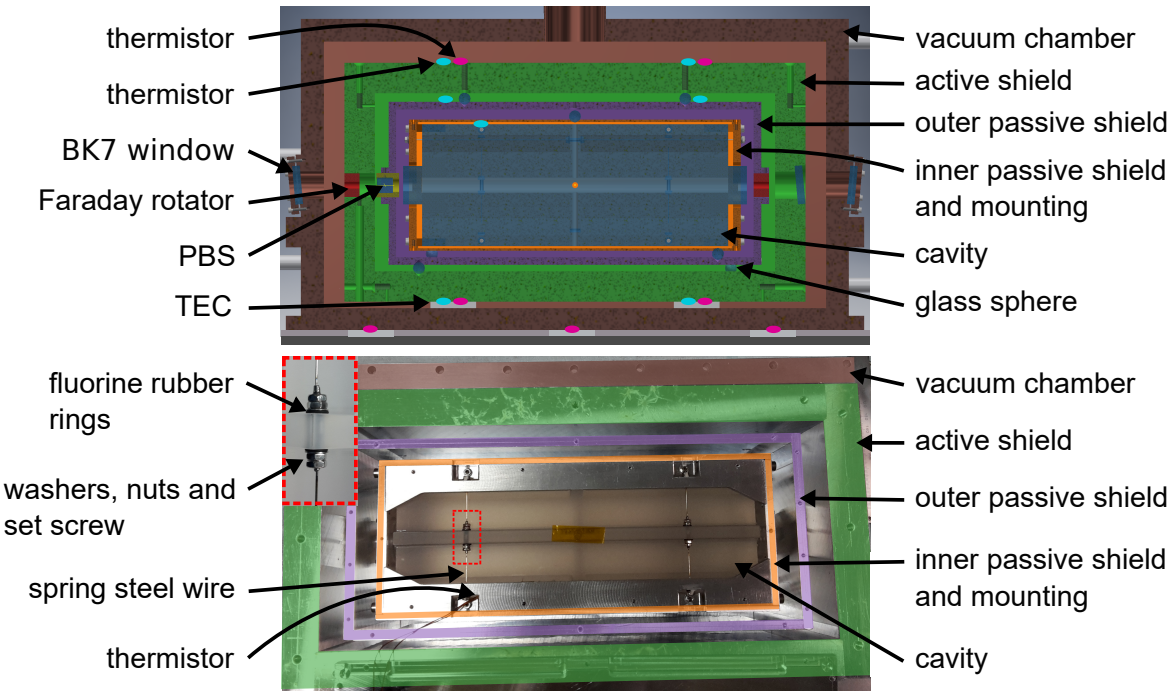


Figure 5.15.: Top: vertical cross section of the vacuum chamber. Bottom: top view of the vacuum chamber without cover plates.

and thermal radiation by placing the cavity in vacuum, which is already required due to the impact of pressure fluctuations on the cavity's optical length stability described in section 5.8. The heat transfer due to thermal conduction mainly depends on the thermal conductivity of the cavity mounting. Thus, materials with low thermal conductivity must be used. The heat exchange by thermal radiation can be reduced by surrounding the cavity with thermal heat shields with low emissivity. In the end, especially temperature fluctuations at low frequencies are expected to limit the cavity's length instability and therefore the laser's fractional frequency instability.

Based on the findings of passive and active temperature stabilization of past ultra-stable cavities [43, 121, 131, 51], the temperature stabilization shown in figure 5.15 was implemented. The cavity is placed inside a vacuum chamber including one active and two passive heat shields. The active heat shield is temperature stabilized to the CTE zero crossing temperature $T_0$ of the cavity with two separate control loops for the left and right side. Each control loop includes two thermoelectric coolers (TECs)[12] at the bottom of the shield, two negative temperature coefficient (NTC) thermistors[13] at the bottom and top of the heat shield, pink in figure 5.15, and a proportional-integral-derivative (PID) controller[14]. The average resistance of the top and bottom thermistor is used for the temperature control to take a vertical temperature gradient over the heat shield into account, mainly caused by the fact that all TECs are placed at

[12]PKE 71 a 0020 4 H 200 from Peltron GmbH Peltier-Technik
[13]B57560G1103 NTC thermistor from TDK Electronics
[14]TEC-1091 from Meerstetter Engineering GmbH

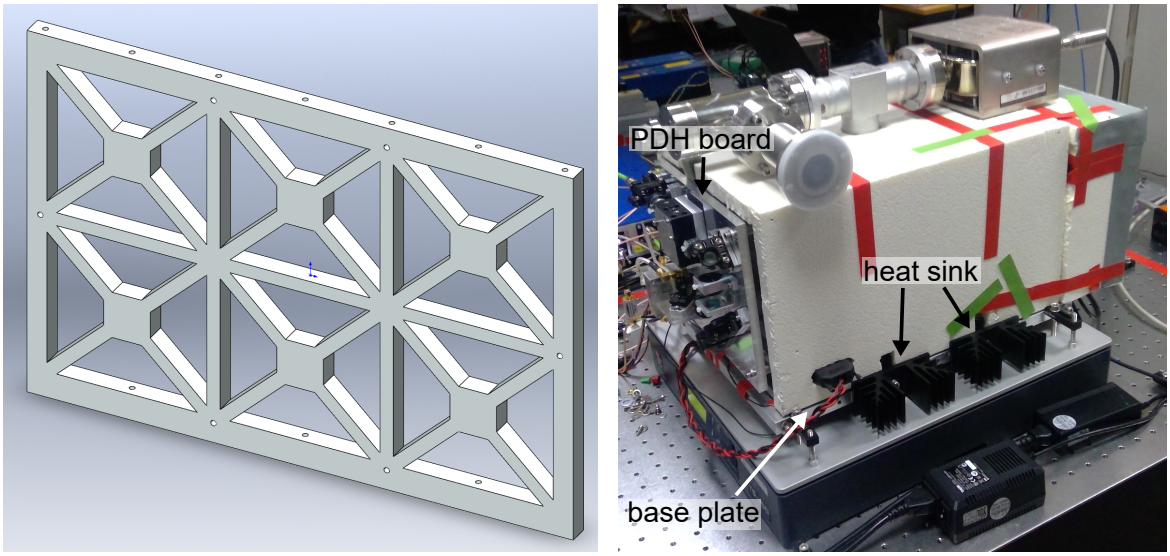


Figure 5.16.: left: base plate design, right: picture of the cavity

the bottom of the heat shield. 125 µm-thick Indium foil is placed between the TECs and the vacuum chamber as well as the active heat shield to ensure good thermal contact and to compensate small height differences for example between the single TECs. To ensure low thermal conductivity between the single heat shields, three glass spheres with a diameter of 8 mm, which are place in cone-shaped recesses of the shields, separate the shields from the bottom. From the top, screws with fluorine rubber tips push down glass spheres to assure a rigid mounting of the cavity. The cavity itself is mounted using spring steel wires, which are welded to set screws. Details of this mounting are given in section 5.7.

In addition to the active temperature stabilization of the outermost heat shield, the vacuum chamber is temperature stabilized equivalently to the active heat shield, but using only one thermistor at the bottom of the vacuum chamber and three control loops. The aluminum base plate in combination with heat sinks, as shown in figure 5.16, serves as heat sink for the vacuum chamber. Additionally, the vacuum chamber including the PDH board and optics for the power stabilization on the backside are covered with extruded polystyrene foam (XPS) plates for thermal isolation. The entire setup weighs 43 kg. The outer dimensions of the vacuum chamber are 20.5 cm·24 cm·38 cm.

To characterize the temperate sensitivity, a temperature step was applied to the active heat shield, which caused a temperature change of the innermost heat shield from 293 K to 303 K over seven days. The laser frequency was compared to a second ultra-stable laser, from which the fractional length change of the cavity was derived. In figure 5.17, the fractional length change is plotted over the temperature measured by the thermistor connected to the cavity's mounting frame. The CTE zero crossing was found after two and a half days at a temperature of 297.4 K of the innermost heat shield, however, the heat shield's temperature was still changing at a rate of

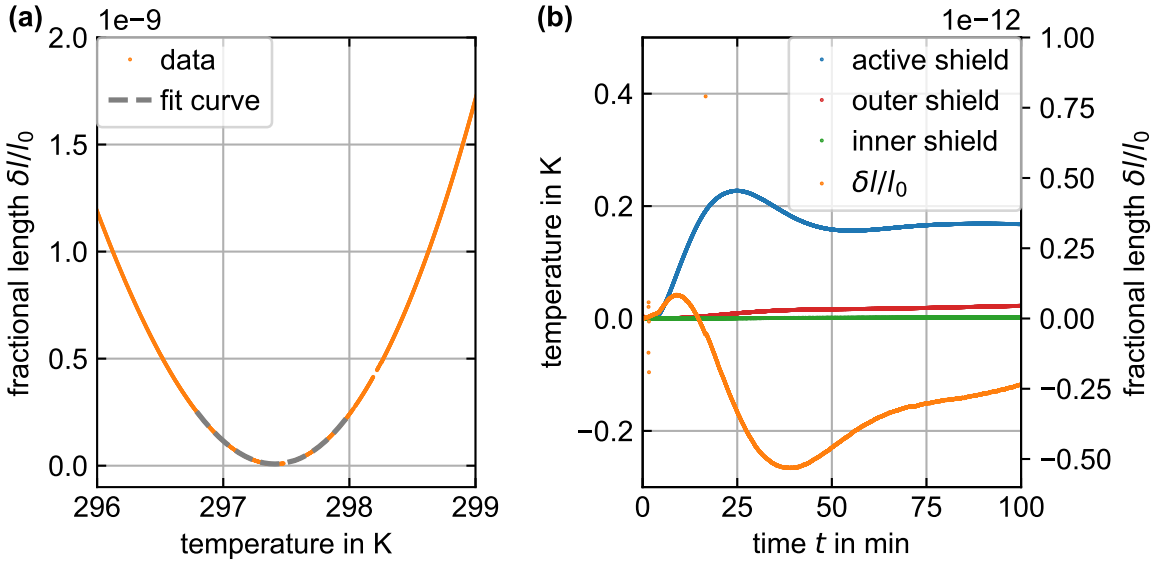


Figure 5.17.: (a) Fractional length change of the cavity plotted over the temperature measured at the cavity mounting frame. Fit function as given in equation 5.13. (b) Response of the passive heat shields and the cavity's fractional length change to a temperature change of the active heat shield.

$1.8\,\mathrm{mK\,min^{-1}}$. From the step response in figure 5.19, which is described later, the temperature of the cavity at this point in time is estimated to be lower by approximately 2 K compared to the innermost heat shield. Thus, the actual zero crossing of the CTE of the cavity is approximately at 295.4 K. The curve of figure 5.17 a was used with equation 5.13 to derive $\alpha'$ and $\alpha''$, which leads to an over estimation of approximately 6 % of these two values as the actual cavity temperature shows a steeper increase compared to the inner passive shield after 2.5 d, see figure 5.19. $\alpha'$ is $1.3 \times 10^{-9}\,\mathrm{K^{-2}}$ and $\alpha''$ is $8 \times 10^{-11}\,\mathrm{K^{-3}}$. For previous cavities with an ULE spacer, FS mirror substrates and ULE compensation rings, $\alpha'$ is $8.6 \times 10^{-10}\,\mathrm{K^{-2}}$ for an 12 cm long cavity and $2.2 \times 10^{-9}\,\mathrm{K^{-2}}$ for an 48 cm long cavity [121].

Figure 5.17 b shows the transient behavior of the active heat shield, blue curve, along with the temperature of the outer and inner passive heat shields, red and green, and the fractional length change of the cavity, orange, after the set temperature of the temperature controller was changed at a time of 4 min. If more than one out-of-loop thermistor was available per heat shield, the resulting average temperature is plotted. While the temperatures of the passive heat shields show the expected low pass behavior, an immediate response of the fractional length of the cavity to a temperature change of the active heat shield is observed instead of the expected low pass behavior. This immediate response of the cavity's fractional length might be caused by thermal expansion of the heat shield, which causes mechanical stress in the mounting structure and thus stretches, squeezes or bends the cavity due to the over determined mounting of the cavity. If this is the case, the response should be unaffected by the CTE of the cavity and rather scale with the step size of the temperature change

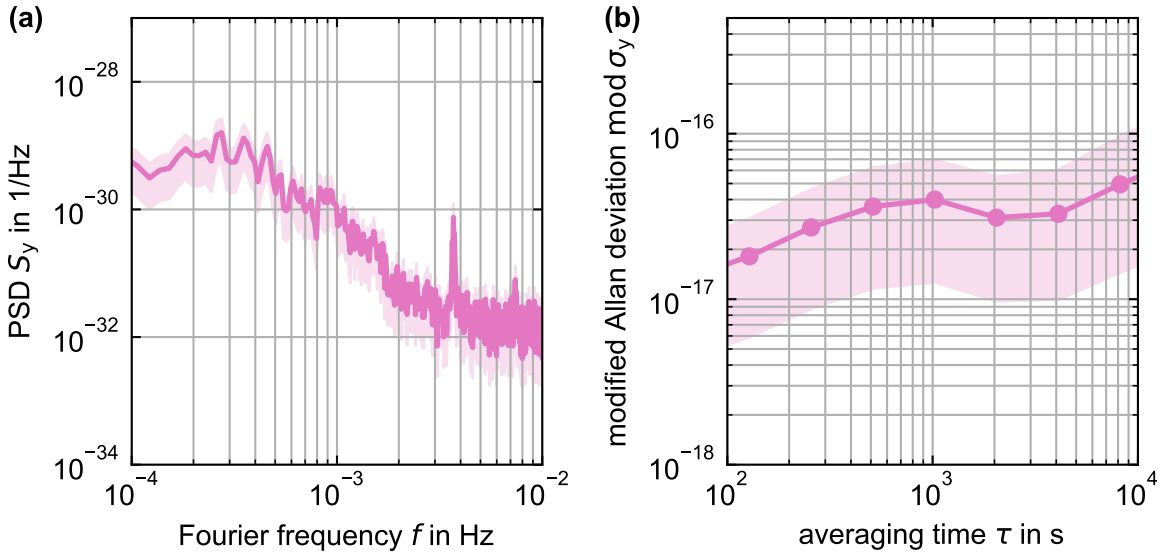


Figure 5.18.: Fractional frequency instability caused by thermal stress.

of the active heat shield. For different temperature steps, the response of the cavity's fractional length shows a similar behavior compared to figure 5.17 b and it's amplitude scales roughly with the temperature step size, while a correlation with the CTE of the cavity was not found. As a first simple approximation, a directly proportional relationship between the active shield temperature and the fractional length change was assumed. A conversion factor of $3(2) \times 10^{-12}\,\mathrm{K}^{-1}$ was derived from the maximum values of the two curves. Figure 5.18 shows the fractional frequency instability caused by thermal stress. For Fourier frequencies below $1 \times 10^{-3}\,\mathrm{Hz}$ or averaging times above $5 \times 10^{2}\,\mathrm{s}$ the instability is in the order of the thermal noise floor, but still below. For frequencies above $1 \times 10^{-3}\,\mathrm{Hz}$ or averaging times below $5 \times 10^{2}\,\mathrm{s}$ it is well below the thermal noise floor. Thus, only the long term stability of the laser might be affected by the thermal stress. This effect most likely could be reduced by a more complex cavity mounting, which avoids an over determination as presented in Häfner et al. [51]. Possibly, a temperature change of the passive heat shields may also cause thermal stress, however, their temperatures change much slower, thus rendering such an effect likely invisible. No fractional length response to a change of vacuum chamber temperature was observed.

Figure 5.19 shows the long term response of the passive heat shields' temperature and the fractional length of the cavity to a step in temperature of the active heat shield. The initial offset of the curves was removed and the responses are normalized to their absolute change $[T(t) - T(0)]/\Delta T$ and $[\delta l(t) - \delta l(0)]/\Delta l$, respectively. Thus figure 5.19 a shows the response to a unit step function. The temperature step of 0.2 K was performed 4 K away from the zero crossing temperature of the CTE. Thus, approximately a linear behavior between temperature change of the cavity and its length change can be be assumed. Equation 5.14 describes the temperature response of the cavity to a unity step function at the active heat shield for a design using

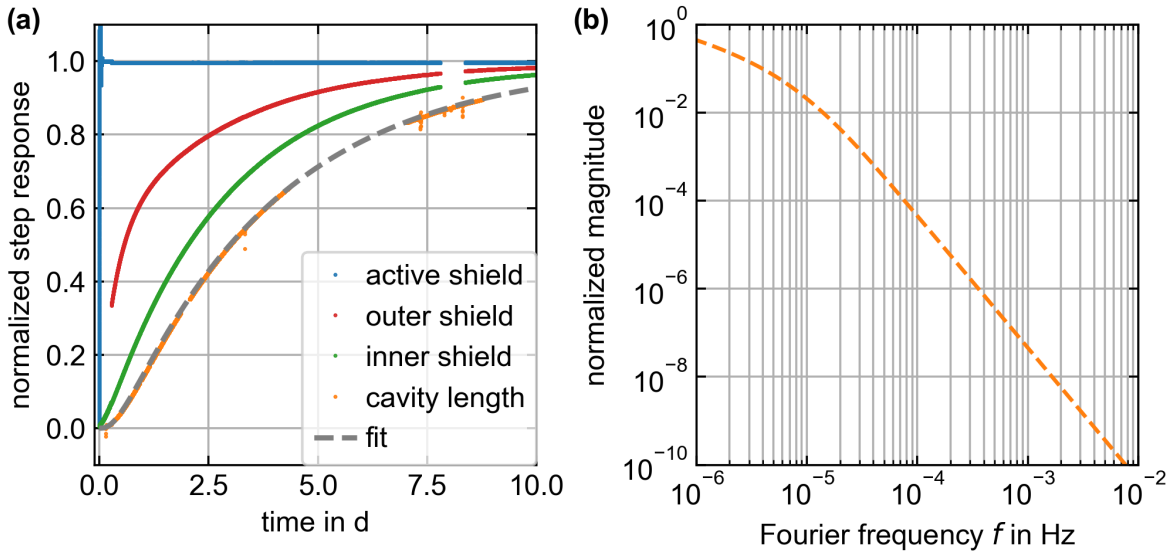


Figure 5.19.: (a) Normalized step response of the passive heat shields' temperatures and the fractional cavity length to a temperature step of the active heat shield. (b) Normalized amplitude response of the fractional cavity length to the temperature of the active heat shield.

two passive heat shields, assuming that the heat transfer between the shields and the cavity is defined by thermal conduction and radiation between the shields, while thermal convection and thermal radiation directly from outside the vacuum chamber through the windows to the cavity is neglected, which is a good approximation for a cavity operated close to room temperature and placed in ultra-high vacuum [121].

$$\begin{aligned}\frac{T_{\mathrm{cav}}(t)-T_{\mathrm{cav}}(0)}{\Delta T_{\mathrm{cav}}} = 1- \Bigg[ & \frac{t_{\mathrm{a}}^2}{[t_{\mathrm{a}}-t_{\mathrm{b}}][t_{\mathrm{a}}-t_{\mathrm{c}}]} \exp\left(-\frac{t}{t_{\mathrm{a}}}\right) \\ & - \frac{t_{\mathrm{b}}^2}{[t_{\mathrm{a}}-t_{\mathrm{b}}][t_{\mathrm{b}}-t_{\mathrm{c}}]} \exp\left(-\frac{t}{t_{\mathrm{b}}}\right) \\ & + \frac{t_{\mathrm{c}}^2}{[t_{\mathrm{a}}-t_{\mathrm{c}}][t_{\mathrm{b}}-t_{\mathrm{c}}]} \exp\left(-\frac{t}{t_{\mathrm{c}}}\right) \Bigg]\end{aligned} \tag{5.14}$$

For this setup $t_{\mathrm{a}} = 0.11\,\mathrm{d}$, $t_{\mathrm{b}}$ 0.34 d and $t_{\mathrm{c}} = 3.64\,\mathrm{d}$ were found as shown by the grey curve in figure 5.19 a. The transfer function was derived by calculating the FFT of the derivative of the step response, which is the impulse response. Figure 5.19 b shows the normalized amplitude response of the system.

The resulting fractional frequency instability caused by temperature changes of the cavity was derived from the average temperature fluctuations of the active heat shield measured with the four out-of-loop thermistors, cyan in figure 5.15, which are about a few 100 µK for the active heat shield over a day. The cavity is operated at its zero crossing temperature within 1 K uncertainty, thus $\alpha = 1.4 \times 10^{-9}$ is assumed for the conversion from temperature to fractional frequency fluctuations. Together with the

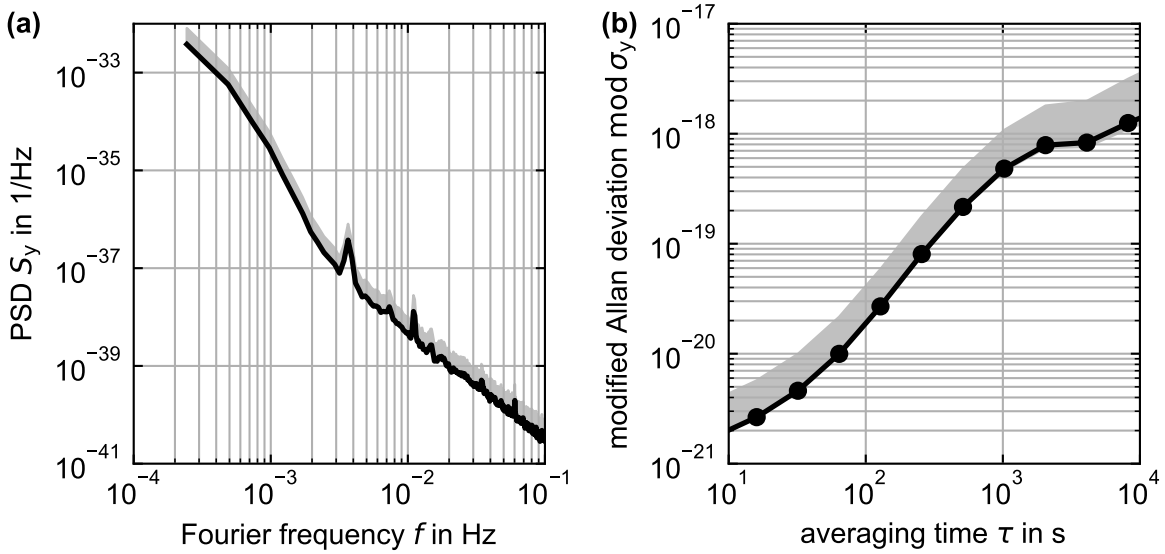


Figure 5.20.: Fractional frequency instability caused by temperature changes of the active heat shield operated 1 K away from the zero crossing temperature, black line, and 2 K away from the zero crossing temperature, pale black line.

amplitude response as shown in figure 5.19 b, the fractional frequency instability of the laser as shown in figure 5.20 was calculated. The instability caused by temperature fluctuations of the active heat shield is well below the thermal noise floor limit.

The frequency drift caused by aging of the spacer was observed to be $23\,\mathrm{mHz\,s^{-1}}$. This drift decays exponentially over time with time constants of several years and is caused by an ongoing crystallization of the glass [132, 133]. The constant drift was removed before analyzing the data as during clock operation constant frequency drifts can be compensated by the double-pass AOM on the laser distribution breadboard.

## 5.10. Measured laser instability

The clock laser's fractional frequency instability was measured against a second ultra-stable laser [44] via a frequency comb with the setup shown in figure 5.6. The beat frequency between the two lasers was detected with a sampling rate of 100 Hz or 1 Hz by a frequency counter[15]. The fractional frequency instability of the laser was directly calculated from the fluctuations of the beat frequency, which are dominated by the instability of the laser presented in this work, as the second laser system shows an instability of at least a factor two lower [44]. Figure 5.21 shows the median of the fractional frequency instability of multiple measurements, cyan lines, and their maximum and minimum values, shaded areas, for measurements with 100 Hz or 1 Hz sampling rate. For averaging times between 1 s and 100 s, the maximum values are

[15] K+K FXE from K + K Messtechnik GmbH, using lamda averaging

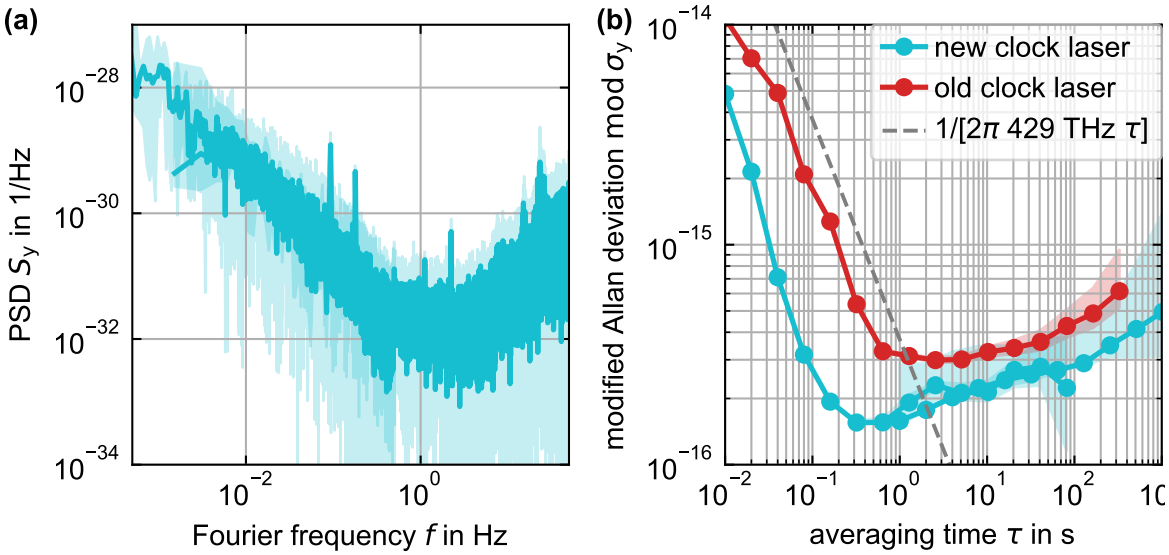


Figure 5.21.: Fractional frequency instability of the new clock laser, cyan, and the old clock laser, red. Reference line to determine the coherence time for Ramsey spectroscopy, see equation 2.1.

caused by occasional events like failure of an active stabilization or the re-locking of the laser to the cavity. Thus, the median was chosen instead of the mean to give a better picture of the typical instability of the laser system.

For averaging times around 0.1 s, the laser's mADEV is reduced down to a seventh compared to the old laser system [51], red curve. For longer averaging times, $\tau > 1\,\mathrm{s}$, the mADEV is reduced to two-thirds of the old laser's instability. Assuming Ramsey interrogation, the coherence time as defined in equation 2.1 increases from 1 s to 2 s with the new clock laser.

Figure 5.22 shows the laser's fractional frequency noise along with the different technical noise contributions described in the previous sections. The uncertainties of the single measurements are not included here for better readability of the figure. Note that the absolute values of the mADEV depend to a certain extend on the sampling conditions like the sampling frequency and pre-averaging of the values, which differs between the measurements as different instruments were used. Thus, for comparisons between the absolute values, rather the PSD should be used.

For averaging times below 0.1 s or Fourier frequencies above 5 Hz, the measured fractional frequency instability agrees within the uncertainties with the instability caused by optical path length stabilization including the electronic noise of the beat note detection. Similar components were used for the beat note detection and recording in both measurements. Thus, this noise is expected to be approximately the same in both measurements. The higher instability of the previous clock laser [51] at this averaging times originates most likely from an uncompensated optical fiber between laser distribution breadboard and the cavity. Thus, for low instabilities below averaging times of 0.1 s or Fourier frequencies above 5 Hz, optical path length stabilization in all optical paths is unavoidable.

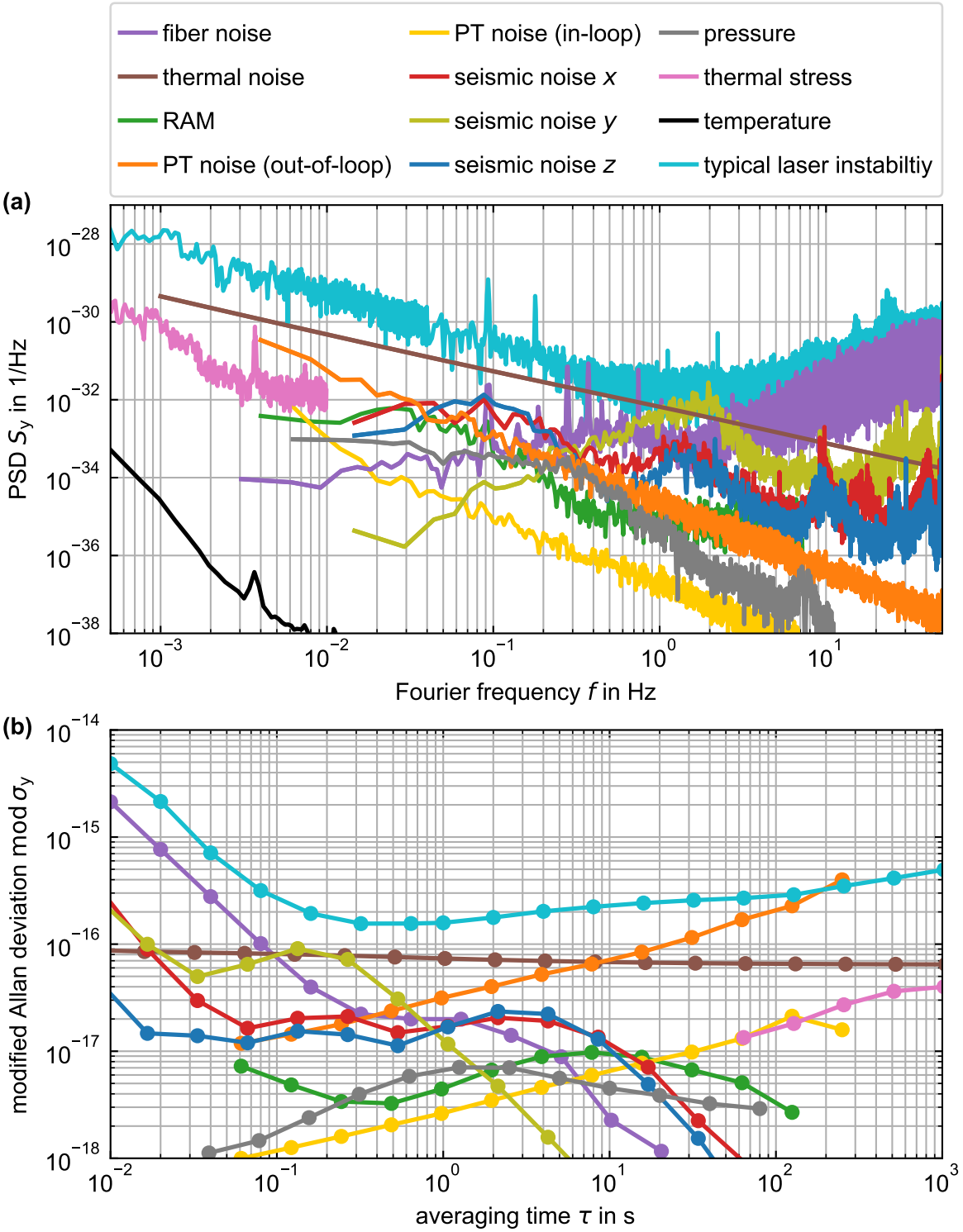


Figure 5.22.: Fractional frequency instability of the new clock laser together with all investigated noise contributions.

At averaging times around 0.2 s or Fourier frequencies of 2 Hz, seismic noise might put a limitation to the clock laser's fractional frequency instability. However, as discussed before, when taking only the dynamically derived vibration sensitivity into account, the seismic noise is not expected to limit the laser's instability.

For averaging times above 0.5 s or Fourier frequencies below 1 Hz, the instabilities caused by thermal noise, PT noise, thermal stress and temperature fluctuations are the biggest contributions. However, the measured laser instability is higher than expected based on these contributions, which normally are expected to limit the lasers instability at this time scale.

The instability caused by thermal stress might be underestimated in absence of a good model to describe this effect. However, the findings so far suggest that the instability decreases with smaller temperature fluctuations. It is also known from recent conferences that other groups also struggle to reach the predicted thermal noise floor for $Al_{0.92}Ga_{0.08}As/GaAs$ mirrors using a system based on a 21 cm-long Silicon cavity operated at cryogenic temperatures. Yu et al. [134] investigated birefringence noise appearing with different sign for the slow and fast axis of their cavity, which currently seems to limit their fractional frequency instability to the mid $10^{-17}$ range. However, the origin of this noise is not found yet and it has to be investigated whether it is also a dominant contribution for room temperature cavities.

Nevertheless, the laser system presented here achieves an instability slightly below the instability theoretically achievable with fused silica ($SiO_2$)/tantalum pentoxide ($Ta_2O_5$) mirrors of $2 \cdot 10^{-16}$ as shown in figure 3.5 b and outperforms previously published transportable clock laser systems.

# 6. Frequency Doubling

As $Al_{0.92}Ga_{0.08}As$/GaAs mirror coatings are absorbing at the $^{87}Sr$ clock transition frequency of 429.2 THz, corresponding to a wavelength of 698 nm, the system is operated at 214.6 THz, a wavelength of 1397 nm, which is twice the clock transition wavelength. Thus, frequency doubling using a periodically-poled lithium niobate (PPLN) waveguide frequency doubler[1] is performed to shift the laser frequency to the $^{87}Sr$ clock transition frequency. Frequency doubling can be implemented in an optical clock laser system as simply as shown in figure 6.1. Here, the fundamental light at 1397 nm, passing trough the frequency doubler, is reflected back by a dichroic mirror and is used for the optical path length stabilization, while the frequency doubled light at 698 nm is used to interrogate the atoms.

To not degrade the laser frequency stability, this setup requires a sufficiently constant phase between the fundamental light and the frequency doubled light. Excess phase noise in the second-harmonic generation (SHG) process can be caused by several effects like amplitude-to-phase conversion, the Kerr effect or thermal noise [136, 137]. The excess phase noise and phase evolution in a PPLN waveguide frequency doubler was investigated under steady-state operation and for light pulse generation within this work in view of frequency doubling in a clock laser with the simple setup in figure 6.1. This investigation has already been published in Herbers et al. [135] and the main findings are shortly repeated hereinafter for the sake of completeness.

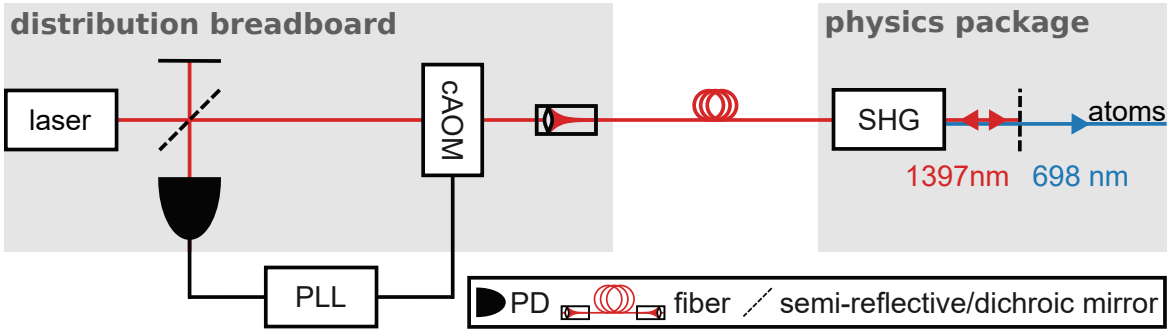


Figure 6.1.: Implementation of frequency doubling in a clock laser system [135].

[1] WH-0698-000-A-B-C from NTT Electronics

## 6.1. Steady-state operation

To measure the phase noise between fundamental and frequency-doubled light, other phase and frequency noise, like laser frequency noise, AOM noise and phase noise caused by optical path length fluctuations must either be passively rejected by a clever processing of the optical and electronic signals or suppressed significantly below the SHG noise by active stabilization.

The setup and signal processing as shown in figure 6.2 a rejects laser noise, AOM noise and phase noise caused by optical path length fluctuation [135]. Thus, only the excess phase noise of the SHG remains, which is recorded by a phase comparator implemented on a field-programmable gate array (FPGA).

The PSD of the fractional frequency noise resulting from the excess phase noise under steady-state operation of the PPLN waveguide frequency doubler is shown along with the electronic noise of the setup and the laser's fractional frequency instability, see figure 6.2 b.

For Fourier frequencies above a few hertz, the measurement of the excess phase noise is limited by the electronic noise of the setup, while for lower frequencies fractional frequency instabilities below $1 \times 10^{-34}\,\mathrm{Hz}^{-1}$ were found. For all Fourier frequencies investigated, the instability caused by excess phase noise of the glsPPLN waveguide frequency doubler is well below the laser's fractional frequency instability and thus does not degrade it.

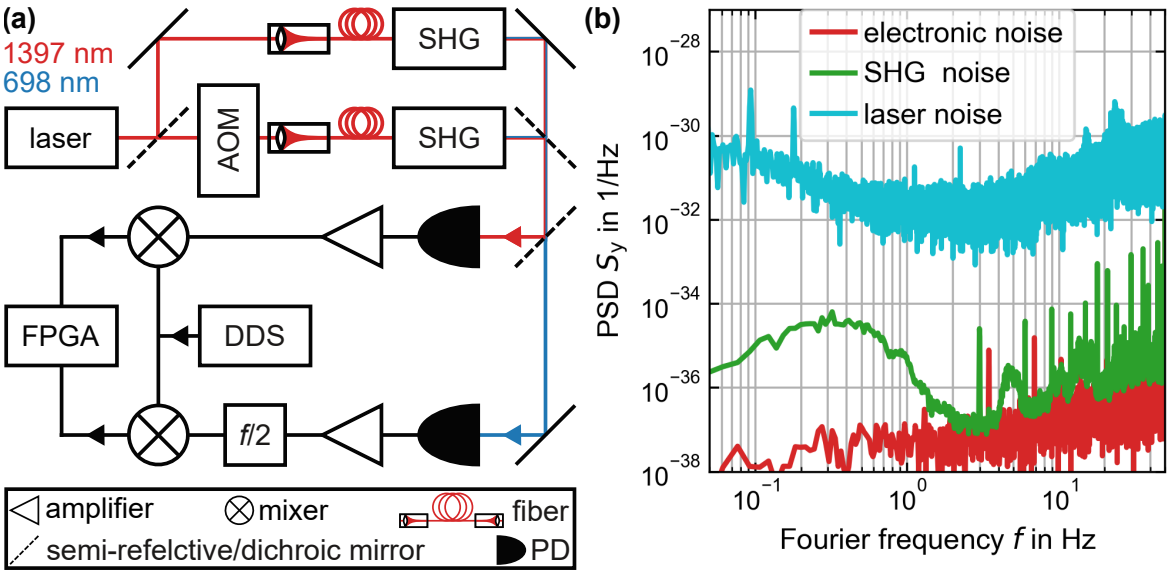


Figure 6.2.: (a) Setup to determine the excess phase noise of PPLN waveguide frequency doublers [135]. (b) PSD of the fractional frequency instability caused by electronic noise of the setup, excess phase noise of PPLN waveguide frequency doublers and the instability of the clock laser system for comparison. [135]

## 6.2. Light pulse generation

Using the setup shown in figure 6.1, the pulses for interrogating the atoms are generated by modulating the optical power of the fundamental light. A change in optical power causes a temperature change in the crystal due to absorption and thus, among others, a change in refractive index, which in turn results in a phase evolution between the fundamental and frequency doubled light. Such a phase evolution results in a frequency offset between the clock laser frequency and the atomic transition frequency and thus adds a systematic frequency shift to the clock transition frequency.

The setup as described in figure 6.2 a was used to investigate the phase response caused by sudden power changes of the fundamental light by step wise changing the optical power of the fundamental light with the AOM. Assuming an exponential behavior of the phase response to sudden changes in power, a decay time of 0.21(14) s and a sensitivity of $56(28) \times 10^{-5}\,\mathrm{rad\,mW^{-1}}$ was found [135].

The expected phase evolution for Rabi and Ramsey interrogation caused by sudden power changes like interrogation pulses, is schematically shown in figure 6.3 a. For Ramsey interrogation, the phase difference increases exponentially during the first $\pi/2$-pulse and decreases exponentially during the dark time. However, the phase difference does not decay to zero and starts from a non-zero value for the second $\pi/2$-pulse, during which it increases exponentially again. For Rabi interrogation, the phase difference increases exponentially during the whole $\pi$-pulse. The offset resulting from the decay during the dead time is not considered for the sake of simplicity, leading to a slight overestimation of the fractional frequency shift if the offset is constant. The

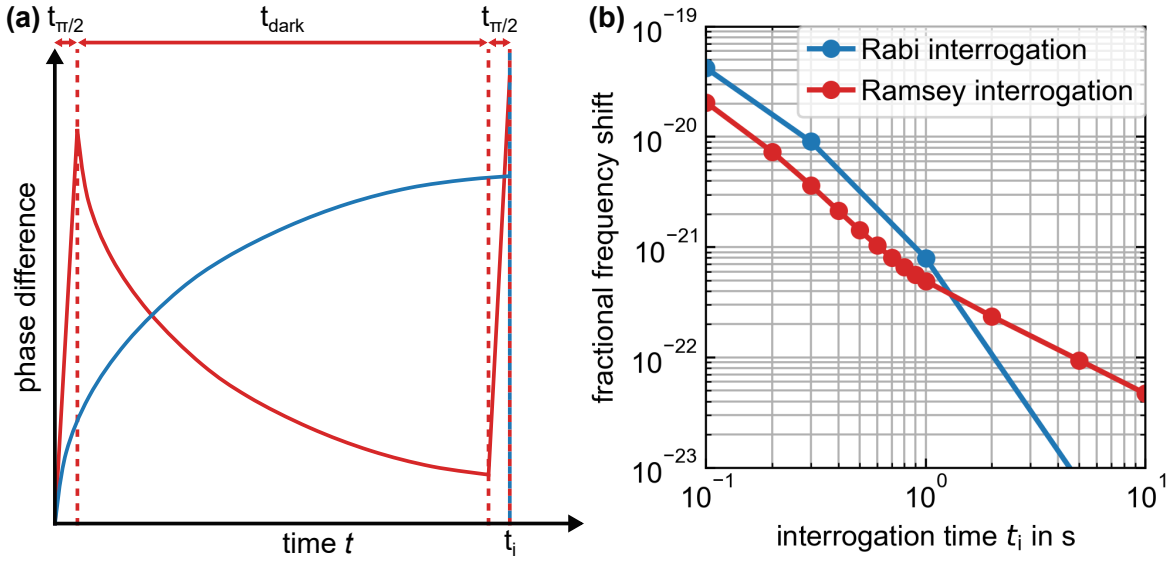


Figure 6.3.: (a) Schematic sketch of the phase evolution between fundamental and frequency doubled light of a PPLN waveguide frequency doubler for Rabi and Ramsey interrogation. (b) Fractional frequency shift resulting from the phase evolution during Rabi and Ramsey interrogation. [135]

curves for the resulting fractional frequency shifts shown in figure 6.3 b were calculated using typical values for a $^{87}$Sr lattice clock and a PPLN waveguide frequency doubler by Herbers et al. [135]. They are well below the systematic uncertainty of today's optical clocks, which is in the order of $10^{-18}$ [18, 138].

# 7. Progress in optical clocks

Within this work, a laser system based on a cavity with crystalline $Al_{0.92}Ga_{0.08}As/GaAs$ mirror coatings, FS glass mirror substrates and a 20 cm-long ULE glass spacer was presented. So far, few investigations on cavities based on crystalline mirror coatings have been published, but none of them did reach their predicted thermal noise floor or outperformed the expected instability with $Ta_2O_5/SiO_2$ mirrors, due to instabilities either caused by newly-discovered birefringence noise in cryogenic cavities [134] or caused by technical noise sources like temperature fluctuations or seismic noise [56].

The laser system presented here shows the lowest fractional frequency instability among published transportable laser systems, even outperforming PTB's current transportable laser system [51], which had the lowest fractional frequency instability until now. All components of the presented laser system were investigated in view of technical noise limiting the laser instability, including the light distribution, the frequency doubling, the reference resonator and the electronics.

The laser system achieves an instability as low as $\mathrm{mod}\,\sigma_y = 1.6 \cdot 10^{-16}$, which is already a factor 1.3 lower than the theoretically possible instability of $\mathrm{mod}\,\sigma_y = 2{\cdot}10^{-16}$ with $Ta_2O_5/SiO_2$ mirrors. Depending on the averaging time of interest, the fractional frequency instability has been reduced by a factor of up to seven compared to PTB's current transportable laser system. This reduced instability allows a reduction of the Dick effect limit by roughly a factor of four as shown in figure 7.1 for interrogation times below 0.5 s, which would reduce the clock's instability significantly.

However, despite these good results, the expected thermal noise floor of the cavity's fractional frequency instability, which is in the high $10^{-17}$ range, has not been reached yet. A further reduction of the instability caused by seismic noise, for example by an active feed forward correction to the vibration isolation table or the laser frequency as described in section 5.7, could reduce the laser's instability at around 0.2 s averaging time or Fourier frequencies around 2.5 Hz.

For averaging times above 0.5 s or Fourier frequencies below 1 Hz, the laser instability could not be explained by the effects investigated so far. Thus, further investigations, especially at low Fourier frequencies, are of high interest to validate whether this laser system might be limited by noise resulting from unknown properties of $Al_{0.92}Ga_{0.08}As/GaAs$ mirrors or an unidentified noise source not connected to the mirror coatings. Unknown noise resulting from the mirror coatings could increase the instability reachable with $Al_{0.92}Ga_{0.08}As/GaAs$ mirrors, reducing their benefits compared to $Ta_2O_5/SiO_2$ mirrors.

Assuming that the predicted thermal noise of $Al_{0.92}Ga_{0.08}As/GaAs$ mirror coatings can be reached and is not degraded by so far unknown noise sources, silicon mirror substrates would reduce the thermal noise floor to $\mathrm{mod}\,\sigma_y \approx 4.4 \cdot 10^{-17}$. However,

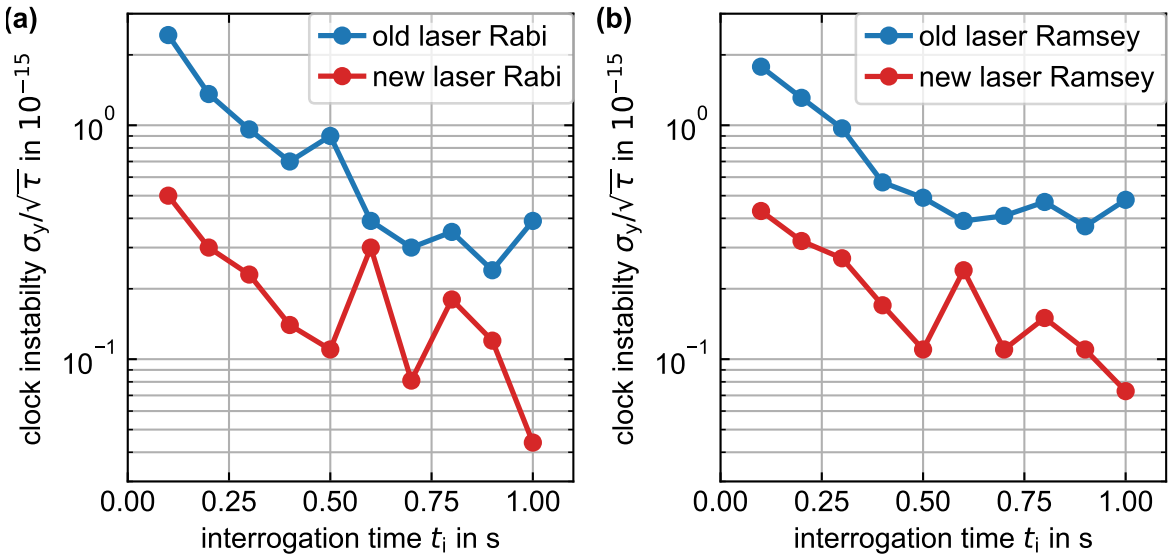


Figure 7.1.: Dick effect limit calculated using the equations in section 2.3 with $t_{\mathrm{dead}} = 0.5\,\mathrm{s}$, $t_{\pi/2} = 1\,\mathrm{ms}$ and the laser instabilities shown in figure 5.21.

silicon has an approximately four times higher coefficient of thermal expansion compared to FS glass at room temperature and thus the effect of mechanical stress in the cavity due to different CTEs and its compensation using an ULE ring have to be investigated. While silicon substrates are only suitable for wavelengths above 1100 nm, as its absorption increases significantly below this value, this would be no limitation for a Sr clock laser system operating at twice the transition wavelength of 1397 nm. Alternatively, meta mirrors as described by [139] are promising candidates to reduce the thermal noise caused by the mirrors. However, meta mirrors are currently still under fundamental investigation and have to reach sufficient reflectivity first in order to provide a serious alternative.

# A. Additional equations

The equations given in this section are taken from previous work and are repeated here only for completeness to clearly state, which equations are used in this work. The notation of the cited work is used, unless the variable was defined in the main text already. In this case the notation of this work is used. If variables form cited work are used, their definition is given.

## A.1. Pound-Drever-Hall error signal

The equations for the PDH error signal $\varepsilon_{\mathrm{PDH}}$ given here are taken from Black [41]. They are valid for fast modulation frequency $f_{\mathrm{m}} \gg lw$ and a small modulation depth $M < 1$.

$$\varepsilon_{\mathrm{PDH}} = -2\sqrt{P_{\mathrm{c}}P_{\mathrm{s}}}\Im\left[H(\nu)H^*(\nu + f_{\mathrm{m}}) - H^*(\nu)H(\nu - f_{\mathrm{m}})\right] \tag{A.1}$$

$$H(\nu) = \frac{E_{\mathrm{ref}}}{E_{\mathrm{inc}}} = \frac{\sqrt{R}\left[\exp\left(i\frac{2\pi\nu}{FSR}\right) - 1\right]}{1 - R\exp\left(i\frac{2\pi\nu}{FSR}\right)} \tag{A.2}$$

The reflection coefficient $H$ is defined by the ratio of the electric field of the reflected beam $E_{\mathrm{ref}}$ and the incident beam $E_{\mathrm{inc}}$ and is given here for a symmetric cavity with no losses. Note in the original equation the amplitude refection coefficient is used, which is equal to the square root of the intensity reflection coefficient $R$ used here.

## A.2. Thick coating correction factor

The thick coating correction factor $\Gamma_{\mathrm{tc}}$ as given by Evans et al. [103], with the average coating values as given in section A.3.

$$\Gamma_{\mathrm{tc}} = \frac{p_{\mathrm{E}}^2\Gamma_0 + p_{\mathrm{E}}p_{\mathrm{R}}\zeta\Gamma_1 + p_{\mathrm{R}}^2\zeta^2\Gamma_2}{R\zeta^2\Gamma_{\mathrm{D}}} \tag{A.3}$$

$$\Gamma_0 = 2[\sinh(\zeta) - \sin(\zeta)] + 2R[\cosh(\zeta) - \cos(\zeta)] \tag{A.4}$$

$$\Gamma_1 = 8\sin(\zeta/2)[R\cosh(\zeta/2) + \sinh(\zeta/2)] \tag{A.5}$$

$$\Gamma_2 = [1 + R^2]\sinh(\zeta) + [1 - R^2]\sin(\zeta) + 2R\cosh(\zeta) \tag{A.6}$$

$$\Gamma_{\mathrm{D}} = [1 + R^2]\cosh(\zeta) + [1 - R^2]\cos(\zeta) + 2R\sinh(\zeta) \tag{A.7}$$

with the power deposition fractions

$$p_{\mathrm{E}} = \frac{\Delta\bar{\alpha} d_{\mathrm{ct}}}{\Delta\bar{\alpha} d_{\mathrm{ct}} - \beta_{\mathrm{ct}}\lambda_0} \tag{A.8}$$

$$p_{\mathrm{R}} = \frac{-\beta_{\mathrm{ct}} d_{\mathrm{ct}}}{\Delta\bar{\alpha} d_{\mathrm{ct}} - \beta_{\mathrm{ct}}\lambda_0} \tag{A.9}$$

and with the effective coefficient of thermal expansion

$$\Delta\bar{\alpha} = \alpha_{\mathrm{ct}} - \alpha_{\mathrm{sb}}\frac{C_{\mathrm{ct}}}{C_{\mathrm{sb}}} \tag{A.10}$$

and with the scale factor

$$\xi = \frac{\sqrt{2} d_{\mathrm{ct}}}{l_{\mathrm{th,ct}}} \tag{A.11}$$

$$R = \frac{\kappa_{\mathrm{ct}} l_{\mathrm{th,sb}}}{\kappa_{\mathrm{sb}} l_{\mathrm{th,ct}}} \tag{A.12}$$

For $d_{\mathrm{ct}} \ll l_{\mathrm{th,ct}}$ ($l_{\mathrm{th}} = \sqrt{\kappa/[C\,2\pi\,f]}$), the correction factor simplifies to:

$$\Gamma_{\mathrm{tc}} \approx 1 + \frac{p_{\mathrm{E}}^2 + 3[p_{\mathrm{R}} - R^2]}{3R}\zeta - \frac{p_{\mathrm{E}} - 3[1 - R^2]}{6}\zeta^2 \tag{A.13}$$

For $d_{\mathrm{ct}} \gg l_{\mathrm{th,ct}}$, the correction factor simplifies to:

$$\Gamma_{\mathrm{tc}} \approx \frac{2p_{\mathrm{E}}^2}{R[1+R]\zeta^2} + \frac{p_{\mathrm{R}}^2}{R} \tag{A.14}$$

## A.3. Average coefficient values of the mirror coating

The equations given for the average values of the mirror coating properties are taken from Fejer et al. [112] with the nomenclature as used by Evans et al. [103]. The volume average of the CTE of a mirror consisting of layers of different materials is given by:

$$\alpha_{\mathrm{ct}} = \sum_{k=1}^{N_{\mathrm{k}}} \bar{\alpha_{\mathrm{k}}}\frac{d_{\mathrm{k}}}{d_{\mathrm{ct}}} \tag{A.15}$$

with the CTE for a given layer $k$ with thickness $d_{\mathrm{k}}$.

$$\bar{\alpha_{\mathrm{k}}} = \alpha_{\mathrm{k}}\frac{1+\eta_{\mathrm{sb}}}{1-\eta_{\mathrm{k}}}\left[\frac{1+\eta_{\mathrm{k}}}{1+\eta_{\mathrm{sb}}} + [1-2\eta_{\mathrm{sb}}]\frac{Y_{\mathrm{k}}}{Y_{\mathrm{sb}}}\right] \tag{A.16}$$

The average value of the heat capacity is given by:

$$C_{\mathrm{ct}} = \sum_{k=1}^{N_{\mathrm{k}}} C_{\mathrm{k}} \frac{d_{\mathrm{k}}}{d_{\mathrm{ct}}} \tag{A.17}$$

The average thermal conductivity is given by:

$$\kappa_{\mathrm{ct}} = \left[ \sum_{k=1}^{N_{\mathrm{k}}} \frac{1}{\kappa_{\mathrm{k}}} \frac{d_{\mathrm{k}}}{d_{\mathrm{ct}}} \right]^{-1} \tag{A.18}$$

To calculate, the effective thermorefractive index of the mirror coating the equation given by Evans et al. [103] for high reflectors with an halfwave cap layer is used in this work.

$$\beta_{\mathrm{ct}} = \frac{B_H + B_L}{4[n_{\mathrm{H}}^2 - n_{\mathrm{L}}^2]} \tag{A.19}$$

with the auxiliaary variable $B_k$ for a given layer k.

$$B_k = \beta_{\mathrm{k}} + \alpha_{\mathrm{k}} n_{\mathrm{k}} \frac{1 + \eta_{\mathrm{k}}}{1 - \eta_{\mathrm{k}}} \tag{A.20}$$

The average refractive index of the coating is given by:

$$n_{\mathrm{ct}} = \sum_{k=1}^{N_{\mathrm{k}}} n_{\mathrm{k}} \frac{1}{N_{\mathrm{k}}} \tag{A.21}$$

The coating thickness is given by equation A.22.

$$d_{\mathrm{ct}} = \frac{\lambda_0}{4 n_{\mathrm{H}}} N_{\mathrm{H}} + \frac{\lambda_0}{4 n_{\mathrm{L}}} N_{\mathrm{L}} \tag{A.22}$$

## A.4. Beam waist in a Fabry-Pérot cavity

The beam waist $w_1$ and $w_2$ at the two cavity mirrors are dependent on the mirrors' radius of curvature (ROC) $ROC_1$ and $ROC_2$, cavity length $l_0$, and the wavelength $\lambda_0$ [117].

$$w_1^2 = \frac{l_0 \lambda_0}{\pi} \sqrt{\frac{g_2}{g_1[1 - g_1 g_2]}} \tag{A.23}$$

$$w_2^2 = \frac{l_0 \lambda_0}{\pi} \sqrt{\frac{g_1}{g_2[1 - g_1 g_2]}} \tag{A.24}$$

with the stability parameter g

$$g_1 = 1 - \frac{l_0}{ROC_1} \tag{A.25}$$

$$g_2 = 1 - \frac{l_0}{ROC_2} \tag{A.26}$$

## A.5. Photothermal noise

The following equations are taken from Farsi et al. [122][1] and give the transfer function $\delta X_{\mathrm{PT}}$ between power fluctuations $\delta P_{\mathrm{abs}}$ and resulting optical cavity length fluctuations $\delta l$ including the PTE noise of the substrate $\delta X^{(\mathrm{sb})}_{\mathrm{PTE}}$, PTE noise of the coating $\delta X^{(\mathrm{ct})}_{\mathrm{PTE}}$ and PTR noise of the coating $\delta X^{(\mathrm{ct})}_{\mathrm{PTR}}$. As all three contributions are correlated $\delta X_{\mathrm{PT}}$ is the sum of the single contributions.

$$\delta X_{\mathrm{PT}} = 2\left[\delta X^{(\mathrm{sb})}_{\mathrm{PTE}} + \delta X^{(\mathrm{ct})}_{\mathrm{PTE}} + \delta X^{(\mathrm{ct})}_{\mathrm{PTR}}\right] \tag{A.27}$$

$$\delta X^{(\mathrm{sb})}_{\mathrm{PTE}} = -\frac{\alpha_{\mathrm{sb}}\left[1+\eta_{\mathrm{sb}}\right]}{\pi\kappa_{\mathrm{sb}}}\frac{f^{(\mathrm{sb})}_{\mathrm{T}}}{if}\int_0^\infty \xi \exp\left(-\frac{\xi^2}{\xi_{\mathrm{sb}}}\right)\delta P_{\mathrm{abs}} F\left[1-\frac{\xi}{\xi_{\mathrm{sb}}}\right]\mathrm{d}\xi \tag{A.28}$$

$$\begin{aligned}
\delta X^{(\mathrm{ct})}_{\mathrm{PTE}} = {} & \frac{\alpha_{\mathrm{ct}}}{\pi\kappa_{\mathrm{ct}}}\frac{f^{(\mathrm{ct})}_{\mathrm{T}}}{if}\int_0^\infty \xi \exp\left(-\frac{\xi^2}{\xi_{\mathrm{sb}}}\right)\delta P_{\mathrm{abs}} F \\
& \times\Bigg\{\gamma_1\Bigg[\cosh\left(\xi d_{\mathrm{ct}}\sqrt{2}/w\right) + R\frac{\xi}{\xi_{\mathrm{ct}}}\sinh\left(\xi d_{\mathrm{ct}}\sqrt{2}/w\right) \\
& - \cosh\left(\xi_{\mathrm{ct}} d_{\mathrm{ct}}\sqrt{2}/w\right) \quad - R\sinh\left(\xi_{\mathrm{ct}} d_{\mathrm{ct}}\sqrt{2}/w\right)\Bigg] \\
& - \gamma_1\frac{\xi}{\xi_{\mathrm{c}}}\Bigg[R\cosh\left(\xi d_{\mathrm{ct}}\sqrt{2}/w\right) + \frac{\xi_{\mathrm{ct}}}{\xi}\sinh\left(\xi d_{\mathrm{ct}}\sqrt{2}/w\right) \\
& - R\cosh\left(\xi_{\mathrm{ct}} d_{\mathrm{ct}}\sqrt{2}/w\right) - R\sinh\left(\xi_{\mathrm{ct}} d_{\mathrm{ct}}\sqrt{2}/w\right)\Bigg]\Bigg\}\mathrm{d}\xi
\end{aligned} \tag{A.29}$$

$$\begin{aligned}
\delta X^{(\mathrm{ct})}_{\mathrm{PTR}} = {} & \frac{\lambda_0\beta_{\mathrm{ct}}}{\sqrt{2}\pi\kappa_{\mathrm{ct}} w}\int_0^\infty \exp\left(-\frac{\xi^2}{\xi_{\mathrm{ct}}}\right)\delta P_{\mathrm{abs}}\frac{\xi}{\xi_{\mathrm{ct}}} \\
& \times\frac{\sinh(\xi_{\mathrm{ct}} d_{\mathrm{ct}}\sqrt{2}/w) + R\cosh(\xi_{\mathrm{ct}} d_{\mathrm{ct}}\sqrt{2}/w)}{\cosh(\xi_{\mathrm{ct}} d_{\mathrm{ct}}\sqrt{2}/w) + R\sinh(\xi_{\mathrm{ct}} d_{\mathrm{ct}}\sqrt{2}/w)}\mathrm{d}\xi
\end{aligned} \tag{A.30}$$

[1] Note that there is a misprint four lines after equation A4. It should be $\gamma_1 = \gamma_2 = 1$, which turned out in a private communication with Francesco Marin. Farsi et al. [122] uses the $1/\mathrm{e}$ definition for the spot size, while this work uses the $1/e^2$ definition, see chapter 3 footnote 8. Also the equations are given as functions of the angular frequency in Farsi et al. [122], while this work uses functions of $f$.

The filter $F$ and the reflection coefficient $R$ are defined as follows.

$$F = \frac{1}{\cosh(\xi_{\mathrm{ct}} d_{\mathrm{ct}} \sqrt{2}/w) + R \sinh(\xi_{\mathrm{ct}} d_{\mathrm{ct}} \sqrt{2}/w)} \tag{A.31}$$

$$R = \frac{\kappa_{\mathrm{ct}} \xi_{\mathrm{ct}}}{\kappa_{\mathrm{sb}} \xi_{\mathrm{sb}}} \tag{A.32}$$

The following coefficients serve to simplify the equation:

$$\xi_{\mathrm{ct}} = \sqrt{i \frac{f}{f_{\mathrm{T}}^{(\mathrm{ct})}} + \xi^2} \tag{A.33}$$

$$\xi_{\mathrm{sb}} = \sqrt{i \frac{f}{f_{\mathrm{T}}^{(\mathrm{sb})}} + \xi^2} \tag{A.34}$$

The cutoff frequency $f_{\mathrm{T}}^{(\mathrm{sb})}$ is defined equivalent to the TO noise, see section 3.2.

$$f_{\mathrm{T}}^{(\mathrm{ct})} = \frac{\kappa_{\mathrm{ct}}}{\pi w^2 C_{\mathrm{ct}}} \tag{A.35}$$

$$f_{\mathrm{T}}^{(\mathrm{sb})} = \frac{\kappa_{\mathrm{sb}}}{\pi w^2 C_{\mathrm{sb}}} \tag{A.36}$$

Other than for teh TE noise of the caoting, $\alpha_{\mathrm{ct}}$ is simply the average over $\alpha_{\mathrm{k}}$ for the PTE noise of the coating, as the correction for teh differnt mechanical properties of the coating and substrate is included in $\gamma_1$ already.

$$\alpha_{\mathrm{ct}} = \sum_{k=1}^{N_{\mathrm{k}}} \alpha_{\mathrm{k}} \frac{d_{\mathrm{k}}}{d_{\mathrm{ct}}} \tag{A.37}$$

# B. Material properties

Table B.1.: Material properties at 1397 nm and approximately 300 K.

| | ULE glass | FS glass (bulk)[f] | $SiO_2$ (layer)[f] | $Ta_2O_5$ | $Ta_2O_5$/ $SiO_2$ | $Al_{0.92}Ga_{0.08}As$ | GaAs | $Al_{0.92}Ga_{0.08}As$/ GaAs | silicon |
|---|---|---|---|---|---|---|---|---|---|
| $Y$ (GPa) | 67.6[a] | 72[c] | 72[c] | 144(42)[c] | - | 100[k] | 100[k] | - | 188[l] |
| $\eta$ | 0.17[a] | 0.17[c] | 0.17[c] | 0.23[c] | - | 0.32[k] | 0.32[k] | - | 0.26[l] |
| $\Phi$ $10^{-4}$ | 0.16[b] | 0.01[d] | 0.1-2[d] | 2-7[h] | 4[j] | - | - | 0.24[k] | $1 \cdot 10^{-4}$[l] |
| $C$ (MJ/[m$^3$K]) | 1.7[a] | 1.64[c] | 1.64[c] | 2.51[c] | - | 1.70[k] | 1.75[k] | - | 1630[l] |
| $\alpha$ ($10^-6$/K) | 0.00(3)[a] | 0.51[c] | 2.2[g] | 5.3[g] | - | 5.2[k] | 5.7[k] | - | 2[l] |
| $\kappa$ (W/[Km]) | 1.38[a] | 1.38[c] | 1.38[c] | - | 0.7[i] | 70[k] | 55[k] | - | 130[l] |
| $\beta_{ct}$ ($10^{-6}$ 1/K) | - | - | 5[g] | 64[g] | - | 179[k] | 366[k] | - | |
| $n$ | - | 1.46[e] | 1.46[e] | 2.05[e] | - | 2.96[e] | 3.39[e] | - | |

[a] Referring to company specifications at approximately 300 K
[b] Numata et al. [95]
[c] Values are taken from Fejer et al. [112] and Crooks et al. [140] and their references.
[d] Values between $3 \times 10^{-8}$ and $1 \times 10^{-6}$ [141] and $0.1 \times 10^{-4}$ and $2 \times 10^{-4}$ [142, 87, 140, 143] have been reported for bulk material and thin layers, respectively.
[e] Values derived from Adachi [144], Papatryfonos et al. [145], Malitson [146] and de Marcos et al. [147] for a wavelength of 1397 nm.
[f] FS glass refers to bulk material properties. $SiO_2$ refers to thin layer material properties, if available.
[g] Means of the values from Ogin [148] and his references. $\beta_{ct}$: $SiO_2$: values between $1.9 \times 10^{-6}$ and $8 \times 10^{-6}$, $Ta_2O_5$: values between $14 \times 10^{-6}$ and $121 \times 10^{-6}$, $\alpha$: $SiO_2$: values between $0.5 \times 10^{-6}$ and $5.4 \times 10^{-6}$, $Ta_2O_5$: values between $3.6 \times 10^{-6}$ and $8.9 \times 10^{-6}$
[h] Values between $2 \times 10^{-4}$ and $7 \times 10^{-4}$ have been reported [87, 142, 140, 143]
[i] The values form Crooks et al. [140] and Farsi et al. [122].
[j] Values between $2 \times 10^{-4}$ to $5 \times 10^{-4}$ have been reported [97, 142, 109, 87, 149].
[k] From Chalermsongsak et al. [111] and their references. For $Al_{0.92}Ga_{0.08}As$, most values are derived form GaAs and AlAs measurements.
[l] From Levinshtein et al. [150] and Hagemann [131] and their references.

# C. Engineering drawings

## C.1. Spacer

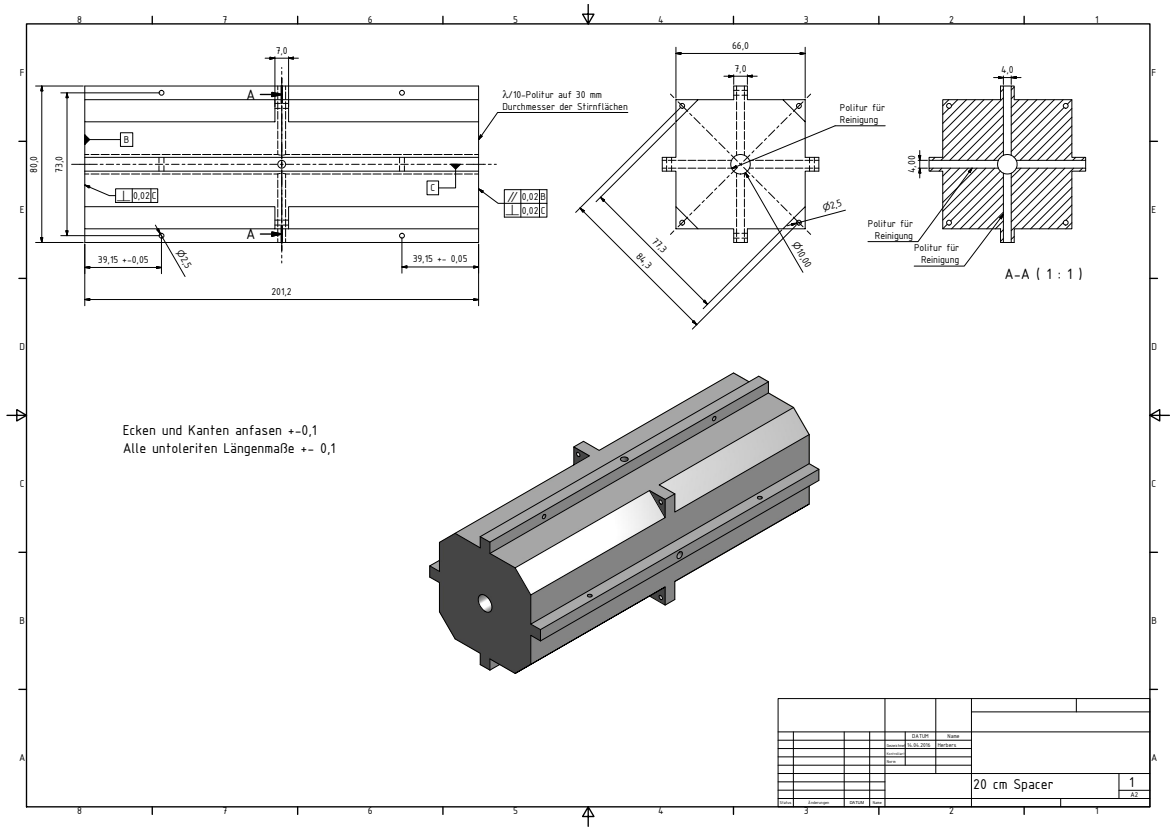


Figure C.1.: Engineering drawing of the cavity's spacer.

# Bibliography


[1] Gretchen K. Campbell, Andrew D. Ludlow, Sebastian Blatt, Jan W. Thomsen, Michael J. Martin, Marcio H. G. de Miranda, Tanya Zelevinsky, Martin M. Boyd, Jun Ye, Scott A. Diddams, Thomas P. Heavner, Thomas E. Parker, and Steven R. Jefferts. The absolute frequency of the $^{87}$Sr optical clock transition. *Metrologia*, 45:539–548, 2008.

[2] C. W. Chou, D. B. Hume, J. C. J. Koelemeij, D. J. Wineland, and T. Rosenband. Frequency comparison of two high-accuracy $Al^+$ optical clocks. *Phys. Rev. Lett.*, 104:070802, 2010.

[3] St. Falke, H. Schnatz, J. S. R. Vellore Winfred, Th. Middelmann, St. Vogt, S. Weyers, B. Lipphardt, G. Grosche, F. Riehle, U. Sterr, and Ch. Lisdat. The $^{87}$Sr optical frequency standard at PTB. *Metrologia*, 48:399–407, 2011.

[4] R. Le Targat, L. Lorini, Y. Le Coq, M. Zawada, J. Guéna, M. Abgrall, M. Gurov, P. Rosenbusch, D. G. Rovera, B. Nagórny, R. Gartman, P. G. Westergaard, M. E. Tobar, M. Lours, G. Santarelli, A. Clairon, S. Bize, P. Laurent, P. Lemonde, and J. Lodewyck. Experimental realization of an optical second with strontium lattice clocks. *Nature Commun.*, 4:2109, 2013.

[5] R. M. Godun, P. B. R. Nisbet-Jones, J. M. Jones, S. A. King, L. A. M. Johnson, H. S. Margolis, K. Szymaniec, S. N. Lea, K. Bongs, and P. Gill. Frequency ratio of two optical clock transitions in $^{171}Yb^+$ and constraints on the time-variation of fundamental constants. *Phys. Rev. Lett.*, 113:210801, Nov 2014.

[6] Christian Sanner, Nils Huntemann, Richard Lange, Christian Tamm, Ekkehard Peik, Marianna S. Safronova, and Sergey G. Porsev. Optical clock comparison test of Lorentz symmetry. *Nature*, 567:204–208, 2019.

[7] B. M. Roberts, P. Delva, A. Al-Masoudi, A. Amy-Klein, C. Bærentsen, C. F. A. Baynham, E. Benkler, S. Bilicki, W. Bowden, E. Cantin, E. A. Curtis, S. Dörscher, F. Frank, P. Gill, R. M. Godun, G. Grosche, A. Hees, I. R. Hill, R. Hobson, N. Huntemann, J. Kronjäger, S. Koke, A. Kuhl, R. Lange, T. Legero, B. Lipphardt, C. Lisdat, J. Lodewyck, O. Lopez, H. S. Margolis, H. Álvarez-Martínez, F. Meynadier, F. Ozimek, E. Peik, P.-E. Pottie, N. Quintin, R. Schwarz, C. Sanner, M. Schioppo, A. Silva, U. Sterr, Chr. Tamm, R. LeTargat, P. Tuckey, G. Vallet, T. Waterholter, D. Xu, and P. Wolf. Search for transient variations of the fine structure constant and dark matter using fiber-linked optical atomic clocks. *New J. Phys.*, 22:093010, Jul 2020.

[8] N. Huntemann, B. Lipphardt, Chr. Tamm, V. Gerginov, S. Weyers, and E. Peik. Improved limit on a temporal variation of $m_p/m_e$ from comparisons of $Yb^+$ and Cs atomic clocks. *Phys. Rev. Lett.*, 113:210802, 2014.

[9] W. F. McGrew, X. Zhang, H. Leopardi, R. J. Fasano, D. Nicolodi, K. Beloy, J. Yao, J. A. Sherman, S. A. Schäffer, J. Savory, R. C. Brown, S. Römisch, C. W. Oates, T. E. Parker, T. M. Fortier, and A. D. Ludlow. Towards the optical second: verifying optical clocks at the SI limit. *Optica*, 6(4):448–454, Apr 2019.

[10] P. Wcisło, P. Ablewski, K. Beloy, S. Bilicki, M. Bober, R. Brown, R. Fasano, R. Ciuryło, H. Hachisu, T. Ido, J. Lodewyck, A. Ludlow, W. McGrew, P. Morzyński, D. Nicolodi, M. Schioppo, M. Sekido, R. Le Targat, P. Wolf, X. Zhang, B. Zjawin, and M. Zawada. New bounds on dark matter coupling from a global network of optical atomic clocks. *Science Advances*, 4(12):eaau4869, 2018.

[11] R. Schwarz, S. Dörscher, A. Al-Masoudi, E. Benkler, T. Legero, U. Sterr, S. Weyers, J. Rahm, B. Lipphardt, and C. Lisdat. Long term measurement of the $^{87}Sr$ clock frequency at the limit of primary Cs clocks. *Phys. Rev. Research*, 2:033242, Aug 2020.

[12] Arne Bjerhammar. On a relativistic geodesy. *Bulletin Géodésique*, 59:207–220, 1985.

[13] Arne Bjerhammar. Relativistic geodesy. Technical Report Technical Report NOS 118 NGS 36, NOAA, 1986.

[14] M. Vermeer. *Chronometric Levelling*. Number 83:2 in Reports of the Finnish Geodetic Institute. Geodeettinen Laitos, Geodetiska Institutet, 1983. ISBN 9789517110877.

[15] Tanja Mehlstäubler, Gesine Grosche, Christian Lisdat, Piet Schmidt, and Heiner Denker. Atomic clocks for geodesy. *Rep. Prog. Phys.*, 81:064401, 2018.

[16] Heiner Denker. *Regional gravity field modeling: Theory and practical results.*, chapter 5, pages 185–291. 2013.

[17] Tobias Bothwell, Dhruv Kedar, Eric Oelker, John M. Robinson, Sarah L. Bromley, Weston L. Tew, Jun Ye, and Colin J. Kennedy. JILA SrI optical lattice clock with uncertainty of $2.0 \times 10^{-18}$. *Metrologia*, 56(6):065004, oct 2019.

[18] W. F. McGrew, X. Zhang, R. J. Fasano, S. A. Schäffer, K. Beloy, D. Nicolodi, R. C. Brown, N. Hinkley, G. Milan, M. Schioppo, T. H. Yoon, and A. D. Ludlow. Atomic clock performance beyond the geodetic limit. *Nature*, 564:87–90, Nov. 2018.

[19] T. L. Nicholson, S. L. Campbell, R. B. Hutson, G. E. Marti, B. J. Bloom, R. L. McNally, W. Zhang, M. D. Barrett, M. S. Safronova, G. F. Strouse, W. L. Tew, and J. Ye. Systematic evaluation of an atomic clock at $2\times10^{-18}$ total uncertainty. *Nature Commun.*, 6:6896, 2015.

[20] C. Lisdat, G. Grosche, N. Quintin, C. Shi, S.M.F. Raupach, C. Grebing, D. Nicolodi, F. Stefani, A. Al-Masoudi, S. Dörscher, S. Häfner, J.-L. Robyr, N. Chiodo, S. Bilicki, E. Bookjans, A. Koczwara, S. Koke, A. Kuhl, F. Wiotte, F. Meynadier, E. Camisard, M. Abgrall, M. Lours, T. Legero, H. Schnatz, U. Sterr, H. Denker, C. Chardonnet, Y. Le Coq, G. Santarelli, A. Amy-Klein, R. Le Targat, J. Lodewyck, O. Lopez, and P.-E. Pottie. A clock network for geodesy and fundamental science. *Nature Commun.*, 7:12443, 2016.

[21] Jacopo Grotti, Silvio Koller, Stefan Vogt, Sebastian Häfner, Uwe Sterr, Christian Lisdat, Heiner Denker, Christian Voigt, Ludger Timmen, Antoine Rolland, Fred N. Baynes, Helen S. Margolis, Michel Zampaolo, Pierre Thoumany, Marco Pizzocaro, Benjamin Rauf, Filippo Bregolin, Anna Tampellini, Piero Barbieri, Massimo Zucco, Giovanni A. Costanzo, Cecilia Clivati, Filippo Levi, and Davide Calonico. Geodesy and metrology with a transportable optical clock. *Nature Physics*, 14:437–441, 2018.

[22] Masao Takamoto, Ichiro Ushijima, Noriaki Ohmae, Toshihiro Yahagi, Kensuke Kokado, Hisaaki Shinkai, and Hidetoshi Katori. Test of general relativity by a pair of transportable optical lattice clocks. *Nature Photonics*, 14:411–415, 2020.

[23] Tetsushi Takano, Masao Takamoto, Ichiro Ushijima, Noriaki Ohmae, Tomoya Akatsuka, Atsushi Yamaguchi, Yuki Kuroishi, Hiroshi Munekane, Basara Miyahara, and Hidetoshi Katori. Geopotential measurements with synchronously linked optical lattice clocks. *Nature Photonics*, 10:662–666, 2016.

[24] Yao Huang, Huaqing Zhang, Baolin Zhang, Yanmei Hao, Hua Guan, Mengyan Zeng, Qunfeng Chen, Yige Lin, Yuzhuo Wang, Shiying Cao, Kun Liang, Fang Fang, Zhanjun Fang, Tianchu Li, and Kelin Gao. Geopotential measurement with a robust, transportable $Ca^+$ optical clock. *Phys. Rev. A*, 102:050802, Nov 2020.

[25] Pacôme Delva, Aurélien Hees, and Peter Wolf. Clocks in space for tests of fundamental physics. *Space Sci. Rev.*, 212:1385–1421, 2017.

[26] Josep Sanjuan, Klaus Abich, Martin Gohlke, Andreas Resch, Thilo Schuldt, Timm Wegehaupt, Geoffrey P. Barwood, Patrick Gill, and Claus Braxmaier. Long-term stable optical cavity for special relativity tests in space. *Opt. Express*, 27(25):36206–36220, Dec 2019. see erratum.

[27] J. Cao, P. Zhang, J. Shang, K. Cui, J. Yuan, S. Chao, S. Wang, H. Shu, and X. Huang. A compact, transportable single-ion optical clock with $7.8 \times 10^{-17}$ systematic uncertainty. *Appl. Phys. B*, 123(4):112, 2017. ISSN 1432-0649.

[28] S. B. Koller, J. Grotti, St. Vogt, A. Al-Masoudi, S. Dörscher, S. Häfner, U. Sterr, and Ch. Lisdat. Transportable optical lattice clock with $7 \times 10^{-17}$ uncertainty. *Phys. Rev. Lett.*, 118:073601, 2017.

[29] G. John Dick. Local oscillator induced instabilities in trapped ion frequency standards. In *Proceedings of* $19^{th}$ *Annu. Precise Time and Time Interval Meeting, Redendo Beach, 1987*, pages 133–147, Washington, DC, 1988. U.S. Naval Observatory.

[30] Audrey Quessada, Richard P. Kovacich, Irène Courtillot, André Clairon, Giorgio Santarelli, and Pierre Lemonde. The Dick effect for an optical frequency standard. *J. Opt. B: Quantum Semiclass. Opt.*, 5:S150–S154, 2003.

[31] W. M. Itano, J. C. Bergquist, J. J. Bollinger, J. M. Gilligan, D. J. Heinzen, F. L. Moore, M. G. Raizen, and D. J. Wineland. Quantum projection noise: Population fluctuations in two-level systems. *Phys. Rev. A*, 47:3554–3570, 1993. See Also: Erratum Phys. Rev. A 51, 1717 (1995).

[32] D. J. Wineland, J. J. Bollinger, W. M. Itano, F. L. Moore, and D. J. Heinzen. Spin squeezing and reduced quantum noise in spectroscopy. *Phys. Rev. A*, 46: R6797–R6800, 1992.

[33] Masahiro Kitagawa and Masahito Ueda. Squeezed spin states. *Phys. Rev. A*, 47:5138–5143, 1993.

[34] Boris Braverman, Akio Kawasaki, Edwin Pedrozo-Peñafiel, Simone Colombo, Chi Shu, Zeyang Li, Enrique Mendez, Megan Yamoah, Leonardo Salvi, Daisuke Akamatsu, Yanhong Xiao, and Vladan Vuletić. Near-unitary spin squeezing in $^{171}$Yb. *Phys. Rev. Lett.*, 122:223203, Jun 2019.

[35] I. Kruse, K. Lange, J. Peise, B. Lücke, L. Pezzé, J. Arlt, W. Ertmer, C. Lisdat, L. Santos, A. Smerzi, and C. Klempt. 0.75 atoms improve the clock signal of 10,000 atoms. *Proc. SPIE*, 10119:101190D–101190D–10, 2017.

[36] Marius Schulte, Christian Lisdat, Piet O. Schmidt, Uwe Sterr, and Klemens Hammerer. Prospects and challenges for squeezing-enhanced optical atomic clocks. *Nature Commun.*, 11:5955, 2020.

[37] M. Schioppo, R. C. Brown, W. F. McGrew, N. Hinkley, R. J. Fasano, K. Beloy, T. H. Yoon, G. Milani, D. Nicolodi, J. A. Sherman, N. B. Phillips, C. W. Oates, and A. D. Ludlow. Ultra-stable optical clock with two cold-atom ensembles. *Nature Photonics*, 11:48–52, 2017.

[38] David B. Hume and David R. Leibrandt. Probing beyond the laser coherence time in optical clock comparisons. *Phys. Rev. A*, 93:032138, Mar 2016.

[39] D. W. Allan. Statistics of atomic frequency standards. *Proc. IEEE*, 54:221–230, 1966.

[40] D. W. Allan. Should the classical variance be used as a basic measure in standards metrology? *IEEE Trans. Instrum. Meas.*, IM-36(2):646–654, June 1987.

[41] Eric D. Black. An introduction to Pound-Drever-Hall laser frequency stabilization. *Am. J. Phys.*, 69:79–87, 2001.

[42] Sana Amairi, Thomas Legero, Thomas Kessler, Uwe Sterr, Jannes B. Wübbena, Olaf Mandel, and Piet O. Schmidt. Reducing the effect of thermal noise in optical cavities. *Appl. Phys. B*, 113(2):233–242, 2013.

[43] Sebastian Häfner, Stephan Falke, Christian Grebing, Stefan Vogt, Thomas Legero, Mikko Merimaa, Christian Lisdat, and Uwe Sterr. $8 \times 10^{-17}$ fractional laser frequency instability with a long room-temperature cavity. *Opt. Lett.*, 40:2112–2115, 2015.

[44] D. G. Matei, T. Legero, S. Häfner, C. Grebing, R. Weyrich, W. Zhang, L. Sonderhouse, J. M. Robinson, J. Ye, F. Riehle, and U. Sterr. 1.5 $\mu$m lasers with sub-10 mHz linewidth. *Phys. Rev. Lett.*, 118:263202, 2017.

[45] John M. Robinson, Eric Oelker, William R. Milner, Wei Zhang, Thomas Legero, Dan G. Matei, Fritz Riehle, Uwe Sterr, and Jun Ye. Crystalline optical cavity at 4 K with thermal noise limited instability and ultralow drift. *Optica*, 6(2): 240–243, Feb 2019.

[46] Garrett D. Cole, Wei Zhang, Michael J. Martin, Jun Ye, and Markus Aspelmeyer. Tenfold reduction of Brownian noise in optical interferometry. *Nature Photonics*, 7:644–650, 2013.

[47] David R. Leibrandt, James C. Bergquist, and Till Rosenband. Cavity-stabilized laser with acceleration sensitivity below $10^{-12}$ g$^{-1}$. *Phys. Rev. A*, 87:023829, 2013.

[48] David R. Leibrandt, Michael J. Thorpe, Mark Notcutt, Robert E. Drullinger, Till Rosenband, and James C. Bergquist. Spherical reference cavities for frequency stabilization of lasers in non-laboratory environments. *Opt. Express*, 19(4):3471–3482, Feb 2011.

[49] Stephen Webster and Patrick Gill. Force-insensitive optical cavity. *Opt. Lett.*, 36:3572–3574, 2011.

[50] Xiaotong Chen, Yanyi Jiang, Bo Li, Hongfu Yu, Haifeng Jiang, Tao Wang, Yuan Yao, and Longsheng Ma. Laser frequency instability of $6 \times 10^{-16}$ using 10-cm-long cavities on a cubic spacer. *Chin. Opt. Lett.*, 18(3):030201, Mar 2020.

[51] Sebastian Häfner, Sofia Herbers, Stefan Vogt, Christian Lisdat, and Uwe Sterr. Transportable interrogation laser system with an instability of mod $\sigma_y = 3 \times 10^{-16}$. *Opt. Express*, 28(11):16407–16416, May 2020.

[52] J. Davila-Rodriguez, F. N. Baynes, A. D. Ludlow, T. M. Fortier, H. Leopardi, S. A. Diddams, and F. Quinlan. Compact, thermal-noise-limited reference cavity for ultra-low-noise microwave generation. *Opt. Lett.*, 42(7):1277–1280, Apr 2017.

[53] Dariusz Świerad, Sebastian Häfner, Stefan Vogt, Bertrand Venon, David Holleville, Sébastien Bize, André Kulosa, Sebastian Bode, Yeshpal Singh, Kai Bongs, Ernst Maria Rasel, Jérôme Lodewyck, Rodolphe Le Targat, Christian Lisdat, and Uwe Sterr. Ultra-stable clock laser system development towards space applications. *Scientific Reports*, 6:33973, 2016.

[54] Qun-Feng Chen, Alexander Nevsky, Marco Cardace, Stephan Schiller, Thomas Legero, Sebastian Häfner, Andre Uhde, and Uwe Sterr. A compact, robust, and transportable ultra-stable laser with a fractional frequency instability of $1 \times 10^{-15}$. *Rev. Sci. Instrum.*, 85:113107, 2014.

[55] B. Argence, E. Prevost, T. Lévèque, R. Le Goff, S. Bize, P. Lemonde, and G. Santarelli. Prototype of an ultra-stable optical cavity for space applications. *Opt. Express*, 20(23):25409–25420, 2012.

[56] Alexandre Didier, Jacques Millo, Baptiste Marechal, Cyrus Rocher, Enrico Rubiola, Roméo Lecomte, Morvan Ouisse, Jérôme Delporte, Clément Lacroûte, and Yann Kersalé. Ultracompact reference ultralow expansion glass cavity. *Appl. Opt.*, 57(22):6470–6473, Aug 2018.

[57] E. Oelker, R. B. Hutson, C. J. Kennedy, L. Sonderhouse, T. Bothwell, A. Goban, D. Kedar, C. Sanner, J. M. Robinson, G. E. Marti, D. G. Matei, T. Legero, M. Giunta, R. Holzwarth, F. Riehle, U. Sterr, and J. Ye. Demonstration of $4.8 \times 10^{-17}$ stability at 1 s for two independent optical clocks. *Nature Photonics*, 13:714–719, 2019.

[58] Ali Al-Masoudi, Sören Dörscher, Sebastian Häfner, Uwe Sterr, and Christian Lisdat. Noise and instability of an optical lattice clock. *Phys. Rev. A*, 92: 063814, 2015.

[59] Ian D. Leroux, Nils Scharnhorst, Stephan Hannig, Johannes Kramer, Lennart Pelzer, Mariia Stepanova, and Piet O. Schmidt. On-line estimation of local oscillator noise and optimisation of servo parameters in atomic clocks. *Metrologia*, 54:307–321, 2017.

[60] Richard Hobson. *An optical lattice clock with neutral strontium.* PhD thesis, Balliol College, University of Oxford, 2016.

[61] G. J. Dick, J. Prestage, C. Greenhall, and L. Maleki. Local oscillator induced degradation of medium-term stability in passive atomic frequency standards. In *Proceedings of the 22nd Annual Precise Time and Time Interval (PTTI) Applications and Planning Meeting, Vienna VA, USA*, pages 487–509, 1990.

[62] Erik Benkler, Christian Lisdat, and Uwe Sterr. On the relation between uncertainties of weighted frequency averages and the various types of allan deviations. *Metrologia*, 52:565, 2015.

[63] Giorgio Santarelli, Claude Audoin, Ala'a Makdissi, Philippe Laurent, G. John Dick, and André Clairon. Frequency stability degradation of an oscillator slaved to a periodically interrogated atomic resonator. *IEEE Trans. Ultrason. Ferroelectr. Freq. Control*, 45:887–894, 1998.

[64] C. Audoin, G. Santarelli, A. Makdissi, and A. Clairon. Properties of an oscillator slaved to a periodically interrogated atomic resonator. *IEEE Trans. Ultrason. Ferroelectr. Freq. Control*, 45:877, 1998.

[65] Charles A. Greenhall. A derivation of the long-term degradation of a pulsed atomic frequency standard from a control-loop model. *IEEE Trans. Ultrason. Ferroelectr. Freq. Control*, 45:895–898, 1998.

[66] R. W. P. Drever, J. L. Hall, F. V. Kowalski, J. Hough, G. M. Ford, A. J. Munley, and H. Ward. Laser phase and frequency stabilization using an optical resonator. *Appl. Phys. B*, 31:97–105, 1983.

[67] J. Helmcke, D. Zevgolis, and B. Ü. Yen. Observation of high contrast, ultra narrow optical Ramsey fringes in saturated absorption utilizing four interaction zones of travelling waves. *Appl. Phys. B*, 28:83–84, 1982.

[68] A. White. Frequency stabilization of gas lasers. *IEEE Journal of Quantum Electronics*, 1(8):349–357, 1965.

[69] T. W. Hänsch and B. Couillaud. Laser frequency stabilization by polarization spectroscopy of a reflecting reference cavity. *Opt. Commun.*, 35:441–444, 1980.

[70] Yu V. Troitskii. Optimization and comparison of the characteristics of optical interference discriminators. *Sov. J. Quantum Electron.*, 8:628–631, 1978.

[71] R. V. Pound. Electronic frequency stabilization of microwave oscillators. *Rev. Sci. Instrum.*, 17:490–505, 1946.

[72] Fritz Riehle and Jürgen Helmcke. Optical frequency standards based on neutral atoms and molecules. In A. N. Luiten, editor, *Frequency Measurement and Control*, volume 79 of *Topics in Applied Physics*, pages 95–129. Springer, Berlin, Heidelberg, New York, 2001.

[73] Fritz Riehle. *Frequency Standards: Basics and Applications*. Wiley-VCH, Weinheim, 2004.

[74] Hui Shen, Liufeng Li, Jin Bi, Jia Wang, and Lisheng Chen. Systematic and quantitative analysis of residual amplitude modulation in Pound-Drever-Hall frequency stabilization. *Phys. Rev. A*, 92:063809, Dec 2015.

[75] G. C. Bjorklund. Frequency-modulation spectroscopy: a new method for measuring weak absorptions and dispersions. *Opt. Lett.*, 5:15–17, 1980.

[76] J. L. Hall, L. Hollberg, T. Baer, and H. G. Robinson. Optical heterodyne saturation spectroscopy. *Appl. Phys. Lett.*, 39:680–682, 1981.

[77] N. C. Wong and J. L. Hall. Servo control of amplitude modulation in frequency-modulation spectroscopy: demonstration of shot-noise-limited detection. *J. Opt. Soc. Am. B*, 2:1527–1533, 1985.

[78] W. Zhang, M. J. Martin, C. Benko, J. L. Hall, J. Ye, C. Hagemann, T. Legero, U. Sterr, F. Riehle, G. D. Cole, and M. Aspelmeyer. Reduction of residual amplitude modulation to $1 \times 10^{-6}$ for frequency-modulation and laser stabilization. *Opt. Lett.*, 39:1980–1983, 2014.

[79] Xiaohui Shi, Jie Zhang, Xiaoyi Zeng, Xiaolong Lü, Kui Liu, Jing Xi, Yanxia Ye, and Zehuang Lu. Suppression of residual amplitude modulation effects in Pound-Drever-Hall locking. *Appl. Phys. B*, 124:153, 2018.

[80] Jin Bi, Yunlin Zhi, Liufeng Li, and Lisheng Chen. Suppressing residual amplitude modulation to the $10^{-7}$ level in optical phase modulation. *Appl. Opt.*, 58 (3):690–694, Jan 2019.

[81] Zhixiu Li, Yuhang Tian, Yajun Wang, Weiguang Ma, and Yaohui Zheng. Residual amplitude modulation and its mitigation in wedged electro-optic modulator. *Opt. Express*, 27(5):7064–7071, Mar 2019.

[82] Zhaoyang Tai, Lulu Yan, Yanyan Zhang, Xiaofei Zhang, Wenge Guo, Shougang Zhang, and Haifeng Jiang. Electro-optic modulator with ultra-low residual amplitude modulation for frequency modulation and laser stabilization. *Opt. Lett.*, 41(23):5584–5587, Dec 2016.

[83] Li Jin. Suppression of residual amplitude modulation of ADP electro-optical modulator in Pound-Drever-Hall laser frequency stabilization. *Opti. Laser Technol.*, 136:106758, 2021. ISSN 0030-3992.

[84] Liufeng Li, Fang Liu, Chun Wang, and Lisheng Chen. Measurement and control of residual amplitude modulation in optical phase modulation. *Rev. Sci. Instrum.*, 83:043111, 2012.

[85] J. L. Hall, W. Zhang, and J. Ye. Accurate removal of RAM from FM laser beams. In *2015 Joint Conference of the IEEE International Frequency Control Symposium the European Frequency and Time Forum*, pages 713–716, 2015.

[86] John F. Diehl, Christopher E. Sunderman, Joseph M. Singley, Vincent J. Urick, and Keith J. Williams. Control of residual amplitude modulation in lithium niobate phase modulators. *Opt. Express*, 25(26):32985–32994, Dec 2017.

[87] Tara Chalermsongsak, Frank Seifert, Evan D. Hall, Koji Arai, Eric K. Gustafson, and Rana X. Adhikari. Broadband measurement of coating thermal noise in rigid Fabry-Pérot cavities. *Metrologia*, 52:17–30, 2015.

[88] Michael L. Gorodetsky. Thermal noises and noise compensation in high-reflection multilayer coating. *Phys. Lett. A*, 372:6813–6822, 2008.

[89] Michael J. Martin. *Quantum Metrology and Many-Body Physics: Pushing the Frontier of the Optical Lattice Clock*. PhD thesis, University of Colorado, 2013.

[90] Herbert B. Callen and Theodore A. Welton. Irreversibility and generalized noise. *Phys. Rev.*, 83(1):34–40, 1951.

[91] Herbert B. Callen and Richard F. Greene. On a theorem of irreversible thermodynamics. *Phys. Rev.*, 86:702–710, 1952.

[92] Yu. Levin. Internal thermal noise in the LIGO test masses: A direct approach. *Phys. Rev. D*, 57:659–663, 1998.

[93] Yuk Tung Liu and Kip S. Thorne. Thermoelastic noise and homogeneous thermal noise in finite sized gravitational-wave test masses. *Phys. Rev. D*, 62:122002, 2000.

[94] François Bondu, Patrice Hello, and Jean-Yves Vinet. Thermal noise in mirrors of interferometric gravitational wave antennas. *Phys. Lett. A*, 246:227–236, 1998.

[95] Kenji Numata, Amy Kemery, and Jordan Camp. Thermal-noise limit in the frequency stabilization of lasers with rigid cavities. *Phys. Rev. Lett.*, 93:250602, 2004.

[96] T. Kessler, T. Legero, and U. Sterr. Thermal noise in optical cavities revisited. *J. Opt. Soc. Am. B*, 29:178–184, 2012.

[97] Gregory M. Harry, Andri M. Gretarsson, Peter R. Saulson, Scott E. Kittelberger, Steven D. Penn, William J. Startin, Sheila Rowan, Martin M. Fejer, D. R. M. Crooks, Gianpietro Cagnoli, Jim Hough, and Norio Nakagawa. Thermal noise in interferometric gravitational wave detectors due to dielectric optical coatings. *Class. Quantum Grav.*, 19:897–917, 2002.

[98] N. Nakagawa, A. M. Gretarsson, E. K. Gustafson, and M. M. Fejer. Thermal noise in half-infinite mirrors with nonuniform loss: A slab of excess loss in a half-infinite mirror. *Phys. Rev. D*, 65:102001, 2002.

[99] V. B. Braginsky, M. L. Gorodetsky, and S. P. Vyatchanin. Thermodynamical fluctuations and photo-thermal shot noise in gravitational wave antennae. *Phys. Lett. A*, 264:1–10, 1999.

[100] Tara Chalermsongsak. *High fidelity probe and mitigation of mirror thermal fluctuations*. PhD thesis, California Institute of Technology, 2014.

[101] D. Heinert, A. G. Gurkovsky, R. Nawrodt, S. P. Vyatchanin, and K. Yamamoto. Thermorefractive noise of finite-sized cylindrical test masses. *Phys. Rev. D*, 84: 062001, 2011.

[102] H. J. Kimble, Benjamin L. Lev, and Jun Ye. Optical interferometers with reduced sensitivity to thermal noise. *Phys. Rev. Lett.*, 101:260602, 2008.

[103] M. Evans, S. Ballmer, M. Fejer, P. Fritschel, G. Harry, and G. Ogin. Thermooptic noise in coated mirrors for high-precision optical measurements. *Phys. Rev. D*, 78:102003, 2008.

[104] V. B. Braginsky, M. L. Gorodetsky, and S. P. Vyatchanin. Thermo-refractive noise in gravitational wave antennae. *Phys. Lett. A*, 271:303–307, 2000.

[105] V. B. Braginsky and S. P. Vyatchanin. Thermodynamical fluctuations in optical mirror coatings. *Phys. Lett. A*, 312:244–255, 2003.

[106] M. Cerdonio, L. Conti, A. Heidmann, and M. Pinard. Thermoelastic effects at low temperatures and quantum limits in displacement measurements. *Phys. Rev. D*, 63:082003, Mar 2001.

[107] Eric D. Black, Akira Villar, Kyle Barbary, Adam Bushmaker, Jay Heefner, Seiji Kawamura, Fumiko Kawazoe, Luca Matone, Sharon Meidt, Shanti R. Rao, Kevin Schulz, Michael Zhang, and Kenneth G. Libbrecht. Direct observation of broadband coating thermal noise in a suspended interferometer. *Phys. Lett. A*, 328:1–5, 2004.

[108] K.S. Chan, M. Siercke, C. Hufnagel, and R. Dumke. Adsorbate electric fields on a cryogenic atom chip. *Phys. Rev. Lett.*, 112:026101, 2014.

[109] Kenji Numata, Masaki Ando, Kazuhiro Yamamoto, Shigemi Otsuka, and Kimio Tsubono. Wide-band direct measurement of thermal fluctuations in an interferometer. *Phys. Rev. Lett.*, 26:260602, 2003.

[110] Eric D. Black, Akira Villar, and Kenneth G. Libbrecht. Thermoelastic-damping noise from sapphire mirrors in a fundamental-noise-limited interferometer. *Phys. Rev. Lett.*, 93:241101, Dec 2004.

[111] Tara Chalermsongsak, Evan D Hall, Garrett D Cole, David Follman, Frank Seifert, Koji Arai, Eric K Gustafson, Joshua R Smith, Markus Aspelmeyer, and Rana X Adhikari. Coherent cancellation of photothermal noise in $GaAs/Al_{0.92}Ga_{0.08}As$ Bragg mirrors. *Metrologia*, 53(2):860, 2016.

[112] M. M. Fejer, S. Rowan, G. Cagnoli, D. R. M. Crooks, A. Gretarsson, G. M. Harry, J. Hough, S. D. Penn, P. H. Sneddon, and S. P. Vyatchanin. Thermoelastic dissipation in inhomogeneous media: loss measurements and displacement noise in coated test masses for interferometric gravitational wave detectors. *Phys. Rev. D*, 70:082003, 2004.

[113] Thomas Legero, Thomas Kessler, and Uwe Sterr. Tuning the thermal expansion properties of optical reference cavities with fused silica mirrors. *J. Opt. Soc. Am. B*, 27:914–919, 2010.

[114] Jun Ye, Jin-Long Peng, R. Jason Jones, Kevin W. Holman, John L. Hall, David J. Jones, Scott A. Diddams, John Kitching, Sebastien Bize, James C. Bergquist, Leo W. Hollberg, Lennart Robertsson, and Long-Sheng Ma. Delivery of high-stability optical and microwave frequency standards over an optical fiber network. *J. Opt. Soc. Am. B*, 20:1459–1467, 2003.

[115] S. Hannig, L. Pelzer, N. Scharnhorst, J. Kramer, M. Stepanova, Z. T. Xu, N. Spethmann, I. D. Leroux, T. E. Mehlstäubler, and P. O. Schmidt. Towards a transportable aluminium ion quantum logic optical clock. arXiv:1902.08701 [physics.atom-ph], Feb 2019.

[116] Eileen Annika Klocke. Design und Charakterisierung eines Breadboards zur Laserfrequenzverteilung mit relativen Instabilitaten von unter $10^{-16}$ in einer transportablen optischen Uhr. Master's thesis, Gottfried Wilhelm Leibniz Universität Hannover, 2020.

[117] Anthony E. Siegman. *Lasers*. University Science Books, Mill Valley, California, 1986.

[118] D. I. Babic and S. W. Corzine. Analytic expressions for the reflection delay, penetration depth, and absorptance of quarter-wave dielectric mirrors. *IEEE J. Quantum Electron.*, 28(2):514–524, Feb 1992. ISSN 0018-9197.

[119] Garrett D. Cole, Wei Zhang, Bryce J. Bjork, David Follman, Paula Heu, Christoph Deutsch, Lindsay Sonderhouse, John Robinson, Chris Franz, Alexei Alexandrovski, Mark Notcutt, Oliver H. Heckl, Jun Ye, and Markus Aspelmeyer. High-performance near- and mid-infrared crystalline coatings. *Optica*, 3:647–656, 2016.

[120] J. T. Milek and M. Neuberger. *Ammonium Dihydrogen Phosphate (ADP)*, pages 23–52. Springer US, Boston, MA, 1972. ISBN 978-1-4684-6168-8.

[121] Sebastian Häfner. *Ultrastabile Lasersysteme für Weltraum- und Boden-Anwendungen*. PhD thesis, Leibniz Universität Hannover, 2015.

[122] Alessandro Farsi, Mario Siciliani de Cumis, Francesco Marino, and Francesco Marin. Photothermal and thermo-refractive effects in high reflectivity mirrors at room and cryogenic temperature. *J. Appl. Phys.*, 111(4):043101, 2012.

[123] M. De Rosa, F. Marin, F. Marino, O. Arcizet, A. Heidmann, and M. Pinard. Experimental investigation of dynamic photo-thermal effect. *Class. Quantum Grav.*, 23(8):S259, 2006.

[124] Zilong Chen, Justin G. Bohnet, Joshua M. Weiner, Kevin C. Cox, and James K. Thompson. Cavity-aided nondemolition measurements for atom counting and spin squeezing. *Phys. Rev. A*, 89:043837, 2014.

[125] T. Nazarova, F. Riehle, and U. Sterr. Vibration-insensitive reference cavity for an ultra-narrow-linewidth laser. *Appl. Phys. B*, 83:531–536, 2006.

[126] D. C. Williams. The parallelism of a length bar with an end load. *J. Sci. Instrum.*, 39:608–610, 1962.

[127] B. Edlén. The refractive index of air. *Metrologia*, 2:71–80, 1966.

[128] K. P. Birch and M. J. Downs. An updated Edlén equation for the refractive index of air. *Metrologia*, 30:155–162, 1993.

[129] K P Birch and M J Downs. Correction to the updated Edlén equation for the refractive index of air. *Metrologia*, 31:315–316, 1994.

[130] Karl Jousten. *Handbuch Vakuumtechnik, Living reference work, Springer eBook Collection, Springer Reference Technik*. Springer;, Wiesbaden, 2018. ISBN 9783658134037.

[131] Christian Hagemann. *Ultra-stable laser based on a cryogenic single-crystal silicon cavity*. PhD thesis, Fakultät für Mathematik und Physik der Gottfried Wilhelm Leibniz Universität Hannover, 2013.

[132] Uwe Sterr and Christian Lisdat. A sharper laser. *Nature Physics*, 5:382–383, 2009.

[133] Isao Ito, Alissa Silva, Takuma Nakamura, and Yohei Kobayashi. Stable CW laser based on low thermal expansion ceramic cavity with 4.9 mHz/s frequency drift. *Opt. Express*, 25(21):26020–26028, Oct 2017.

[134] Jialiang Yu, Thomas Legero, Fritz Riehle, Daniele Nicolodi, Kedar Dhruv, John M. Robinson, Eric Oelker, Jun Ye, and Uwe Sterr. Frequency stability of a cryogenic silicon resonator with crystalline mirror coatings. *Joint Conference of the European Frequency and Time Forum and the IEEE International Frequency Control Symposium*, 7.-17. July 2021.

[135] Sofia Herbers, Sören Dörscher, Erik Benkler, and Christian Lisdat. Phase noise of frequency doublers in optical clock lasers. *Opt. Express*, 27(16):23262–23273, Aug 2019.

[136] Richard L. Sutherland. *Handbook of Nonlinear Optics*. Marcel Dekker, 2 edition, 2003. ISBN 0-8247-4243-5.

[137] D. Yeaton-Massey and R. X. Adhikari. A new bound on excess frequency noise in second harmonic generation in PPKTP at the $10^{-19}$ level. *Opt. Express*, 20: 21019–21024, 2012.

[138] S. M. Brewer, J.-S. Chen, A. M. Hankin, E. R. Clements, C. W. Chou, D. J. Wineland, D. B. Hume, and D. R. Leibrandt. $^{27}Al^{+}$ quantum-logic clock with a systematic uncertainty below $10^{-18}$. *Phys. Rev. Lett.*, 123:033201, 2019.

[139] Johannes Dickmann and Stefanie Kroker. Highly reflective low-noise etalon-based meta-mirror. *Phys. Rev. D*, 98:082003, Oct 2018.

[140] D R M Crooks, G Cagnoli, M M Fejer, G Harry, J Hough, B T Khuri-Yakub, S Penn, R Route, S Rowan, P H Sneddon, I O Wygant, and G G Yaralioglu. Experimental measurements of mechanical dissipation associated with dielectric coatings formed using $SiO_2$, $Ta_2O_5$ and $Al_2O_3$. *Class. Quantum Grav.*, 23:4953–4965, 2006.

[141] Kenji Numata, Kazuhiro Yamamoto, Hidehiko Ishimoto, Shigemi Otsuka, Keita Kawabe, Masaki Ando, and Kimio Tsubono. Systematic measurement of the intrinsic losses in various kinds of bulk fused silica. *Phys. Lett. A*, 327(4):263–271, 2004.

[142] Steven D Penn, Peter H Sneddon, Helena Armandula, Joseph C Betzwieser, Gianpietro Cagnoli, Jordan Camp, D R M Crooks, Martin M Fejer, Andri M Gretarsson, Gregory M Harry, Jim Hough, Scott E Kittelberger, Michael J Mortonson, Roger Route, Sheila Rowan, and Christophoros C Vassiliou. Mechanical loss in tantala/silica dielectric mirror coatings. *Class. Quantum Grav.*, 20(13): 2917, 2003.

[143] Tianjun Li, Felipe A. Aguilar Sandoval, Mickael Geitner, Ludovic Bellon, Gianpietro Cagnoli, Jérôme Degallaix, Vincent Dolique, Raffaele Flaminio, Danièle Forest, Massimo Granata, Christophe Michel, Nazario Morgado, and Laurent Pinard. Measurements of mechanical thermal noise and energy dissipation in optical dielectric coatings. *Phys. Rev. D*, 89:092004, May 2014.

[144] S. Adachi. Optical dispersion relations for GaP, GaAs, GaSb, InP, InAs, InSb, $Al_xGa_{1-x}As$, and $In_{1-x}Ga_xAs_yP_{1-y}$. *Journal of Applied Physics*, 66(12):6030–6040, 1989.

[145] Konstantinos Papatryfonos, Todora Angelova, Antoine Brimont, Barry Reid, Stefan Guldin, Peter Raymond Smith, Mingchu Tang, Keshuang Li, Alwyn J. Seeds, Huiyun Liu, and David R. Selviah. Refractive indices of mbe-grown alxga(1-x)as ternary alloys in the transparent wavelength region. *AIP Advances*, 11(2):025327, 2021.

[146] I. H. Malitson. Interspecimen comparison of the refractive index of fused silica. *J. Opt. Soc. Am.*, 55:1205–1209, 1965.

[147] Luis V. Rodríguez de Marcos, Juan I. Larruquert, José A. Méndez, and José A. Aznárez. Self-consistent optical constants of sio2 and ta2o5 films. *Opt. Mater. Express*, 6(11):3622–3637, Nov 2016.

[148] Gregory H. Ogin. *Measurement of Thermo-Optic Properties of Thin Film Dielectric Coatings*. PhD thesis, California Institute of Technology, 2013.

[149] Gregory M. Harry, Helena Armandula, Eric Black, D. R. M. Crooks, Gianpietro Cagnoli, Jim Hough, Peter Murray, Stuart Reid, Sheila Rowan, Peter Sneddon, Martin M. Fejer, Roger Route, and Steven D. Penn. Thermal noise from optical coatings in gravitational wave detectors. *Appl. Opt.*, 45:1569–1574, 2006.

[150] M Levinshtein, S Rumyantsev, and M Shur. *Handbook Series on Semiconductor Parameters*. WORLD SCIENTIFIC, 1996.

[151] Stefano Origlia, Mysore Srinivas Pramod, Stephan Schiller, Yeshpal Singh, Kai Bongs, Roman Schwarz, Ali Al-Masoudi, Sören Dörscher, Sofia Herbers, Sebastian Häfner, Uwe Sterr, and Christian Lisdat. Towards an optical clock for space: Compact, high-performance optical lattice clock based on bosonic atoms. *Phys. Rev. A*, 98:053443, 2018.

# Symbols

| Symbol | Unit | Description |
|---|---|---|
| $A$ | $\mathrm{m}^2$ | area |
| $b(t)$ | | sensitivity function |
| $C$ | $\frac{\mathrm{J}}{\mathrm{m}^3\mathrm{K}}$ | heat capacity per volume |
| $c$ | $\frac{\mathrm{m}}{\mathrm{s}}$ | velocitiy of light |
| $D$ | | error-signal disciminant |
| $d$ | m | thickness, height |
| $E$ | $\frac{\mathrm{V}}{\mathrm{m}}$ | electric field |
| $F$ | N | force |
| $f$ | Hz | (Fourier/radio) frequency |
| $FSR$ | Hz | free spectral range of an optical resonator |
| $g$ | | stability parameter of a resonator |
| $g_0$ | | gravitational acceleration |
| $H$ | N | reflection coefficient for a symmetric cavity with no losses |
| $h$ | Js | Plank constant |
| $I$ | A | current |
| $J$ | | integrals of different kind |
| $K$ | $\frac{\mathrm{m}^3}{\mathrm{s}}$ | conductivity |
| $k$ | | postive integer |
| $k_\mathrm{B}$ | $\frac{\mathrm{J}}{\mathrm{K}}$ | Boltzmann constant |
| $l$ | m | length |
| $\Delta l$ | m | difference in length |
| $\delta l$ | m | length fluctuations |
| $l_\mathrm{th}$ | m | thermal diffusion length |
| $lw$ | Hz | cavity linewidth |

| Symbol | Unit | Description |
|---|---|---|
| $M$ | | modulation depth |
| $N$ | | number/amount of something |
| $n$ | | refractive index |
| $\delta n$ | | refractive index variations |
| $\Delta n$ | | birefringence |
| $P$ | W | optical power |
| $\delta P$ | W | optical power |
| $p$ | Pa | pressure |
| $\Delta p$ | Pa | pressure difference |
| $\delta p$ | Pa | pressure variations |
| $Q_\mathrm{e}$ | | excitation probability |
| $q_\mathrm{pV}$ | $\frac{\mathrm{Pam^3}}{\mathrm{s}}$ | throughput |
| $R$ | | intensity refelction coefficient |
| $r$ | m | radius |
| $ROC$ | m | mirror's radius of curvature |
| $S_\mathrm{T}$ | $\frac{\mathrm{K^2}}{\mathrm{Hz}}$ | power spectral density of fluctuations of the average temperature |
| $S_\mathrm{x}$ | $\frac{\mathrm{m^2}}{\mathrm{Hz}}$ | power spectral density of length fluctuation |
| $S_\mathrm{y}$ | $\frac{1}{\mathrm{Hz}}$ | power spectral density of fractional frequency fluctuation |
| $s$ | $\frac{\mathrm{m^3}}{\mathrm{s}}$ | pumping speed |
| $T$ | K | temperature |
| $\Delta T$ | K | temperature difference |
| $t$ | s | time/duration |
| $U$ | V | voltage |
| $\vec{u}$ | m | displacement field |
| $\Delta V$ | $\frac{\mathrm{m^4}}{\mathrm{s^2}}$ | gravity potential difference |
| $W_0$ | J | maximum elastic strain energy |
| $X$ | m | Fourier transformed of the displacement |
| $\delta X$ | m | variatons of the Fourier transformed of the displacement |
| $x$ | m | Cartesian coordinate |

| Symbol | Unit | Description |
|---|---|---|
| $Y$ | Pa | Young's modulus |
| $y$ | m | Cartesian coordinate |
| $z$ | m | Cartesian coordinate |
| $\alpha$ | $\frac{1}{\mathrm{K}}$ | cofficient of thermal expansion |
| $\beta$ | | effective thermorefractive index |
| $\Gamma_{\mathrm{tc}}$ | 1/K | thick coating correction |
| $\epsilon_{\mathrm{x},0}$ | W | amplitude of an electric field of a light wave polarized in x direction |
| $\varepsilon$ | W | error signal |
| $\eta$ | | Poisson's ratio |
| $\theta$ | rad | angle |
| $\kappa$ | $\frac{\mathrm{W}}{\mathrm{Km}}$ | thermal conductivity |
| $\lambda_0$ | m | wavelength of clock laser |
| $\nu$ | Hz | optical frequency |
| $\Delta\nu$ | Hz | difference in frequency |
| $\delta\nu$ | Hz | frequency variations |
| $\mathrm{mod}\,\sigma_{\mathrm{y}}$ | | modified Allan Deviation |
| $\sigma_{\mathrm{y}}$ | | Allan Deviation |
| $\tau$ | s | averaging time |
| $\Phi$ | | machnical loss factor |
| $\phi$ | rad | phase |
| $\Delta\phi$ | rad | phase difference |
| $\chi_{\mathrm{abs}}$ | m | absorbtion coefficient |
| $\mathcal{F}$ | | finesse |
| $w$ | m | $1/e^2$ beam waist |
| $\varnothing$ | m | diameter |

# List of figures

# List of tables

# List of publications

- Sebastian Häfner, Sofia Herbers, Stefan Vogt, Christian Lisdat, and Uwe Sterr. Transportable interrogation laser system with an instability of mod $\sigma_y = 3 \times 10^{-16}$. *Opt. Express*, 28(11):16407–16416, May 2020
- Sofia Herbers, Sören Dörscher, Erik Benkler, and Christian Lisdat. Phase noise of frequency doublers in optical clock lasers. *Opt. Express*, 27(16):23262–23273, Aug 2019
- Stefano Origlia, Mysore Srinivas Pramod, Stephan Schiller, Yeshpal Singh, Kai Bongs, Roman Schwarz, Ali Al-Masoudi, Sören Dörscher, Sofia Herbers, Sebastian Häfner, Uwe Sterr, and Christian Lisdat. Towards an optical clock for space: Compact, high-performance optical lattice clock based on bosonic atoms. *Phys. Rev. A*, 98:053443, 2018

# Acknowledgment

Ohne die Unterstützung Vieler wäre diese Arbeit nicht möglich gewesen. Ich freue mich die Gelegenheit zu haben mich an dieser Stelle bei ihnen bedanken zu können.

Als erstes möchte ich mich bei meinen Gutachtern und meinem Prüfungskomitee, PD Dr. Christian Lisdat, Prof. Dr. Piet O. Schmidt, Dr. Rodolphe Le Targat und Prof. Dr. Klemens Hammerer, bedanken.

Ein besonderer Dank geht an Christian Lisdat und Uwe Sterr für die Betreuung meiner Doktorarbeit und dafür, dass sie mir immer mit Rat und Tat zur Seite gestanden haben.

Ein großer Dank geht an meine Kollegen an der PTB, die mich während meiner Doktorarbeit begleitet und unterstützt haben. Vielen Dank für die Unterstützung im Labor, die Diskussionen und Erklärungen, die Fertigung der vielen Bauteile meines Experiments und all die ausgelösten Bestellungen. Ein besonderer Dank gilt Sören Dörscher und Sebastian Häfner für die Antworten auf meine unzähligen Fragen und die Unterstützung im Labor, und meinen langjährigen Bürokollegen, Roman Schwarz und Jacopo Grotti, für die tolle Gesellschaft.

Danke an die QUEST-LFS und besonders an Frau Ohlendorf für die freundliche und gewissenhafte Abwicklung meiner Prüfung.

Danke an meine Familie und meine Freunde für die Unterstützung und die Abwechselung zum Laboralltag. Ein besonderer Dank gilt Tine, die immer ein offenes Ohr hat und Ansgar, der mir ein produktives Arbeiten unter Corona im Homeoffice ermöglicht hat und meine Arbeit Korrektur gelesen hat.

# Curriculum vitae

## Research

since 07/2021 — **Scientist**

at Physikalisch-Technische Bundesanstalt (PTB)
Working group: 4.31 Unit of length

07/2015 - 06/2021 — **PhD Candidate**

at Physikalisch-Technische Bundesanstalt (PTB)
Working group: 4.32 Optical Lattice Clocks

## Academic Education

06/2015 — **Master of Science**

at Gottfried Wilhelm Leibniz Universität Hannover
Field of study: Nanotechnology

10/2012 — **Bachelor of Science**

at Universität Bielefeld
Field of study: Physics